

1995

Imaging and inverse problems of electromagnetic nondestructive evaluation

Steven Gerard Ross
Iowa State University

Follow this and additional works at: <https://lib.dr.iastate.edu/rtd>

 Part of the [Electrical and Electronics Commons](#)

Recommended Citation

Ross, Steven Gerard, "Imaging and inverse problems of electromagnetic nondestructive evaluation " (1995). *Retrospective Theses and Dissertations*. 10716.
<https://lib.dr.iastate.edu/rtd/10716>

This Dissertation is brought to you for free and open access by the Iowa State University Capstones, Theses and Dissertations at Iowa State University Digital Repository. It has been accepted for inclusion in Retrospective Theses and Dissertations by an authorized administrator of Iowa State University Digital Repository. For more information, please contact digirep@iastate.edu.

INFORMATION TO USERS

This manuscript has been reproduced from the microfilm master. UMI films the text directly from the original or copy submitted. Thus, some thesis and dissertation copies are in typewriter face, while others may be from any type of computer printer.

The quality of this reproduction is dependent upon the quality of the copy submitted. Broken or indistinct print, colored or poor quality illustrations and photographs, print bleedthrough, substandard margins, and improper alignment can adversely affect reproduction.

In the unlikely event that the author did not send UMI a complete manuscript and there are missing pages, these will be noted. Also, if unauthorized copyright material had to be removed, a note will indicate the deletion.

Oversize materials (e.g., maps, drawings, charts) are reproduced by sectioning the original, beginning at the upper left-hand corner and continuing from left to right in equal sections with small overlaps. Each original is also photographed in one exposure and is included in reduced form at the back of the book.

Photographs included in the original manuscript have been reproduced xerographically in this copy. Higher quality 6" x 9" black and white photographic prints are available for any photographs or illustrations appearing in this copy for an additional charge. Contact UMI directly to order.

UMI

A Bell & Howell Information Company
300 North Zeeb Road, Ann Arbor, MI 48106-1346 USA
313/761-4700 800/521-0600

Imaging and inverse problems of electromagnetic nondestructive evaluation

by

Steven Gerard Ross

**A Dissertation Submitted to the
Graduate Faculty in Partial Fulfillment of the
Requirements for the Degree of
DOCTOR OF PHILOSOPHY**

Department: Electrical and Computer Engineering

Major: Electrical Engineering (Electromagnetics)

Approved:

Signature was redacted for privacy.

Signature was redacted for privacy.

In Charge of Major Work

Signature was redacted for privacy.

For the Major Department

Signature was redacted for privacy.

For the Graduate College

Members of the Committee:

Signature was redacted for privacy.

**Iowa State University
Ames, Iowa
1995**

Copyright © Steven Gerard Ross, 1995. All rights reserved.

UMI Number: 9531782

**Copyright 1995 by
Ross, Steven Gerard
All rights reserved.**

**UMI Microform 9531782
Copyright 1995, by UMI Company. All rights reserved.**

**This microform edition is protected against unauthorized
copying under Title 17, United States Code.**

UMI

**300 North Zeeb Road
Ann Arbor, MI 48103**

TABLE OF CONTENTS

LIST OF TABLES.....	v
LIST OF FIGURES.....	vi
ACKNOWLEDGEMENTS.....	ix
CHAPTER 1. INTRODUCTION.....	1
1.1 Nondestructive evaluation.....	1
1.2 The Inverse Problem of NDE.....	2
1.2.1 Energy/material interactions.....	4
1.2.2 Data processing and material characterization.....	4
1.3 Solution methods for the inverse problem.....	5
1.3.1 Direct inversion methods.....	5
1.3.2 Indirection inversion methods.....	6
1.4 Motivation for research and scope of dissertation.....	7
CHAPTER 2. ELECTROMAGNETIC NDE.....	9
2.1 Introduction.....	9
2.2 Fully dynamic electromagnetics.....	9
2.2.1 The time-domain inverse problem.....	10
2.2.2 The time-harmonic inverse problem.....	16
2.3 MQS phenomena.....	22
2.3.1 The time-domain inverse problem.....	22
2.3.2 The steady-state inverse problem.....	27
2.3.3 Misconceptions about the MQS inverse problem.....	32
2.4 Static phenomena.....	39

2.5	Conclusions	39
CHAPTER 3	A COMPARISON OF EDDY CURRENT AND MILLIMETER WAVE NDE.....	42
3.1	Introduction.....	42
3.2	Experimental procedure and imaging techniques.....	43
3.2.1	Millimeter wave NDE.....	43
3.2.2	Eddy current NDE	50
3.3	Experimental results.....	51
3.4	Results from millimeter wave NDE through dielectric materials ...	55
3.5	Inspection of tight fatigue cracks.....	60
3.6	Conclusions and future work.....	63
CHAPTER 4	A DIFFUSION-TO-WAVE TRANSFORMATION FOR IMAGING MQS DATA	65
4.1	Introduction.....	65
4.2	The inverse problem.....	66
4.3	The inverse Q transform	70
4.4	Algorithm robustness.....	75
4.5	Transformation of non-impulsive sources	89
4.6	Conclusions	92
CHAPTER 5.	DIRECT INVERSION TECHNIQUES FOR MQS NDE PHENOMENA.....	93
5.1	Introduction.....	93
5.2	1-D analysis	95
5.3	2-D finite element study.....	102
5.3.1	Introduction.....	102
5.3.2	Results.....	106
5.3.3	Resolution.....	111

5.3.4 Modification for phase distortion effects	113
5.3.5 Noise effects.....	116
5.3.6 Coil effects.....	119
5.4 Experimental implementation.....	123
5.4 Conclusions	129
CHAPTER 6. CONCLUSIONS AND FUTURE WORK.....	131
6.1 Summary of contributions	131
6.2 Future work	133
6.3 Concluding remarks	134
REFERENCES.....	136

LIST OF TABLES

Table 4.1: Summary of transform parameters	76
Table 4.2: Summary of transform pairs	76
Table 5.1: Experimental results.....	129

LIST OF FIGURES

Figure 1.1	Block diagram of a generic NDE test and the associated inverse problem ...3	3
Figure 2.1	A typical microwave NDE test	12
Figure 2.2	Domain of dependence the 1-D hyperbolic system	14
Figure 2.3	Range of influence for the 1-D hyperbolic system.....	14
Figure 2.4	Typical characteristic lines of a 1-D hyperbolic boundary value problem..	15
Figure 2.5	A typical eddy current test	24
Figure 2.6	Characteristic lines of a 1-D parabolic boundary value problem.....	26
Figure 3.1	Experimental test set up	44
Figure 3.2	Antenna beam pattern [120]	44
Figure 3.3	SAR crossrange resolution [22].....	49
Figure 3.4	Data collection for pulsed measurement.....	49
Figure 3.5	Images of EDM notches (0.70 mm deep, 0.18 mm wide) (a) eddy current image (length 5 mm) (b) eddy current image (length 10 mm) (c) millimeter wave image (length 5 mm) (d) millimeter wave image (length 10 mm). Note the eddy current scale is half the millimeter wave scale	52
Figure 3.6	Sensitivity to EDM notch depth (length 10 mm, width 0.18 mm) (a) eddy current maximum impedance change vs. EDM notch depth (b) millimeter wave SAR maximum vs. EDM notch depth	54
Figure 3.7	Sensitivity to EDM notch width (length 5 mm, depth 0.70 mm) (a) eddy current maximum impedance change vs. EDM notch width (b) millimeter wave SAR maximum vs. EDM notch width.....	54
Figure 3.8	Millimeter wave SAR image of EDM notch with no covering (width 0.45 mm, depth 15 mm, length 5 mm) (a) C-scan (b) SAR.....	56
Figure 3.9	Millimeter wave images of EDM notch covered with 2 cm of nonconducting honeycomb composite (a) C-scan (b) SAR.....	57

Figure 3.10	Millimeter wave images of EDM notch covered with lossy plastic covering 2 mm thick (loss 10 dB/mm) and 7 mm of lossless plexiglass (a) C-scan (b) SAR.....	58
Figure 3.11	Millimeter wave images of EDM notch covered with 7.5 cm of inhomogeneous ceramic (a) C-scan (b) SAR.....	59
Figure 3.12	Diagram of fatigue crack	61
Figure 3.13	Eddy current image of fatigue crack including crack tip. Total scan dimensions (410 mm x 410 mm)	61
Figure 3.14	Images of millimeter wave scan of starter notch and fatigue crack (a) with reference wire between starter notch and fatigue crack (b) without reference wire	62
Figure 4.1	1-d test geometry for both wave and diffusion problems	67
Figure 4.2	Wave field of equation (4.11)	71
Figure 4.3	Diffusion field of equation (4.12).....	72
Figure 4.4	(a) Transformed wave field with regularization obtained by eliminating singular values below a given threshold (b) Transformed wave field with regularization obtained by eliminating singular values below a given threshold (c) Transformed wave field using Tikhonov regularization (d) Transformed wave field obtained by averaging 100 stable fields inverted using Tikhonov regularization.....	81
Figure 4.5	Wave field obtained with minimum sampling time in diffusion domain reduced to include higher rates of decay which result in unstable wave modes	84
Figure 4.6	(a) Diffusion field with SNR = 40 dB (b) Transformed wave field with regularization obtained by eliminated singular values below a given threshold (c) Transformed wave field obtained by averaging 100 stable fields regularized by eliminating singular values below a given threshold (d) Transformed wave field using Tikhonov regularization (e) Transformed wave field obtained by averaging 100 stable fields inverted with Tikhonov regularization.....	86
Figure 4.7	(a) Wave field obtained from inverting diffusion field with non-ideal impulse source (b) Low pass filtered version of (a).....	91
Figure 5.1	Geometry for the 1-D inverse problem.....	96
Figure 5.2	Phase shifts of intrinsic impedance ($f=2\text{MHz}$, Slab 2: $\sigma=1.4 \times 10^6$, $\mu=\mu_0, \epsilon=\epsilon_0$) (a) Slab 2: $\sigma = \infty, \mu=\mu_0, \epsilon=\epsilon_0$ (b) Slab 2: $\sigma = 0, \mu=\mu_0, \epsilon=\epsilon_0$ (c) Slab 2: $\sigma= 1.4 \times 10^6, \mu=\mu_0, \epsilon=\epsilon_0$	101

Figure 5.3	Eddy current finite element geometry.....	104
Figure 5.4	Image with current rail over stainless steel slab: void position (0.80,-0.30), predicted defect position (0.73,-0.99).....	107
Figure 5.5	Eddy current equiphase contours (a) current rail over a stainless steel halfspace (b) current rail embedded in a stainless steel fullspace.....	109
Figure 5.6	Image with current rail embedded in stainless steel: defect position (0.80,-0.30), predicted defect position (0.78,-0.34).....	110
Figure 5.7	Image with current rail consisting of 2 elements: defect position (0.80,-0.30), predicted defect position (0.80,-0.30).....	110
Figure 5.8	Image with defect closer to surface: defect position (0.80,-0.10), predicted defect position (0.78,-0.08).....	112
Figure 5.9	Impedance phase shift vs. void depth	112
Figure 5.10	Comparison of phase shift of ΔZ^s vs. defect depth (solid line) and the eddy current phase (time two) vs. sample depth (dotted line).....	115
Figure 5.11	Images with coil in air over stainless steel sample (a) defect position (0.80,-0.10), no phase multiplication (b) defect position (0.80,-0.30), no phase multiplication. (c) defect position (0.80,-0.10), phase multiplication p=12 (d) defect position (0.80,-0.30), phase multiplication p=12	117
Figure 5.12	Impedance data with SNR = 20 dB (a) real part (b) imaginary part	120
Figure 5.13	Images from modified algorithm with coil in air over stainless steel sample with SNR = 20 dB: defect position (0.80,-0.30) (a) phase multiplication p=12: predicted defect position (0.80,-0.30) (b) phase multiplication p=40: predicted defect position (0.80,-0.38).....	121
Figure 5.14	Phase shift of impedance vs. defect depth and eddy current phase vs. defect depth.....	122
Figure 5.15	Equiphase contours of experimental coil.....	125
Figure 5.16	Images of hole #2 (a) Magnitude of coil impedance (raster scan) (b) Image with p=1 (c) Image with p=12 (d) Image with p=12 and windowed impedance data	126

ACKNOWLEDGEMENTS

I would like to express my gratitude to my major advisor, Dr. William Lord, for introducing me to NDE and for giving me the opportunity to pursue my Ph.D. His guidance is the primary reason I chose to pursue a career in research and it will no doubt direct me throughout my life. I would like to thank my co-major advisor, Dr. Mark Lusk, for his insight which has been instrumental to this study. I enjoyed our numerous discussions, and I appreciate the time he spent to aid in this research.

I would also like to thank Dr. Yushi Sun for the many discussions which have provided me with a useful and unique perspective on this subject. I would like thank Dr. Hsiu Han, Dr. Paul Sacks, Dr. Lalita Udpa, and Dr. Satish Udpa for taking the time to serve on my committee and for providing much useful advice along the way.

I would also like to express my sincere gratitude to Dr. Min Namkung and NASA Langley Research Center for providing me with the funding to pursue this dissertation through the Graduate Student Researchers Program.

CHAPTER 1. INTRODUCTION

1.1 Nondestructive evaluation

Nondestructive evaluation (NDE) is used in industry to assess the character of structures and materials noninvasively. This differs from destructive testing methods in which a material must in some way be modified to determine its properties. NDE has applications in geophysics, medical diagnostics, and the detection of hidden explosives, however, one of its most useful applications is in determining the integrity of structures which have the potential for catastrophic failure. This includes the inspection of aircraft, railroads, ships, gas pipelines, and numerous other applications. In this setting, NDE is used periodically to determine the presence of any anomalies in a structure, e.g., a fatigue crack on an aircraft wing, which could potentially lead to a catastrophic failure. NDE has come to the forefront in industry for the following reasons [1]:

1. To ensure product reliability.
2. To prevent accidents and save human life.
3. To make a profit for the user.
 - a. To ensure customer satisfaction.
 - b. To aid in better product design.
 - c. To lower manufacturing costs.
 - e. To maintain a uniform quality level.

To accomplish these goals, NDE must not only detect flaws in structures, but also characterize the exact nature of the flaw in order to be able to assess the risk it poses to the overall integrity of the structure. This is important because often flaws can exist for many years without an induced failure. It would be extremely inefficient to determine a structure unsafe based on the presence of a flaw which in reality will be benign for a number of operation cycles. Of course, it would be disastrous if that flaw were to lead to a catastrophic failure. Therefore, the challenge of NDE is to obtain a quantitative characterization which is able to monitor the growth of flaws in a structure. This can then be used to accurately predict life cycles and thus decrease cost for the user while at the same time assuring safe operation.

1.2 The Inverse Problem of NDE

When a structure is inspected with NDE, data is gathered outside the structure with the intent of measuring specific material parameters or determining the location and character of defects. In every case data must be processed in order to obtain the information being sought. Since this amounts to working with an effect to determine its cause, such algorithms are referred to as inversion schemes. A block diagram of a generic NDE system is shown in Figure 1.1. A typical NDE test consists of energy/material interactions, the measurement and storage of these interactions, the subsequent signal processing of the field measurements, and the characterization of the material to determine its integrity. This entire process from energy measurements to final integrity characterization is known as the inverse problem of NDE.

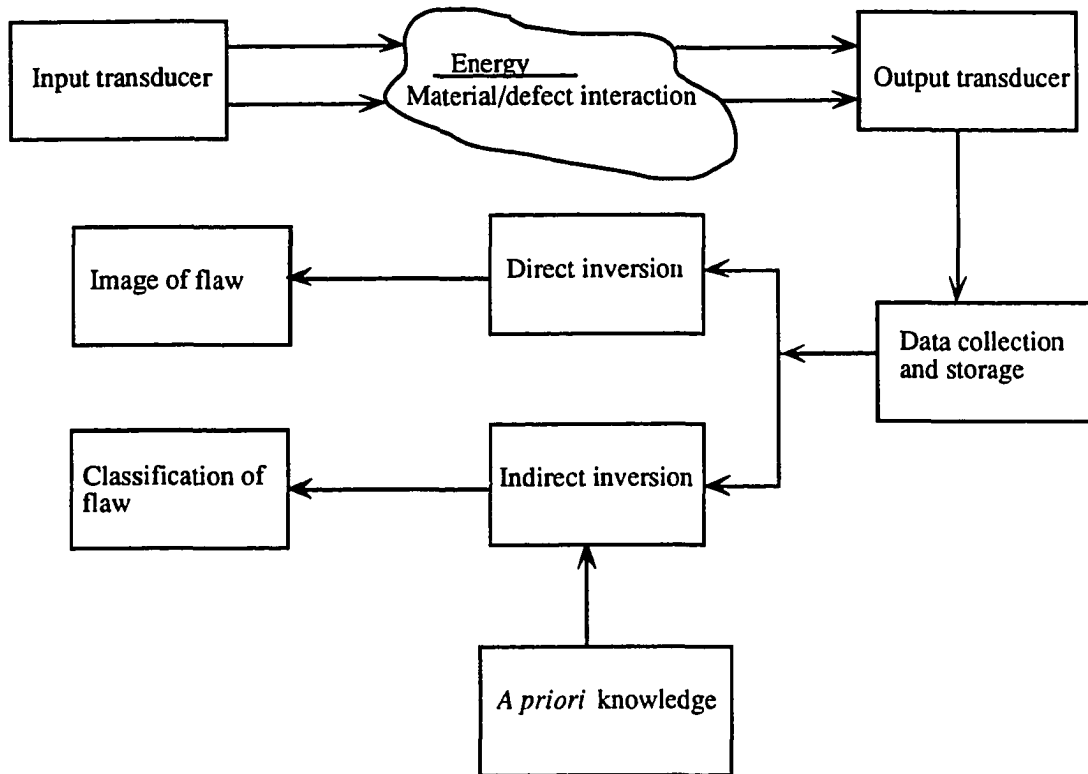


Figure 1.1. Block diagram of a generic NDE system and the associated inverse problem.

1.2.1 Energy/material interactions

All NDE methods require some form of energy that must interact with the structure under test. Generally, an input/output transducer acts as a source of these energy interactions. Note: often one transducer performs the functions of both the input and the output transducer. Various types of energy are used in NDE including ultrasonic [2-3], electromagnetic [1-2,4-5], and thermal [6-7]. The governing physical phenomena of a particular inspection depends directly on the type of NDE energy which is used. For example, ultrasonic energy interacts with the medium as propagating waves and thus the time-of-flight of traveling wave fields is often used to determine the position of flaws. Thermal energy, on the other hand diffuses through material and this process is very different than wave propagation. Time-of-flight is not defined for diffusion phenomena so it can not be used to determine the position of flaws, and instead other methods must be resorted to. Since the governing phenomena can have very different properties, the first step in the inverse problem of NDE is to understand the underlying physics of the energy/material interactions.

1.2.2 Data processing and material characterization

The energy/material interactions are measured with appropriate instrumentation and the data is stored digitally on a computer. This data is then processed to determine what characteristics of the material caused the particular energy/material interactions of the test. The information is then used to characterize the material and subsequently to determine the integrity of the material under test. This process, from data gathering to the determination of the integrity of the material is known as the inverse problem and is an extremely challenging aspect of NDE.

1.3 Solution methods for the inverse problem

1.3.1 Direct inversion methods

The goal of the inverse problem is to utilize the data of the NDE test to characterize anomalous regions in the test material. This can be most efficiently accomplished when a mathematical relationship exists which yields an explicit formula relating the measured fields to the characterization of the test structure. This relationship is known as a direct inversion formula and can be used to provide a visual reconstruction of the object which yields quantitative information about potential flaws in the test sample. The integrity of the material can then be determined in a reliable manner. Examples of direct inversion methods are computer aided tomography and holography. As shown in Chapter 2, the governing NDE phenomenon dictates whether a direct mathematical inversion method exists and whether or not it is sufficiently robust for practical exploitation. If the governing physics do not lead to a robust direct inversion scheme then indirect solutions have to be used instead.

Assuming that a mathematical inversion formula is available, it is still necessary for the appropriate field measurements to be available for use in the formula. For example, in X-ray inspections the frequency of operation is too high to measure any associated phase shift in the wave fields. If measurable, this phase information could potentially be used to obtain very high resolution images through direct inversion schemes. Because this information is not available, direct inversion algorithms have been developed to utilize measurements of amplitude instead of phase. It is also not possible to directly measure phase shifts associated with optical fields, however, the relative phase shift can be measured indirectly through holography schemes and direct inversion algorithms associated with optics exploit this phase information.

When available, direct inversion schemes provide an efficient technique for the quantitative characterization of anomalies in a test material. However, for a direct inversion scheme to be available two constraints must be met:

1. An analytic mathematical inversion formula must be obtained.
2. The field values necessary for the mathematical inversion must be physically measurable.

If either of these conditions are not met, indirect solution methods must be resorted to which provide a less efficient and typically less quantitative inversion than direct solution methods.

1.3.2 Indirect inversion methods

Indirect solutions differ from direct solutions in that the anomalous region in the test sample is not directly reconstructed. Instead, procedures are employed which utilize large amounts of *a priori* information along with iterative or classification techniques. Generally the measured data is compared with a previous known set of reference measurements which each correspond to a certain type and size of flaw, .e.g., a 1 mm long fatigue crack under a rivet. The character of the anomaly of interest is then determined from the reference standard which most closely matches the test signal. This process is generally performed with a computerized calibration scheme which relies on signal processing and large amounts of *a priori* knowledge [8-15].

In the past, reference standards were produced with experimental mock ups of the test structure, however, the last fifteen years have seen major advances in the use of computer simulations to generate reference data [16-17]. This can particularly be attributed to the large increases in computer speed and memory capabilities. The advantage found in indirect calibration procedures is that once an accurate classification scheme is perfected it can be

easily adapted to different test situations and geometries. The disadvantage associated with these indirect methods is that they do not directly reconstruct flaws associated with the material. Instead the information is more qualitative in nature in which a signal is classified as belonging to a particular flaw category.

1.4 Motivation for research and scope of dissertation

The motivation for this study arises from the NDE community's ongoing pursuit to develop direct inversion methods which can be used for the quick and reliable characterization of materials. In developing direct inversion algorithms it is critical that the underlying NDE phenomena be well understood and that the inversion algorithm be appropriately based on the governing physics. For example, "wave-based" inversion methods such as holography and tomography utilize properties of wave propagation such as scattering, back propagation, and time-of-flight. Often, however, inversion methods which utilize a particular phenomenon, e.g., wave propagation and scattering, are applied to a physical situation which does not support wave fields, e.g., diffusion. This is based on a misunderstanding of the underlying NDE phenomena and can lead to results which are not physically based and are therefore misleading.

The first goal of this research is to elucidate the role of the underlying physics and mathematics in the direct solution of electromagnetic NDE inverse problems. To do this, the differences in the governing mathematical and physical properties of diffusion and wave phenomena and their associated inverse problem are described. It is clearly shown how systems governed by wave propagation give rise to direct inversion schemes which utilize wave attributes such as scattering, back propagation, and time-of-flight. It is also shown how diffusion and its associated inverse problem differs from that associated with wave systems. This dissertation also presents two physically based and mathematically justifiable

techniques which can potentially be used for the direct inversion of diffusion systems. In Chapter 2 a theoretical background of electromagnetic phenomena and its associated inverse problems is given. Also, some misconceptions about diffusion are delineated. Chapter 3 describes research utilizing conventional imaging techniques for fully dynamic electromagnetic and magnetoquasistatic phenomena. Here a direct "wave-based" inversion scheme is used for millimeter wave NDE data and more qualitative images are obtained for eddy current NDE. The two methods are then compared to demonstrate differences between millimeter wave NDE governed by wave propagation and eddy current NDE governed by diffusion. In Chapter 4 a transformation is introduced which allows a diffusion field to be observed as a wave field and can be used to obtain direct imaging techniques for diffusion systems. An analytic inversion of the transformation is introduced to provide insight into robustness issues, while an averaging technique is introduced to regularize the numerical inversion of the transformation. Chapter 5 presents a direct inversion technique which can potentially be used to image subsurface flaws in conducting materials using eddy current NDE. A 1-D analytic study and a 2-D finite element simulation are utilized to clearly indicate the foundations of the technique and the physical limitations associated with the inversion method. Experimental results demonstrate the potential for applying this direct inversion scheme to realistic eddy current data. The conclusions of the study along with avenues for future research are described in Chapter 6.

CHAPTER 2. ELECTROMAGNETIC NDE

2.1 Introduction

Electromagnetic NDE is the science of noninvasively inspecting the structural character of materials using energy of the electromagnetic spectrum [1-2,4-5]. The goal of electromagnetic NDE is to characterize materials from measurements made around the sample. As with other NDE methods, this involves the solution of an associated inverse problem. Inversion procedures vary significantly with the type of electromagnetic phenomenon being exploited [5]. Mathematically, the approaches adopted depend upon the form that Maxwell's equations take which for a given material, geometry, and electromagnetic excitation can be either fully dynamic, magnetoquasistatic (MQS), electroquasistatic (EQS), or static.

2.2 Fully dynamic electromagnetics

As mentioned in Chapter 1, the inverse problem can be solved directly with mathematical inversion formulas developed from the underlying physics, or indirectly with classification schemes such as neural networks. The generalized solution of the fully dynamic electromagnetic inverse problem is quite difficult and requires some type of indirect solution method [18-19]. Although the generalized solution to the fully dynamic inverse problem can not be solved directly, there are simplifying approximations that allow direct inversion schemes to be employed. These direct inversion schemes can often be utilized on small computers and result in a fast and straightforward method of imaging anomalies in a test medium. As the

following sections point out, fully dynamic electromagnetic inversion methods are approached either in the time-domain with transient analysis or with time-harmonic analysis.

2.2.1 The time-domain inverse problem

In linear, homogeneous, isotropic, charge free, and source free media Maxwell's equations are given as [20]

$$\nabla \times \mathbf{E} = -\mu \frac{\partial \mathbf{H}}{\partial t} \quad (2.1)$$

$$\nabla \times \mathbf{H} = \frac{\epsilon \partial \mathbf{E}}{\partial t} + \sigma \mathbf{E} \quad (2.2)$$

$$\nabla \cdot \mathbf{E} = 0 \quad (2.3)$$

$$\nabla \cdot \mathbf{H} = 0 \quad (2.4)$$

where

\mathbf{E} = electric field intensity Volts/m

\mathbf{H} = magnetic field intensity Amps/m

ϵ = permittivity Farads/m

μ = permeability Henries/m

σ = conductivity Siemens/m.

Equations (2.1) - (2.4) imply that the electric field intensity, \mathbf{E} , and the magnetic field intensity \mathbf{H} , are governed by an equation of the form

$$\nabla^2 \mathbf{E} - \mu\sigma \frac{\partial}{\partial t} \mathbf{E} - \mu\epsilon \frac{\partial^2}{\partial t^2} \mathbf{E} = 0. \quad (2.5)$$

This hyperbolic partial differential equation describes electromagnetic wave phenomena in lossy media and is the governing equation for fully dynamic electromagnetic NDE systems. The significant characteristic of systems governed by (2.5) is that the energy propagates away from a source as a separate entity [21]. An example of a fully dynamic NDE test is shown in Figure 2.1 where a horn antenna generates electromagnetic waves which interact with a test sample and are then scattered back to the horn. Hyperbolic systems governed by (2.5) have certain features which can be exploited for the direct solution of the inverse problem. This is most easily demonstrated with a 1-D example. Consider the electric field equation (2.5) in a 1-D setting (uniform plane wave with no variations in the y or z directions) given by

$$\frac{\partial^2 \mathbf{E}}{\partial x^2} - \mu\epsilon \frac{\partial^2 \mathbf{E}}{\partial t^2} = 0 \quad (2.6)$$

with initial conditions

$$\mathbf{E}(x,0) = f(x) \quad (2.7)$$

$$\frac{\partial \mathbf{E}}{\partial t}(x,0) = g(x). \quad (2.8)$$

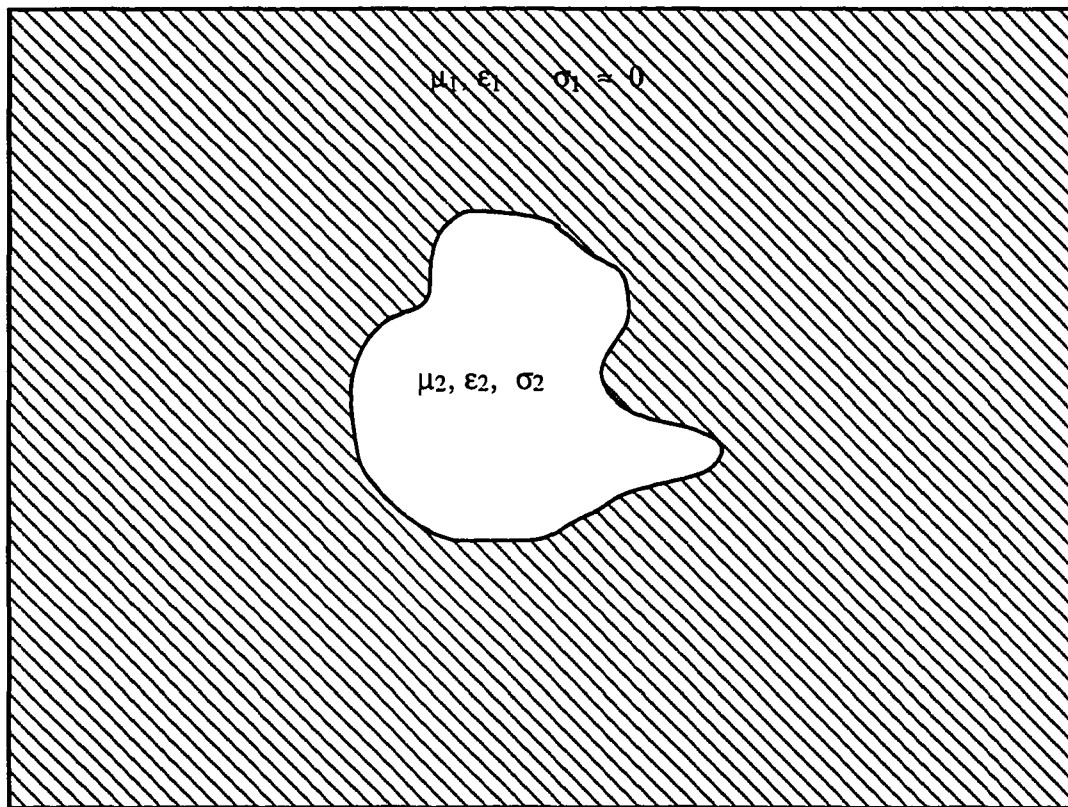
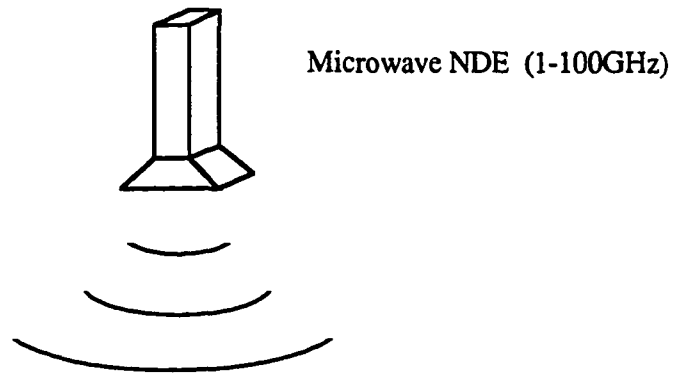


Figure 2.1 A typical microwave NDE test.

The solution to this initial value problem is given by [22-23]

$$E(x,t) = \frac{1}{2}[f(x+ct) + f(x-ct)] + \frac{1}{2c} \int_{x-ct}^{x+ct} g(\xi) d\xi \quad (2.9)$$

where

$$c = \frac{1}{\sqrt{\mu\epsilon}} \quad (2.10)$$

is the speed of electromagnetic wave propagation in the medium. From (2.9) it can be seen that the initial data only affect the solution $E(x',t')$ through their values for x in the interval $[x'-ct', x'+ct']$ of the x -axis in the region cut out by the lines $x+ct = x'+ct'$ and $x-ct = x'-ct'$ through the point (x',t') . These are known as the "characteristic lines" [22-23] and this interval represents the domain of dependence for the solution at the point (x',t') as shown in Figure 2.2. Also, the disturbance that originates at the point x' at time $t = 0$ only affect points in the wedge-shaped region of Figure 2.3 which is known as the "range of influence" of the point (x',t') . These properties indicate that for this system, disturbances travel with finite speed c . If boundary conditions are imposed at some point x' , the boundary will not feel the effect of the initial conditions until the disturbance travels along a characteristic line $x - ct = 0$ to the point x' , conversely the point $x = 0$ will feel no effect from the boundary until the initial disturbance reaches the boundary and travels along the characteristic line $x + ct = x' + ct'$ back to $x = 0$. This is demonstrated graphically in Figure 2.4 and is further discussed in Chapter 4. This finite speed of propagation is a unique characteristic of wave phenomena and is routinely exploited to help obtain a solution of the inverse problem. A simple example of this is seen in synthetic aperture radar (SAR) systems which utilize the time-of-flight of electromagnetic waves to and from a scattering object to determine the position of a flying object such as an

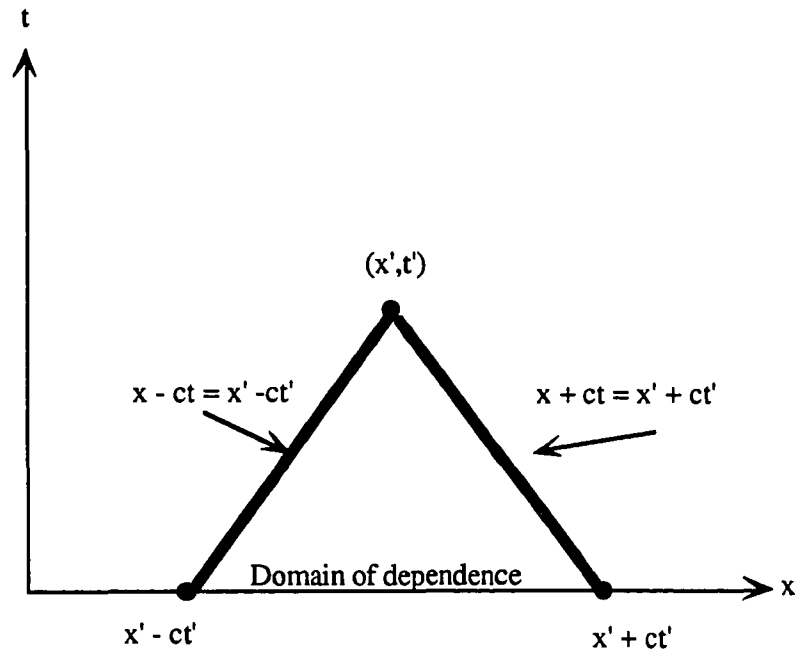


Figure 2.2 Domain of dependence the 1-D hyperbolic system

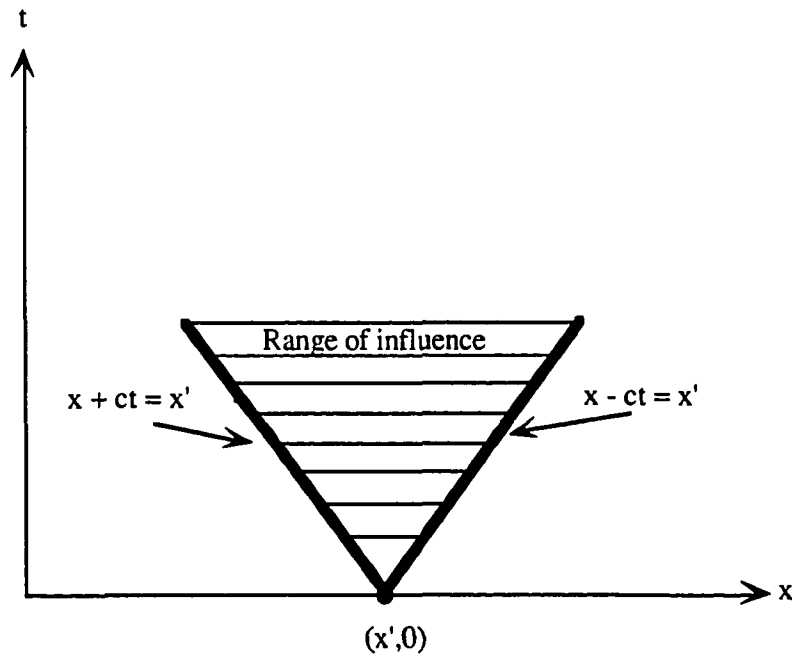


Figure 2.3. Range of influence for the 1-D hyperbolic system.

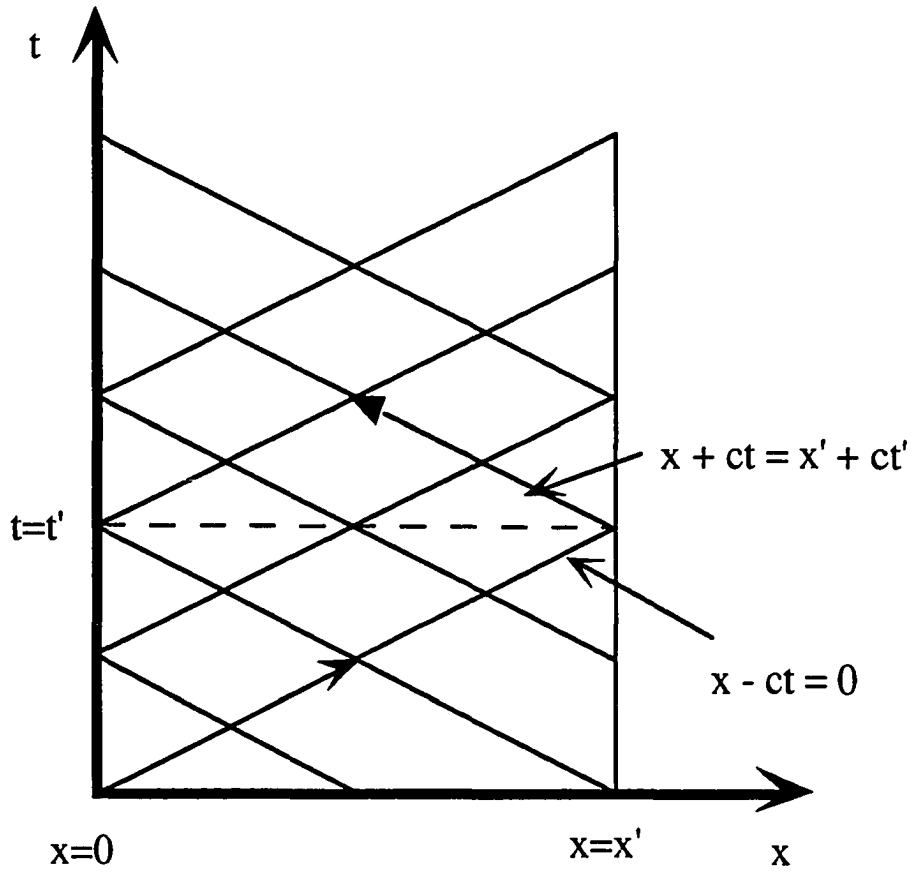


Figure 2.4. Typical characteristic lines of a 1-D hyperbolic boundary value problem.

aircraft [24-26]. There have been many developments in time-domain inverse problems for fully dynamic electromagnetics [27-34], however, the majority of NDE applications utilize single frequency time-harmonic sources. Since a time-domain measurement can be obtained from a time-harmonic swept frequency source, single frequency methods discussed in the next section can be extended to time domain applications.

2.2.2 The time-harmonic inverse problem

Often, the NDE test is performed with electromagnetic energy at a single sinusoidal frequency in which case the time harmonic fields are written as

$$\mathbf{E}(\mathbf{x},t) = \text{Re} [\mathbf{E}^s(\mathbf{x}) \exp(j\omega t)] \quad (2.11)$$

where ω is the frequency of operation, $j = \sqrt{-1}$, and \mathbf{E}^s is the phasor representation of the time-harmonic electric field. Maxwell's equations (2.1)-(2.4) can now be written as

$$\nabla \times \mathbf{E}^s = -j\omega\mu \mathbf{H}^s \quad (2.12)$$

$$\nabla \times \mathbf{H}^s = \sigma\mathbf{E}^s + j\omega\epsilon\mathbf{E}^s \quad (2.13)$$

$$\nabla \cdot \mathbf{E}^s = 0 \quad (2.14)$$

$$\nabla \cdot \mathbf{H}^s = 0. \quad (2.15)$$

The governing electric field equation for this time-harmonic system is given as

$$\nabla^2 \mathbf{E}^s + k^2 \mathbf{E}^s = 0 \quad (2.16)$$

where

$$k^2 = \omega^2 \mu \epsilon - j \omega \mu \sigma, \quad (2.17)$$

and (2.16) is the elliptic equation that describes single frequency time-harmonic wave phenomena. When the NDE test is time-harmonic, transient effects are neglected and the time-of-flight of disturbance can no longer be utilized because the governing equation has no time dependence. A transient disturbance can be generated through swept frequency measurements, however, in that case (2.5) is the governing equation. Consider the 1-D system

$$\frac{\partial^2 E^s}{\partial x^2} - \omega^2 \mu \epsilon E^s = 0 \quad (2.18)$$

whose solution is

$$E^s(x) = E_0^s \exp(-j \omega \sqrt{\mu \epsilon} x) \quad (2.19)$$

with the time-harmonic solution given by

$$E(x) = E_0 \cos(\omega \sqrt{\mu \epsilon} x + \omega t) \quad (2.20)$$

which describes spatially harmonic and time-harmonic waves. It is assumed that all transient effects have vanished and the only time variations are sinusoidal oscillations. Consequently, the time-of-flight of a signal to and from a scatterer can not be utilized in the solution of the inverse problem. However, the hyperbolic nature of the underlying mathematics can be

exploited by utilizing the relative phase shifts between the scattered and incident wave fields to determine the distance from the source to the scattering object analogously to the previous time-of-flight measurements. The simplest example of this is when an electromagnetic wave is assumed to be a uniform plane wave incident upon a perfectly conducting scattering object. The phase shift of the scattered field can then be measured and compared to the phase shift of the incident field. From this measurement the distance between the source and the scattering object can be determined within a multiple of a wavelength of the source. As mentioned previously, this concept is utilized in SAR to determine the position of aircraft [24-26,35].

Formally, for higher dimensional time-harmonic systems, the governing equation for the fully dynamic electric field in the presence of a scattering medium is given by [36-37]

$$\mathbf{E}^s(\mathbf{x}) = \mathbf{E}_0^s(\mathbf{x}) + \int_v (k^2(\mathbf{x}') - k_0^2) \mathbf{G}(\mathbf{x}; \mathbf{x}') \cdot \mathbf{E}^s(\mathbf{x}') dv \quad (2.21)$$

where $\mathbf{E}^s(\mathbf{x})$ is the total field that results from the interaction of the incident field $\mathbf{E}_0^s(\mathbf{x})$ with the scattering medium. Here k describes the scattering medium, k_0 describes the host medium, \mathbf{G} is the Green's function of the geometry, and v is the volume of the scatterer. The goal of the fully dynamic inverse problem is to determine the properties of the scattering medium $k(\mathbf{x})$ through measurements of the electric field outside the medium. This requires the inversion of (2.21) for $k(\mathbf{x}')$ which is quite difficult because the relation between the unknown contrast $(k^2(\mathbf{x}') - k_0^2)$ and the measured scattered field is nonlinear in general. The nonlinear inversion of (2.21) is an active topic of research [38-44]. There are, however, a number of approximations [45-50] which can be used to linearize the inversion of (2.21). These approximations are either in the form of the electromagnetic wave or in the form of the scattering properties of the anomalous region. There are a variety of direct inversion techniques which utilize these approximations for the linearized inversion of (2.21) [51-59].

These techniques provide a fast and computationally inexpensive method for obtaining a quantitative description of a scattering object. For example, to determine the position of small conducting object in the far field of the antenna, the generalized inversion of (2.21) is not necessary. Instead assumptions about the material parameters of the object can be utilized which result in reliable approximate solutions. For instance, the scattering medium can be considered to be a perfect conducting point (impulse function), the source field a uniform far field plane wave, and $G(\mathbf{x};\mathbf{x}')$ the far field Green's function given by

$$G(\mathbf{x};\mathbf{x}') = \frac{\exp[-j\beta(\mathbf{x};\mathbf{x}')] }{4\pi(\mathbf{x};\mathbf{x}')}. \quad (2.22)$$

Multiple scattering can be neglected so the total field $\mathbf{E}^s(\mathbf{x})$ inside the integrand is equal to the source field $\mathbf{E}_0^s(\mathbf{x})$. Equation (2.21) can now be written as

$$\mathbf{E}_{\text{scatter}}^s(\mathbf{x}) = \mathbf{E}_0^s \frac{\exp(-j2\beta|\mathbf{x}-\mathbf{x}'|)}{4\pi|\mathbf{x}-\mathbf{x}'|} \quad (2.23)$$

with

$$\mathbf{E}_{\text{scatter}}^s(\mathbf{x}) = \mathbf{E}^s(\mathbf{x}) - \mathbf{E}_0^s(\mathbf{x}) \quad (2.24)$$

representing the scattered field. A synthetic aperture can then be formed to utilize measurements of the scattered field from different positions to determine the position of the perfectly conducting point scatterer. This technique utilizes many approximations, however, it can be used to predict the position of conducting objects for fully dynamic NDE [60].

In general, of course, the far field Green's function can not be employed and the anomalous region can not be treated as a perfectly conducting point. However, there are still

approximations which can be used to simplify the inversion of (2.21). One very common method is the Born approximation [46-48] in which the total field $\mathbf{E}^s(\mathbf{x})$ is approximated by the incident field $\mathbf{E}_0^s(\mathbf{x})$ by assuming that the scattering medium is weak. Utilizing the Born approximation, (2.21) can be written as

$$\mathbf{E}_{\text{scat}}^s(\mathbf{x}) = \int_v \left(k^2(\mathbf{x}') - k_0^2 \right) \mathbf{G}(\mathbf{x}; \mathbf{x}') \cdot \mathbf{E}_0^s(\mathbf{x}') \, dv. \quad (2.25)$$

which is now an explicit formula for the anomalous region $k(\mathbf{x})$ from measurements of the scattered field. There are many such approximations which can be utilized to obtain an explicit relationship between measurements of the scattered field and the anomalous region [45-50]. These then yield direct inversion schemes which have many industrial applications [51-59].

There are a number of electromagnetic NDE methods which utilize some sort of direct inversion method for the characterization of materials including microwave [57-62], optical [63-68], and X-ray [55,69-70] NDE techniques. All of these techniques utilize the fact that electromagnetic fields propagate through space and are scattered and attenuated by anomalous regions in the space. Although electromagnetic propagation occurs for all of the above techniques, the fields behave somewhat differently at different operating frequencies. Because of this, the instrumentation used to measure the electromagnetic fields must be varied with operating frequency. As mentioned in Chapter 1, the mathematical inversion algorithm must correspond to the physical field measurements which are available at the operating frequency of interest. This has led to the development of different inversion techniques which are utilized for different test frequencies and material parameters.

A typical microwave NDE test is used to inspect low loss material for defects in the frequency range of 1-100 GHz [61-62]. The scattered fields can be used to determine specimen properties and to locate defects in a specimen. At these frequencies the wavelength is

between 30 cm and 3 mm, and for most NDE inspections wave effects such as diffraction must be taken into account. The measurement instrumentation is able to separate the scattered field from the incident field and directly measure their associated phase shifts. For swept frequency measurements Fourier synthesis can be used to generate a time domain pulse from this phase information. Under certain approximations, this information can then be used to characterize materials quantitatively. Optical techniques utilize lasers to inspect materials in the frequency range of 10^{14} - 10^{15} Hz, where the wavelength is approximately 10^{-7} m. The phase shift of the electromagnetic waves is not directly measurable at these frequencies, so instead indirect approaches such as holography are utilized to measure the relative phase shift of the electromagnetic waves [63-68]. This information can then be used subsequently to reconstruct anomalies which the wave field encounters. X-ray methods use electromagnetic frequencies in the range of 10^{17} - 10^{18} Hz with associated wavelengths of approximately 10^{-10} m. At these frequencies, no attempt is made to measure the phase shift of the propagating wave field, rather measurements of the attenuation of the field are used to reconstruct anomalous regions inside the test sample. This measurement limitation is overcome by using inversion techniques requiring only amplitude measurements [55,69-70]. The differences in the measurement technique for these three fully dynamic NDE techniques demonstrate the statement of Chapter 1 that solutions for the inverse problem must utilize the physical measurements which are available. In all cases, the anomalous region is reconstructed through inversion procedures which utilize the underlying properties of electromagnetic wave phenomena.

This section has demonstrated that properties of fully dynamic electromagnetic wave phenomena such as scattering and finite time of travel can be exploited to obtain a direct solution of the inverse problem. In general, the nonlinear inversion of the integral equation (2.21) must be performed to characterize the scattering medium. In some instances, linearizing approximations can be used to obtain direct explicit inversion formulas that can be used to characterize scattering objects. Although these techniques are not described in detail here, the

underlying mathematics of all of these methods utilize basic concepts of wave phenomena such as scattering, time-of-flight, and back propagation of wave fields. These direct inversions are not applicable in many instances because the complexity of the system often renders the linearizing approximations invalid. In these instances indirect approaches must be utilized to invert the field data. However, the physically based, mathematical inversion is possible under certain approximations and these techniques are frequently used in industry. This point is emphasized because the next section demonstrates the misuse of these direct "wave-based" imaging techniques on phenomena which are not governed by wave propagation.

2.3 MQS phenomena

2.3.1 The time domain inverse problem

If the frequency of the transducer is sufficiently low and/or the medium is sufficiently conductive, conduction current dominates and displacement current can be neglected in (2.2). In this case Maxwell's equations for a source free region are now written as

$$\nabla \times \mathbf{E} = -\mu \frac{\partial \mathbf{H}}{\partial t} \quad (2.26)$$

$$\nabla \times \mathbf{H} = \sigma \mathbf{E} \quad (2.27)$$

$$\nabla \cdot \mathbf{E} = 0 \quad (2.28)$$

$$\nabla \cdot \mathbf{H} = 0. \quad (2.29)$$

The fields are now considered magnetoquasistatic (MQS) [71] and the governing electric field equation is given as

$$\nabla^2 \mathbf{E} - \mu\sigma \frac{\partial}{\partial t} \mathbf{E} = 0. \quad (2.30)$$

Equation (2.30) is the parabolic equation governing time-domain MQS phenomena, e.g., pulsed eddy current NDE [72-74]. For pulsed eddy current tests, a coil sets up a time-varying magnetic field which induces time varying eddy currents in the test sample as shown in Figure 2.5. These currents in turn set up fields which affect the source coil. When the eddy currents are disrupted by anomalies, the time-domain voltage of the source coil is affected accordingly and indicates the presence of an anomaly. As this section demonstrates, the features of the parabolic equation (2.30) do not lend themselves well to solutions of the inverse problem. By neglecting displacement current in (2.2), MQS approximations exclude the possibility of wave propagation and instead, field interactions with materials result in diffusion phenomena. Since the solutions to (2.30) do not allow wave propagation, phenomena such as scattering and time-of-flight are not available for the quantitative solution of the inverse problem as they are for phenomena governed by the fully dynamic system of (2.5) [75]. Consequently, the character of the anomalous region is generally determined by calibration procedures.

Consider the 1-D parabolic equation given by

$$\frac{\partial^2 \mathbf{E}}{\partial x^2} - \mu\sigma \frac{\partial \mathbf{E}}{\partial t} = 0 \quad (2.31)$$

with initial condition

$$\mathbf{E}(x,0) = f(x). \quad (2.32)$$

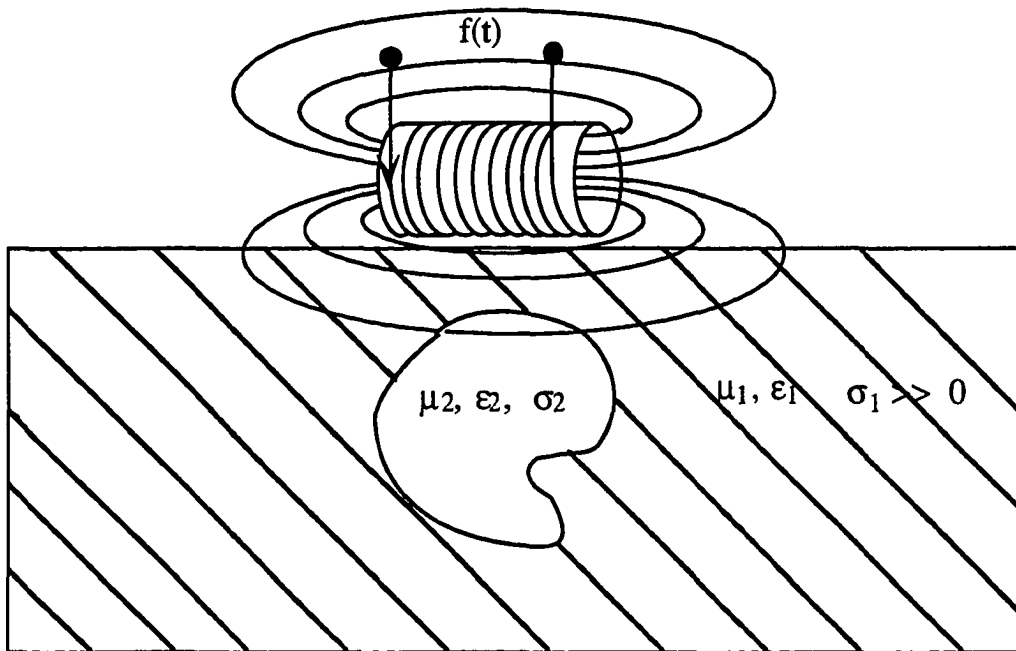
Eddy Current NDE ($f < 5 \text{ MHz}$)

Figure 2.5. A typical eddy current test.

The solution to this system is given by [22]

$$E(x,t) = \int_{-\infty}^{\infty} k\left(x-y, \frac{t}{\mu\sigma}\right) f(y) dy \quad (2.33)$$

where

$$k(x,t) = \frac{1}{\sqrt{4\pi t}} \exp\left(-\frac{x^2}{4t}\right). \quad (2.34)$$

Clearly, for $t > 0$, $E(x,t)$ depends on the values of f at all points. Also, the values of f near one point will affect the value of $E(x,t)$ at all x an infinitesimal moment later, though only imperceptibly at large distances. Thus, signals here travel with infinite speed, indicating some limitation to the strict applicability of the heat equation to physical phenomena. The main point is that disturbances do not travel with a finite speed of propagation as they do for hyperbolic systems. Instead a disturbance disperses itself through the medium instantaneously along the characteristic lines $t = \text{constant}$ so the domain of dependence and the region of influence for a parabolic equation is infinite, unlike the finite domain of hyperbolic equations. If boundary conditions are imposed at some point $x = x'$, the boundary feels the effect of the initial disturbance instantaneously, conversely the point $x = 0$ also feels the effect of the boundary instantaneously. This is demonstrated graphically in Figure 2.6.

Thus, there are significant differences between fully dynamic electromagnetics and MQS systems. For fully dynamic systems scattering, time-of-flight, and propagation of disturbances along the characteristic lines can be used to solve the inverse problem directly. For MQS systems disturbances are felt instantaneously throughout the medium of interest. Wave attributes such as time-of-flight, scattering, and propagation of disturbances are not available

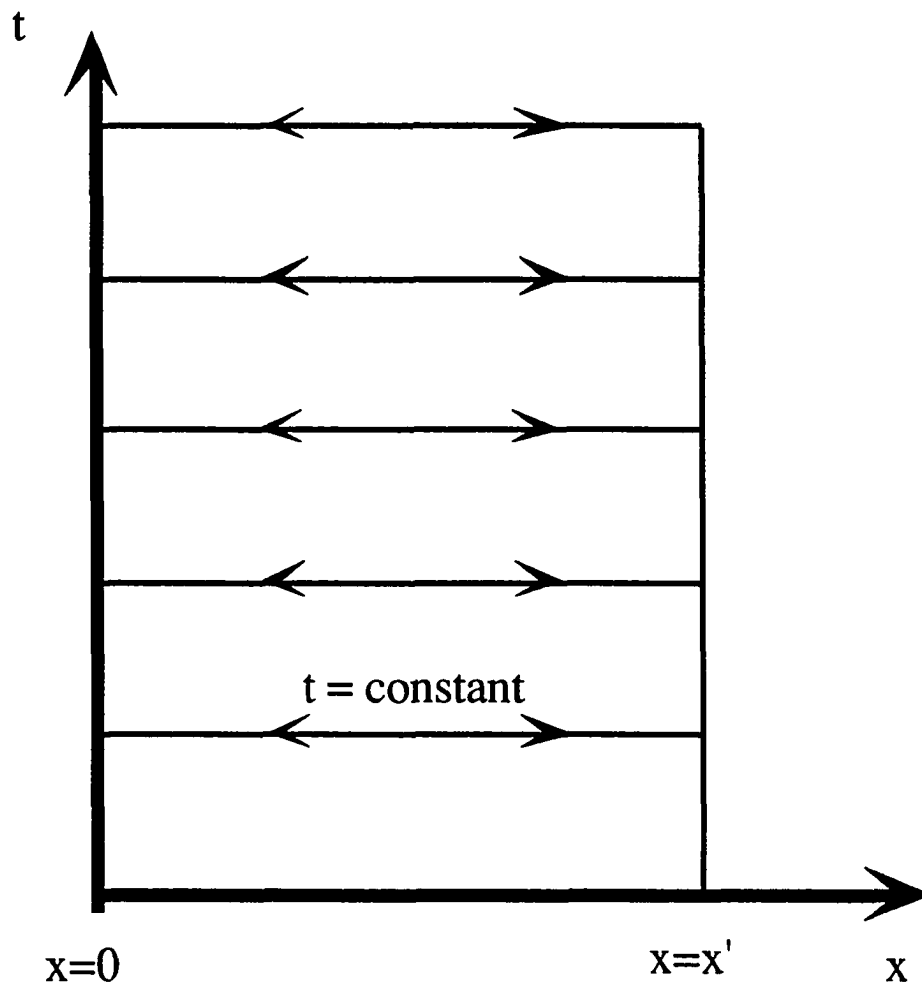


Figure 2.6. Characteristic lines of a 1-D parabolic boundary value problem.

for the solution of the inverse problem. Because of this, direct inverse schemes which exploit time-of-flight, scattering and back propagation can not be utilized for parabolic systems. Instead, data obtained from MQS interactions governed by the parabolic system of (2.30) are generally processed by forward based (calibration) algorithms which interpret data through comparisons with previous results, often facilitated by artificial intelligence techniques [8-12].

There is, however, a mathematical transformation which exists between the hyperbolic equation (2.5) and the parabolic equation (2.30) [76-78]. As discussed in Chapter 4, the transformation can be used to observe diffusion data in a wave format and to solve the inverse problem subsequently with wave attributes such as time-of-flight, scattering, and back propagation [79-82]. There are, however, many difficulties associated with the transformation which limit its applicability. The fact that the transformation exists does not imply that systems governed by hyperbolic equations are in some sense equivalent to systems governed by parabolic equations, rather, its ill-posedness helps to demonstrate their differences.

2.3.2 The steady-state inverse problem

Generally, the differences between hyperbolic partial differential equations and parabolic partial differential equations are recognized and their associated inverse problem are treated accordingly [83-86]. At issue is the time harmonic form of the parabolic system (2.30) which can be derived from Maxwell's equations. For time-harmonic measurements under the MQS approximation, Maxwell's equations are given as

$$\nabla \times \mathbf{E}^s = -j\omega\mu \mathbf{H}^s \quad (2.35)$$

$$\nabla \times \mathbf{H}^s = \sigma\mathbf{E}^s \quad (2.36)$$

$$\nabla \cdot \mathbf{E}^s = 0 \quad (2.37)$$

$$\nabla \cdot \mathbf{H}^s = 0. \quad (2.38)$$

The governing electric field equation for this steady state system is now given as

$$\nabla^2 \mathbf{E}^s + k^2 \mathbf{E}^s = 0 \quad (2.39)$$

where

$$k^2 = -j\omega\mu\sigma. \quad (2.40)$$

MQS phenomena generally occur at low operating frequencies ($f < 5$ MHz) and with high material conductivities ($\sigma > 10^5$ S/m). At these frequencies displacement current is negligible compared to conduction current and although the governing time-harmonic MQS field equations are of similar to form to those of time harmonic fully dynamic wave field, the underlying physics exclude wave propagation.

Consider the 1-D system given by

$$\frac{\partial^2 \mathbf{E}^s}{\partial x^2} - j\omega\mu\sigma \mathbf{E}^s = 0 \quad (2.41)$$

whose solution in phasor form is given by

$$\mathbf{E}(x) = E_0 \exp\left[-\sqrt{\frac{\omega\mu\sigma}{2}} (1 + j) x\right] \quad (2.42)$$

with the steady-state solution written as

$$E(x,t) = E_0 \exp\left(-\sqrt{\frac{\omega\mu\sigma}{2}} x\right) \cos\left(\sqrt{\frac{\omega\mu\sigma}{2}} x - \omega t\right). \quad (2.43)$$

Equation (2.43) describes a field decaying exponentially in magnitude and having a linear phase shift with depth. Although (2.43) has the mathematical form of a wave field, it does not actually describe a true electromagnetic wave. This is clear from the fact that displacement current is negligible under the MQS approximation. Thus, (2.43) simply describes an MQS field which has no transient behavior but instead oscillates in time and space and decays with distance x . Conversely, an interface at some point x' mathematically has the form of a scattered wave field, but the underlying parabolic nature of the governing MQS phenomena results in effects which are felt instantaneously throughout, so there are no incident and scattered fields of which to measure the relative phase shifts as there are in fully dynamic systems.

The most common MQS NDE method is steady state eddy current NDE. A single frequency coil is used to generate a magnetic field which induces eddy currents in the test specimen as shown in Figure 2.5. As with pulsed eddy current tests, these induced eddy currents are disrupted by any anomalies in the sample and this in turn alters the voltage of the source coil. Since, wave propagation does not occur in MQS phenomena, the source fields do not propagate away from the coil, scatter off the anomaly, and propagate back to the source coil as they do for fully dynamic electromagnetic systems. Instead, as the previous section demonstrates, effects are felt instantaneously and depend on both the source coil and the anomalous region. Generally, this effect on the source coil is measured indirectly in terms of the complex impedance of the source coil. This is very different from wave systems, where there is direct access to fields which are scattered from anomalous regions. The impedance measurements are not generally used directly to reconstruct anomalous regions in the test material, but rather are used to indicate the presence of a flaw qualitatively [87-88] as is

demonstrated in Chapter 3. Calibration procedures are then used to determine the exact character of the flaw.

Formally, the time-harmonic MQS electric field E^s in the presence of an anomalous region is given by [89]

$$E^s(\mathbf{x}) = E_0^s(\mathbf{x}) + \int_V (k^2(\mathbf{x}') - k_0^2) G(\mathbf{x}; \mathbf{x}') \cdot E^s(\mathbf{x}') dV \quad (2.44)$$

where $E_0^s(\mathbf{x})$ is the source field in the absence of the anomaly, and $E^s(\mathbf{x})$ is the total field in the presence of the inhomogeneity. Equation (2.43) is of course, mathematically equivalent to the solution (2.21) of the fully dynamic electric field in the presence of a scattering object. As in the wave case, the inversion of (2.44) can lead to a reconstruction of the anomalous region in the medium. However, scattering and back propagation can not be employed to solve the inverse problem because the phenomenon is parabolic in nature. Examples of the mathematical inversion of (2.44) are given by Sabbagh [90] where the Green's function for a certain geometry is derived and is then used to invert (2.44) to characterize the properties of the anomalous region $k(x)$. This suffers from the disadvantage that the derivation of Green's function is quite difficult for most geometries. The inversion of (2.44) is also shown to be invertible under certain approximations for a layered halfspace problem [91].

For MQS systems, and in particular eddy current NDE, it is much more difficult to obtain the relevant physical measurements than for fully dynamic systems. This is because the fields which arise due to the presence of an inhomogeneity are not as physically accessible under the MQS approximation as are they are for fully dynamic systems. For wave systems, for example, the radiating field is scattered and this scattered field can be measured and compared to the source field. For MQS systems, e.g., eddy current NDE, the fields do not propagate away from the source and scatter off of anomalies. Instead the eddy currents which are

induced in the conducting test sample by the source coil are disrupted by anomalies in the test sample. This in turn instantaneously affects the fields of the source coil through MQS induction and this effect is measured as a change in the impedance of the source coil. The impedance of the source coil is not a direct measurement of the field which results from the eddy current perturbation. Instead, the impedance measurement is an integrated effect which includes factors which depend on the source coil, test geometry, and the eddy currents induced throughout the sample [4].

Auld, et. al [92] use reciprocity to derive a formula for the impedance change in a coil over a halfspace in terms of the source current I , the conductivity variation in the medium, and the electric field $\mathbf{E}^s(\mathbf{x})$. The complex impedance change ΔZ^s of a coil over a conducting halfspace with host conductivity σ_0 and containing an anomalous region with conductivity $\sigma(\mathbf{x})$ is given as

$$\Delta Z^s = \frac{1}{I^2} \int_{V_D} (\sigma(\mathbf{x}) - \sigma_0) \mathbf{E}_0^s(\mathbf{x}) \cdot \mathbf{E}^s(\mathbf{x}) dv, \quad (2.45)$$

where $\mathbf{E}^s(\mathbf{x})$ is the electric field in the presence of an anomaly, $\mathbf{E}_0^s(\mathbf{x})$ is the electric field in the absence of the anomaly, and I^s is the source current in the eddy current coil. Measurements of ΔZ^s can be used to determine features of a defect such as a surface crack in a metal [93]. However, in general the impedance change ΔZ^s varies nonlinearly with variations in conductivity, thus, the inversion of (2.45) is quite difficult and generally limited to simplified geometries. There has been success using linearizing approximation to invert directly (2.45) to obtain a conductivity profile [94]. Chapter 5 demonstrates a linearized inversion of (2.45) which can be implemented to image small subsurface flaws.

2.3.3 Misconceptions about the MQS inverse problem

An important concept of electromagnetic phenomena is that when displacement current is negligible compared to conduction current, wave propagation does not occur and the fields are MQS. Also, if the operating frequency is sufficiently low that the time rate of change of the electromagnetic fields is very small, the fields are also considered EQS and wave propagation and radiation do not occur. The misunderstanding of this concept has led to much confusion in both the general public and the research community. For example, there is much recent concern about radiation affects from power lines. However, the idea of radiation from power lines is a misnomer because at the frequencies of power transmission (60 Hz) displacement current is sufficiently small that quasistatic approximations are valid and radiation does not occur [95]. Also, many electromagnetic texts often ignore MQS approximations for electromagnetic fields in conducting materials [20,96]. If an electromagnetic wave traveling in space encounters a material sufficiently conductive so that conduction current dominates displacement current, wave propagation does not occur in the metal and instead the fields are governed by MQS diffusion. This concept is often ignored in electromagnetic texts [20,96] and demonstrates that many authors do not lend a clear understanding of MQS phenomena. This same misunderstanding has led to a considerable amount of confusion about the MQS inverse problem.

The previous section demonstrates that there are approaches which result in a direct solution to the MQS inverse problem. These approaches must be mathematically rigorous and subsequently treat the underlying MQS phenomenon appropriately. There have, however, been attempts to obtain direct solutions to the MQS inverse problem without a rigorous physical basis. In these instances, the similarity of the fully dynamic equation (2.16) and (2.21) to the MQS equation (2.39) and (2.44), respectively, has led many researchers to refer to steady-state MQS diffusion and thermal diffusion phenomena as arising from “skin waves”

[97-100]. This in turn has led them to consider the possibility of developing direct inversion schemes such as those used for fully dynamic electromagnetic phenomena, e.g., holography and diffraction tomography, for the processing of data associated with MQS diffusion. These approaches are generally employed for single frequency eddy current inspections governed by (2.39) where the magnitude and phase of the complex impedance of a coil is recorded to detect the presence of a flaw. Under the premise that the phase shifts of time-harmonic eddy current impedance measurements are in some sense analogous to those obtained by wave-based devices, a number of researchers have applied direct "wave-based" reconstructions directly to such diffusive data [97-102]. Generally, these techniques assume that since the eddy currents in the sample are oscillatory and have an associated phase repetition period, the eddy currents arise from wave phenomena, which is contrary to the underlying MQS approximations.

One direct "wave-based" imaging technique which has been attempted on eddy current phenomena is diffraction tomography (DT) [100]. Here, the fact that the integral formulation of electric currents and fields is formally the same as the one describing a wave scattering phenomenon results in the development of eddy current diffraction tomography inversion algorithms. Formally, diffraction tomography represents a linearized solution of the nonlinear inverse problem (2.21) such that the field data is backpropagated in order to generate some quantity that depends upon the unknown scatterer properties. For wave fields, imaging can be done with the application of FFT-based diffraction tomography procedures, and in fact this has been utilized for microwave NDE [57]. The application of DT to eddy current phenomena is suspect based on the fact that under the MQS approximation, wave propagation does not occur and therefore neither can backpropagation. For clarity, the steps of DT used in [100] are briefly reviewed. First a Born like approximation is used in which the total electric field in the presence of an anomalous region $E^s(\mathbf{x})$ is approximated by the original source field in the absence of an anomalous region $E_0^s(\mathbf{x})$. Equation (2.44) can now be written as

$$\mathbf{E}^s(\mathbf{x}) = \mathbf{E}_0^s(\mathbf{x}) + \int_V (k^2(\mathbf{x}') - k_0^2) \mathbf{G}(\mathbf{x}; \mathbf{x}') \cdot \mathbf{E}_0^s(\mathbf{x}') dV \quad (2.46)$$

which then yields the relationship for the anomalous field

$$\mathbf{E}_a^s(\mathbf{x}) = \int_V (k^2(\mathbf{x}') - k_0^2) \mathbf{G}(\mathbf{x}; \mathbf{x}') \cdot \mathbf{E}_0^s(\mathbf{x}') dV \quad (2.47)$$

where

$$\mathbf{E}_a^s(\mathbf{x}) = \mathbf{E}^s(\mathbf{x}) - \mathbf{E}_0^s(\mathbf{x}). \quad (2.48)$$

By expanding $\mathbf{G}(\mathbf{x}, \mathbf{x}')$ into a spectral expansion, a linear relationship is obtained between the Fourier transform of the measured anomalous field and the anomalous region. Then, after taking measurements along a line above the flaw region, and subsequently Fourier transforming that data, the spectral values of the anomalous region are obtain in the Fourier domain. The inverse Fourier transform then provides a single-frequency image of the anomaly. Different frequencies can be used to fill in the Fourier space data. This is a standard DT implementation and the researchers include a method to account for the attenuation of the eddy currents. The technique does, however, rest on the premise that the source field behaves as a plane wave. The derivation includes effects such as transmission and reflection from an interface, thus, the technique lacks an appropriate underlying physical justification. The main idea of the authors is to obtain a direct inversion of (2.44) using electric field measurements, however, the interpretation as waves is incorrect and should not be used as a basis for inverting eddy current data. Also, the electric field is not actually measured in eddy current tests, instead impedance measurements are used which would further complicate these approaches.

In efforts to directly invert the impedance relationship of (2.45), some researchers have utilized holographic approaches to attempt to backpropagate the eddy current fields by applying holography to eddy current impedance measurements [97-99]. The misconceptions of applying holography to MQS phenomena are described by [103-105], however, this concept is briefly reviewed here for clarity. Holographic approaches are based on the fact that propagating wave fields have a linear phase shift with position and can thus be described as a linear spatial filter. For phenomena governed by wave propagation, a hologram is generated by recording the transducer response as it is scanned over a rectangular aperture in the xy plane at some point $z = z_0$. The complex field in the recording plane $z = z_0$ can be expressed in the form

$$f(x,y,z_0) = |f(x,y,z_0)| \exp[j\theta(x,y,z_0)]. \quad (2.49)$$

Using the holographic technique of backward wave propagation, it is possible to propagate the recorded hologram $f(x,y,z_0)$ which represents the complex scattered wavefront, back to its source, the defect scatterer which interferes with the wave at $f(x,y,z_1)$.

The first step in propagating the hologram plane is to decompose the recorded hologram into its plane wave angular spectrum by applying the two-dimensional Fourier transform as

$$F(u,v,z_0) = \int \int f(x,y,z_0) \exp[-2\pi j(ux + vy)] dx dy. \quad (2.50)$$

The plane wave angular spectrum can now be propagated back to the plane $z = z_1$ by multiplying $F(u,v,z_0)$ by a propagator $P(u,v,\Delta z)$. When propagating to another plane

$z_1 = z_0 + \Delta z$, the wave field f obeys the fully dynamic Helmholtz equation of (2.16) rewritten here as

$$\nabla^2 f + \left(\frac{2\pi}{\lambda}\right)^2 f = 0 \quad (2.51)$$

where λ is the wavelength. Substituting (2.50) into (2.51) yields the relationship for the propagation factor given as

$$P(u,v,\Delta z) = \exp\left[-\frac{j2\pi}{\lambda}\left(\sqrt{1 - (\lambda u)^2 - (\lambda v)^2} \Delta z\right)\right]. \quad (2.52)$$

The propagated hologram can then be reconstructed by taking the inverse Fourier transform of the propagator multiplied by (2.50) as

$$f(x,y,z_1) = \int \int F(u,v,z_0) \exp\left[-\frac{j2\pi}{\lambda}\left(\sqrt{1 - (\lambda u)^2 - (\lambda v)^2} \Delta z\right)\right] \exp[j2\pi(ux + vy)] du dv. \quad (2.52)$$

Thus a wavefront measured at some point z_0 can be reconstructed in any desired plane z_1 in the following steps [68,103].

1. Measure the complex field distribution $f(x,y,z_0)$.
2. Compute the two dimensional Fourier transform of the $f(z,y,z_0)$.
3. Multiply this by a propagation factor to get the Fourier transform of the field at z_1 .
4. Compute the inverse Fourier transform to get the desired field distribution $f(x,y,z_1)$.

As with DT, this algorithm provides a direct solution to the inverse problem which can be easily implemented on a computer. Holography is an established technique used routinely for reconstruction of wave fields. However, it can only be expected to lend a meaningful result if the phenomenon is described as a true wave field.

There have been, however, numerous attempts to utilize holography on eddy current impedance measurements. In all approaches, the similarity of the governing time-harmonic fully dynamic equation (2.16) to the governing MQS equation (2.39) has led researchers to conclude that eddy currents behave as waves. This is an incorrect interpretation because for a typical eddy current frequency, say $f = 10$ KHz, the wavelength in air is one kilometer while the coil is generally less than one millimeter away from the test sample. Thus, there are not sufficient time and phase variations to consider the eddy current coil as launching a wave from air into the material, as many researchers suggest. A major misconception is based on the fact that the induced eddy currents have a sinusoidal phase repetition period of $2\pi\delta$ in the conducting sample, where δ referred to as the "skin depth" and is defined as

$$\delta = \frac{1}{\sqrt{\pi f \mu \sigma}} = \frac{1}{\alpha} = \frac{1}{\beta} \quad (2.54)$$

Since the eddy currents have phase repetitions which are similar to the sinusoidal repetitions of time-harmonic wave fields, they are sometimes erroneously treated as actual propagating wave fields. For a typical eddy current test, the operating parameters are $f=10$ KHz, $\mu = \mu_0$ H/m, $\epsilon = \epsilon_0$ F/m, and $\sigma = 3 \times 10^7$ S/m. Here the displacement current in the sample is

$$\mathbf{J}_d^s = j\omega\epsilon\mathbf{E}^s = j8.85 \times 10^{-10}\mathbf{E}^s \quad (2.55)$$

while conduction current in the sample is given by

$$\mathbf{J}_c^s = \sigma \mathbf{E} = 3 \times 10^7 \mathbf{E}^s \quad (2.56)$$

Clearly, displacement current is negligible compared to conduction current and as the MQS approximations suggest, wave propagation does not occur. Thus, there is no reason to assume that holographic approaches based on wave propagation can be applied to eddy current phenomena [103-104]. This fact appears to be ignored simply because the eddy currents repeat sinusoidally in the conducting sample.

Another justification for using holography on eddy current measurements is a relationship which can be derived from the impedance formula (2.45). It can be shown that there is a linear relationship between impedance phase shifts and the phase shifts of subsurface flaws in a conducting medium. (This relationship is derived in Chapter 5). Also, under certain approximations there is a linear relationship between the phase of a fully dynamic scattered field and the distance to the scatterer. The linear relationship of impedance fields has been used as a justification for treating eddy current phenomena as wave phenomena and subsequently backpropagating impedance measurements with holography, analogously to the backpropagation of wave fields [98]. However, as Chapter 5 points out, the fact that a linear phase relationship exists does not imply that the underlying phenomena is wave based. It can be used to generate images of anomalous regions in the sample, however, the reconstruction algorithms do not attempt to back propagate the measured fields.

In summary, the use of direct “wave-based” inversion techniques such as holography and diffraction tomography which rely on wave attributes such as back propagation have no physical basis for MQS diffusion phenomena. Of course, there may exist mathematical relationships which can be used to invert (2.44) to characterize an anomalous region. However, their use must be physically and mathematically based within an MQS framework.

2.4 Static phenomena

In many NDE applications the governing fields have no time variance and Maxwell's equations for source free regions are written as

$$\nabla \times \mathbf{E} = 0 \quad (2.57)$$

$$\nabla \times \mathbf{H} = 0 \quad (2.58)$$

$$\nabla \cdot \mathbf{E} = 0 \quad (2.59)$$

$$\nabla \cdot \mathbf{H} = 0. \quad (2.60)$$

Because the fields have no time variations, direct inversion methods which utilize variations of time and phase are not applicable. Instead, indirect procedures such as calibration techniques are used to solve the inverse problem [106-107]. Static electric and magnetic phenomena are not discussed in detail here because there seem to be no misconceptions about the appropriate inversion formulas even though the governing partial differential equations can be cast as a Helmholtz equation with $k = 0$.

2.5 Conclusions

This chapter gives a theoretical background in electromagnetic NDE and the associated inverse problem. Clearly the governing electromagnetic phenomena change significantly depending on the operating frequency and material parameters. Varying these parameters results in either fully dynamic, MQS, or static phenomena. These three phenomena have very

different physical properties which affect their associated inverse problems. In general, the inverse problems for all three phenomena are very difficult and often indirect methods such as calibration must be used. There are, however, instances where the fully dynamic inverse problem can be simplified and wave properties such as scattering, time-of-flight, and back propagation can be utilized with appropriate mathematical algorithms to obtain direct inversion techniques that can be used to obtain quantitative images of anomalies in a test sample. These techniques include SAR, diffraction tomography, holography, and many others. Static phenomena, on the other hand have no variations in time and the inversion must be performed with indirect techniques. There is, however, some confusion about MQS phenomena. Here the fields are governed by diffusion instead of wave propagation so wave properties such as scattering, time-of-flight, and back propagation can not be utilized for the solution of the inverse problem. Instead, the inverse problem is generally solved indirectly much like the inverse problem for static electric and magnetic phenomena. This appears to be well understood in the time domain, when the governing parabolic equation and its associated properties are much different from that of the fully dynamic hyperbolic equation. However, for time-harmonic tests, the governing equations of fully dynamic electromagnetic and MQS phenomena take on the same mathematical form. This has led to misconceptions which have resulted in the inappropriate use of wave based inversions on MQS phenomena.

A primary goal of the remaining portion of this dissertation is to demonstrate the differences of MQS and fully dynamic electromagnetic phenomena and to indicate some areas which show potential for the direct inversion of MQS phenomena. Chapter 3 describes experimental imaging results for fully dynamic millimeter wave NDE and MQS eddy current NDE. This helps to demonstrate the associated properties of each technique and also introduces a potential application for millimeter wave NDE. Chapter 4 describes a transformation between hyperbolic and parabolic equations which could potentially provide a method for the direct inversion of MQS diffusion phenomena. Chapter 5 describes a direct

inversion technique which can be used to image subsurface flaws in metals using eddy current NDE. Both an analytic and a numerical study are utilized to demonstrate the underlying foundations of the inversion method, while experimental results are used to demonstrate the limitations associated with applying it to realistic eddy current data.

CHAPTER 3. A COMPARISON OF EDDY CURRENT AND MILLIMETER WAVE NDE

3.1 Introduction

As Chapter 2 shows, the physics of the fully dynamic electromagnetic inverse problem and the MQS inverse problem are quite different. This chapter uses an experimental study to examine the differences in the physical properties and the associated inverse problem of the two systems. To do this, fully dynamic millimeter wave NDE and MQS eddy current NDE are used to inspect surface breaking flaws in an aluminum sample. This type of flaw is chosen because it is potentially detectable by both techniques. A subsurface flaw in aluminum would not be detectable with millimeter wave NDE because the fields attenuate too rapidly, while a flaw in a nonconducting sample would not be detectable with eddy current NDE because there would be no induced eddy currents. There are many NDE situations which require the inspection of surface breaking flaws in conducting materials, for example fatigue cracks on airplane skins.

Eddy current NDE has been used effectively for the detection of fatigue cracks and other surface breaking flaws in conducting materials [108], however, a detracting characteristic is that due to the MQS nature of eddy current phenomena, the eddy current transducer must be placed in close proximity to the test specimen. Since millimeter wave energy can propagate in air, millimeter wave NDE offers an alternative approach with the significant advantage of detection in the stand-off mode of operation. Millimeter wave NDE has been shown to be effective at detecting small flaws [109-112], however, most methods under study require that the transducer be placed in close proximity to the specimen. These methods thus suffer from

the same disadvantages as eddy current techniques. This chapter compares the detection capabilities of surface breaking flaws on conducting materials for conventional eddy current NDE and for millimeter wave NDE in the stand off mode. It provides an insight into the underlying physics and the applicable inversion techniques available for fully dynamic electromagnetic NDE and MQS NDE. It also introduces an application for millimeter wave NDE which has seen little practical implementation.

3.2 Experimental procedure and imaging techniques

3.2.1 Millimeter wave NDE

Millimeter wave phenomena utilize a waveguide antenna to direct electromagnetic energy which is produced in the form of propagating waves. These waves propagate away from the antenna and interact with anomalies which scatter the incident energy. Some of this scattered energy propagates back to the source and can be measured by a network analyzer and subsequently used to characterize the nature of the scattering medium. A schematic of the millimeter wave experimental set up used in this study is shown in Figure 3.1. It consists of a Hewlett Packard 8510C network analyzer system with an operating frequency of 75-110 GHz. The HP 8510C utilizes time-harmonic wave fields, however, through swept frequency measurements and Fourier synthesis, a time-domain pulsed can be generated. The equipment is capable of performing an FFT internally, therefore, for all practical purposes the source acts as a time domain pulse generator. The millimeter wave transducer is a 25 dB Aerowave standard gain horn placed approximately 30 cm from the test sample and is used in the monostatic mode (acting as both transmitter and receiver). The antenna pattern of the horn is shown in Figure 3.2. An aluminum plate with various electrical-discharged machined (EDM)

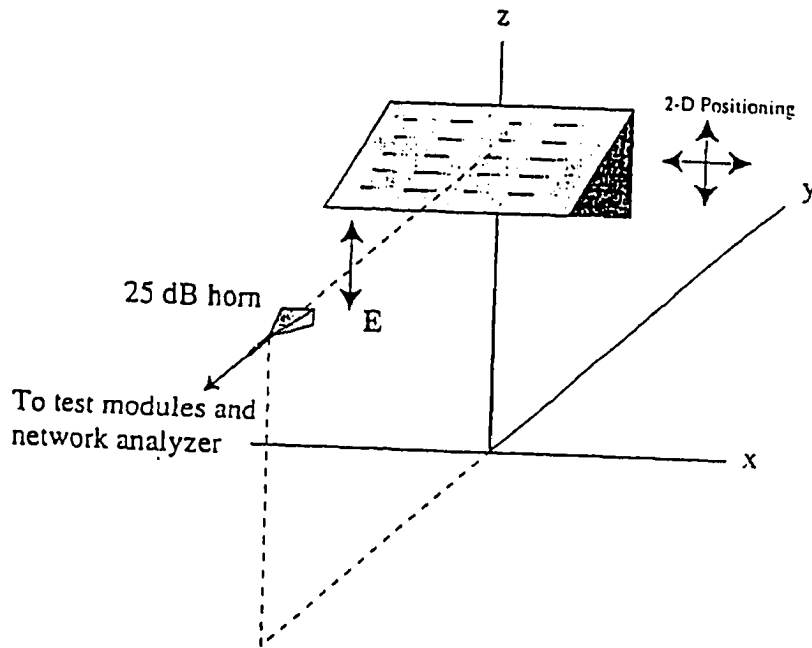


Figure 3.1 Experimental test set up.

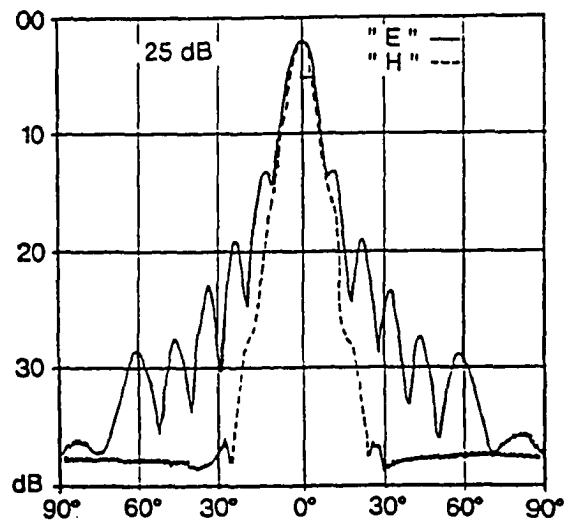


Figure 3.2 Antenna beam pattern [113].

notches is mounted on a 3-D scanning system. The millimeter waves propagate in air to the aluminum sample where the energy is reflected away from the sample according to

$$\mathbf{E}_r = \Gamma \mathbf{E}_i \quad (3.1)$$

where \mathbf{E}_i is the incident time-harmonic wave field and \mathbf{E}_r is the reflected wave field, with the reflection coefficient defined as

$$\Gamma = \frac{\eta_2 - \eta_1}{\eta_2 + \eta_1} \quad (3.2)$$

where

$$\eta = \sqrt{\frac{j\omega\mu}{\sigma + j\omega\epsilon}} \quad (3.3)$$

Medium 1 is well approximated by free space, so

$$\eta_1 = \sqrt{\frac{\mu_0}{\epsilon_0}} = 377 \text{ Ohms/m} \quad (3.4)$$

while for the aluminum plate

$$\eta_2 = \sqrt{\frac{j\omega\mu_0}{\sigma + j\omega\epsilon_0}} = 0.1147 \times 10^{-3} (1 + j) \text{ Ohms/m} \quad (3.5)$$

thus, the reflection coefficient is

$$\Gamma = -0.9994 + j0.0006 = 0.9994 \angle 179.966^\circ. \quad (3.6)$$

The vast majority of the millimeter wave energy is specularly reflected away from the aluminum plate so only a very small fraction actually penetrates the aluminum sample. Note: Although the fields in the metal appear to be in the form of waves, this is not actually the case. The conduction current in the sample is given by

$$\mathbf{J}_c = \sigma \mathbf{E} = 3 \times 10^7 \mathbf{E} \quad (3.7)$$

while displacement current is given by

$$\mathbf{J}_d = \omega \epsilon \mathbf{E} = 5.563 \mathbf{E}. \quad (3.8)$$

Thus, displacement current is negligible compared to conduction current and the MQS approximation holds. Therefore the fields do not behave as decaying waves in the aluminum sample, but rather as MQS diffusion.

In the presence of a flaw, the induced surface currents set up by the impinging electromagnetic wave are disrupted by the flaws and affect the scattered energy. This scattered energy differs from the specularly reflected energy which is seen in the absence of a flaw, however, the specularly reflected energy tends to dominate the signal and make flaw detection difficult. To distinguish this energy from the specularly reflected energy, the sample is placed at a 45 degree angle to the incident wave. The specularly reflected energy is no longer scattered back to the source, so in the absence of a flaw, no return signal is measured. When the incident energy interacts with a flaw, the specularly reflected energy is disrupted and tends to

scatter in all directions from the plate. This scattered energy is now detected with the source horn and can be used potentially to characterize the flaw.

To exploit the frequency range of the system, the source is frequency swept from 75-110 GHz and the signal is subsequently Fourier transformed to obtain a time domain pulse. To decrease the amount of data required for storage, only the maximum of the time domain pulse (P), and subsequent time-of-flight (τ) are recorded for imaging as shown in Figure 3.3. For these tests, the polarization of the electric field is perpendicular to the EDM notch for best results. The amount of scattered energy generated by the EDM notch is directly proportional to the polarization of the incident wave. If the polarization is parallel to the EDM notch, the surface current has very little interruption and subsequently very little scattered energy is produced. When the polarization is perpendicular to the direction of the EDM notch, the maximum amount of surface current is disrupted and there is a large amount of scattered energy produced. Thus, polarization could conceivably be used to determine the orientation of the flaw and thus increase the information content of millimeter wave NDE.

Two different techniques are utilized to image the millimeter wave data. In both cases the antenna is scanned in the X-Z plane with a spatial step of 1 mm as shown in Figure 3.1. The simplest imaging technique consists of plotting the magnitude of the maximum received signal at each C-scan position. This technique can be used to indicate the presence of a flaw. The other imaging technique is synthetic aperture radar (SAR) where the time-of-flight of the maximum returned energy and the pulse amplitude at this time are both utilized to create a focused image [24,112]. The defect is considered to consist of point like flaws and by measuring the time-of-flight of the pulse to the sample and back to the source, the distance from the source to the flaw can be determined. By utilizing measurements along a 2-D baseline perpendicular to the test sample, the position of the flaw can be determined. The SAR algorithm generates 3-D images, however, for simplicity the images shown here consist of the

maximum 2-D slice in the X-Z plane of the total 3-D image. There is a limit to the resolution of SAR imaging with the down range resolution given as [24]

$$\Delta z = \frac{c}{2B} \quad (3.9)$$

where c is the speed of the electromagnetic wave propagation and B is the bandwidth of the swept frequency generated pulse (35 GHz). Thus, the down range resolution of SAR imaging is limited to approximately 8.57 mm. The cross range resolution for a linear SAR as shown in Figure 3.4 is given by [24]

$$\Delta = \frac{cR}{2f_0L} \quad (3.10)$$

where

c = wave speed in the propagating medium

f_0 = center frequency

L = effective aperture dimension

R = observation distance.

The antenna pattern of the source is shown in Figure 3.4 where the 3 dB (half power) point is approximately 5 degrees so the expected cross range resolution is 8.65 mm. This resolution can be increased by using wide beamwidth horns, although, this would have the effect of increasing specular reflection. Consequently, it is not possible to obtain high resolution images of the flaws because the flaw dimensions are in the millimeter range while the resolution limit is almost 1 cm. Thus, for these particular test parameters, SAR is not an ideal method for obtaining information about the flaws, but it does provide a demonstration of how

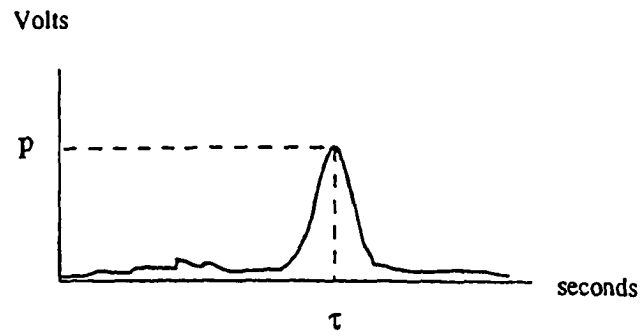


Figure 3.3 Data collection for pulsed measurement.

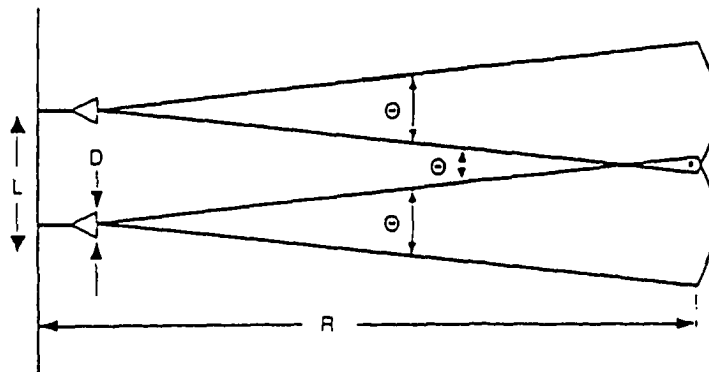


Figure 3.4 SAR crossrange resolution [24].

characteristics of wave propagation can be used to invert fully dynamic electromagnetic fields. To increase the characterization potential of the imaging routine, *a priori* information could be included with a more rigorous imaging algorithm which utilizes calibration techniques. However, this is beyond the scope of this study. The goal here is to demonstrate how features of wave propagation can be utilized to help characterize flaws using millimeter wave NDE. In this setting, the C-scan image is used to analyze the raw data obtained from the experiment, while SAR is used to increase resolution and decrease background noise.

3.2.2 Eddy current NDE

As mentioned in Chapter 2, eddy current testing does not utilize propagating waves but rather MQS induction. The coil is placed in close proximity to the test sample (less than 1 mm) and the eddy currents induced in the sample affect the coil. When these currents are disrupted they cause a change in the source coil that is measured in terms of the complex steady-state impedance. This impedance measurement provides qualitative information about the flaw and can not generally be used to obtain a quantitative reconstruction of the flaw. There have been attempts to invert the impedance formula (2.45) to obtain a profile of surface breaking flaws [93], however, these techniques are limited due to the complex nature of most flaws observed in practice. To obtain a quantitative characterization of the flaw, classification algorithms are generally employed along with reference standards which are generated either computationally or experimentally.

The eddy current NDE experiments utilize the same 3-D scanning system of Figure 3.1, however, the sample is placed flat in the X-Z-plane and an eddy current coil is scanned over the top of the sample with a resolution of 0.25 mm. A Zetec pencil probe with a diameter of 3.175 mm and an operating frequency of 500 KHz is used with a Zetec MIZ-17 eddy current tester to obtain impedance measurements. The eddy current imaging consists of plots of raster scans of

coil impedance changes at each scan location. These images give a qualitative characterization of the flaw but do not provide information such as EDM notch depth which would instead be obtained through classification techniques which are not utilized here.

3.3 Experimental results

A number of experiments were performed in order to compare millimeter wave SAR images and eddy current raster scan images of EDM notches of different lengths, widths, and depths. Figure 3.5 shows images of EDM notches 0.18 mm wide and 0.70 mm deep. Figure 3.5a is an eddy current image of an EDM notch 5 mm long and Figure 3.5b is an eddy current image of an EDM notch 10 mm long. The eddy current coil is easily able to distinguish between the two different length notches, and clearly shows the shape of the EDM notch. Figure 3.5c and 3.5d show millimeter wave SAR images of the same 5 mm long and 10 mm long EDM notches. The SAR images for the two different length notches are very similar and the notch length is not distinguishable from the shape of the image alone. The SAR algorithm lacks adequate cross range resolution because the horns used have very narrow beamwidth. This reduces the number of view angles which can be used to create the image and subsequently limits the focusing ability of the algorithm. Wider beamwidth horns could be used to reduce this problem, however, as mentioned earlier this would have the undesired effect of increased specular reflection from the horn. There are methods to reduce specular reflection effects through signal processing [112], and this is an area for further investigation.

Although the shape of the SAR images does not distinguish the length of the notch, the maximum magnitude of the image is quite sensitive to crack length. This is because the amount of current interrupted is proportional to the notch length. Crack length and direction could possibly be determined with a calibration scheme which utilizes return signal strength and horn polarization. Since the shape of the millimeter wave SAR images shows little variance from

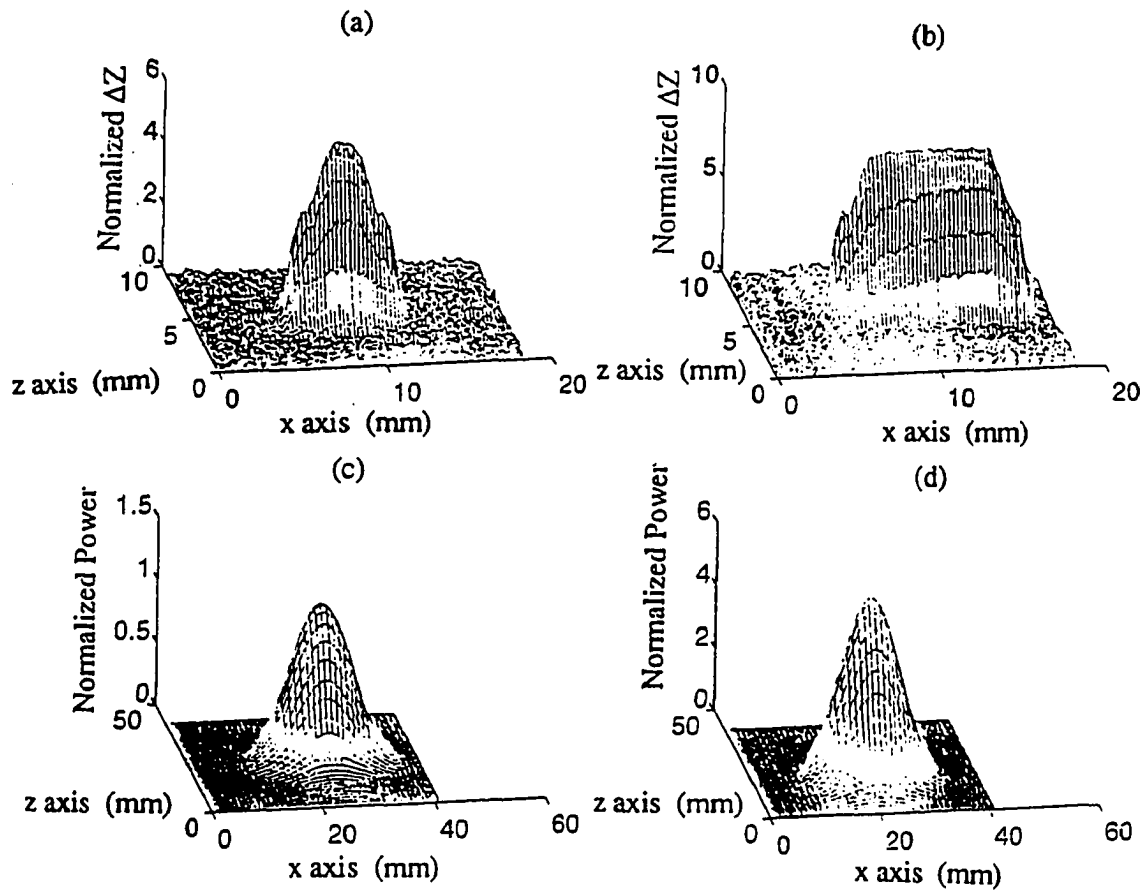


Figure 3.5 Images of EDM notches (0.70 mm deep, 0.18 mm wide) a) eddy current image (length 5 mm) b) eddy current image (length 10 mm) c) millimeter wave image (length 5 mm) d) millimeter wave image (length 10 mm). Note the eddy current scale is one half the millimeter wave scale.

that of Figure 3.5c and Figure 3.5d for all of the EDM notches tested, the following results of eddy current and millimeter wave comparisons show only the maximum amplitude of the resultant image. Figure 3.6 shows results from EDM notches 0.18 mm wide, 10 mm long, and with varying depths. Figure 3.6a is a plot of the maximum eddy current impedance magnitude change vs. EDM notch depth and Figure 3.6b shows a plot of millimeter wave SAR amplitude change vs. EDM notch depth. Both techniques have an increase in return signal strength for a corresponding increase in defect depth, however, after a certain depth there is no increase in millimeter wave return signal strength for a corresponding increase in EDM notch depth. This phenomenon was seen in other experiments and requires further investigation, although, it is possibly caused by the inability of the waves generated by surface currents to propagate out of the deeper notch. Figure 3.7a shows results of eddy current responses to EDM notches 0.70 mm deep, 5 mm long and with varying width. The eddy current probe is sensitive to width changes as expected. It should be noted that although the maximum eddy current signal does not continue to increase for large widths, the small size of the probe would allow the width to be determined from a 2-D raster scan image. Figure 3.7b shows results of millimeter wave signals from EDM notches of varying width. The millimeter wave technique shows good sensitivity to width, and thus compares well with the eddy current technique.

These comparisons have shown that while the millimeter wave technique is sensitive to depth, length, and width; the eddy current technique exhibits superior sensitivity to the stand off millimeter wave inspection. As mentioned earlier, the crossrange resolution of the millimeter wave technique could be improved with a wider beamwidth horn and this should be investigated further. However, millimeter wave NDE appears to be effective at detecting surface defects from large distances away from the test sample and does have significant advantages over other NDE techniques because a couplant is not required. Another significant advantage of the wave-based modality is its ability to interrogate components through dielectric barriers. This is considered next.

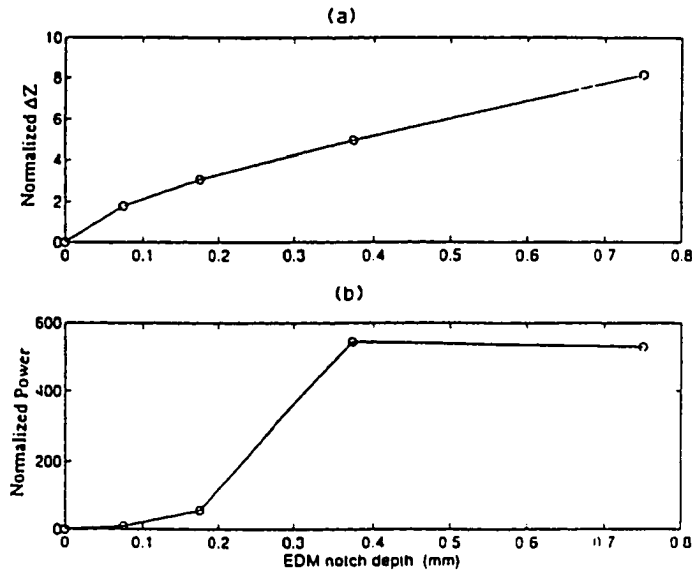


Figure 3.6 Sensitivity to EDM notch depth (length 10 mm, width 0.18 mm) a) eddy current maximum impedance change vs. EDM notch depth b) millimeter wave SAR maximum vs. EDM notch depth.

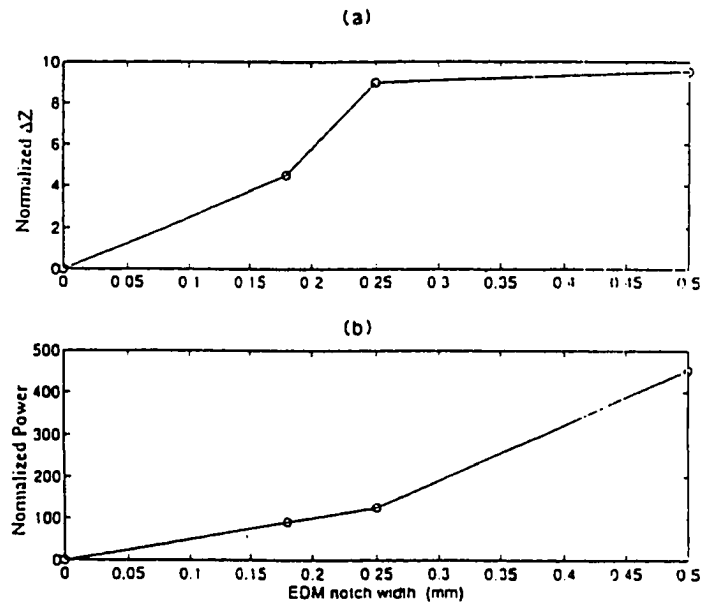


Figure 3.7 Sensitivity to EDM notch width (length 5 mm, depth 0.70 mm) a) eddy current maximum impedance change vs. EDM notch width b) millimeter wave SAR maximum vs. EDM notch width.

3.4 Results from millimeter wave NDE through dielectric materials

A strength of millimeter wave NDE is demonstrated by its ability to image surface defects on aluminum plates covered with thick dielectric materials. For completeness, the covered plates were inspected with the eddy current coil, however, the coil did not have any measurable change in impedance from that of the coil in air. Therefore, eddy current results are not shown in the following figures, and millimeter wave C-scan images are compared to millimeter wave SAR images to demonstrate the benefits of the focusing technique.

The millimeter wave tests were done on an EDM notch 0.45 mm wide, 10 mm long and 1.5 mm deep. A reference image with no covering is shown in Figure 3.8. The C-scan image clearly distinguishes the EDM notch and the SAR image shows a very slight reduction in background noise. Figure 3.9a and 3.9b show C-scan and SAR images of the EDM notch with a 2 cm nonconducting honeycomb composite covering. The C-scan clearly shows the EDM notch as well as the periodic signal variation from the honeycomb itself. The SAR image significantly reduces the background signal from the honeycomb, giving a much clearer image of the EDM notch. Thus, even with limited angular resolution the SAR process has benefits. Figure 3.10a and 3.10b show C-scan and SAR images of the EDM notch covered with 2 mm of corrugated plastic with 10 dB loss/mm and 8 mm of lossless plexiglass. The dielectric loss of the plastic has little effect on the signal due to the large dynamic range of the equipment. Figure 3.11a and 3.11b show C-scan and SAR results from the EDM notch covered with a 10 cm inhomogeneous ceramic material. The image is distorted from the inhomogeneities in the sample, however, the SAR routine reduces the distortion significantly.

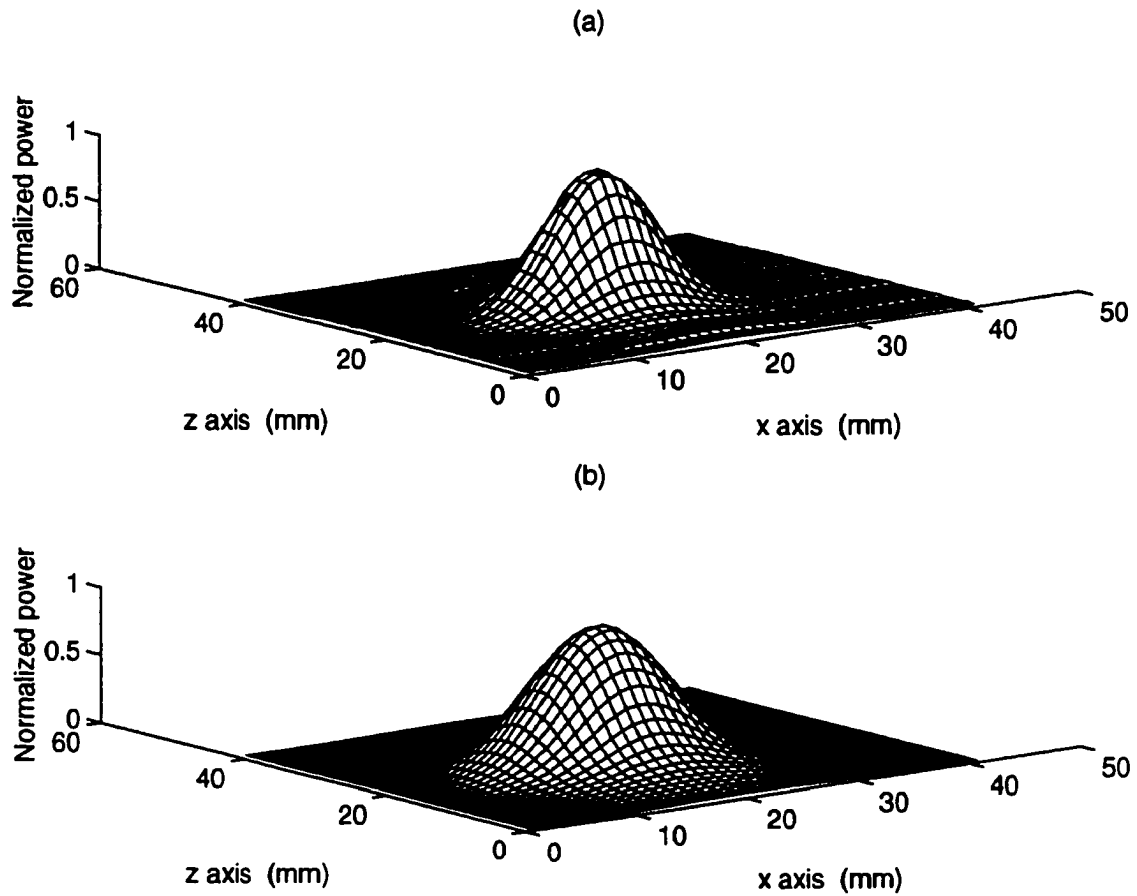


Figure 3.8 Millimeter wave image of EDM notch with no covering (width 0.45 mm, depth 1.5 mm, length 5 mm) (a) C-Scan (b) SAR.

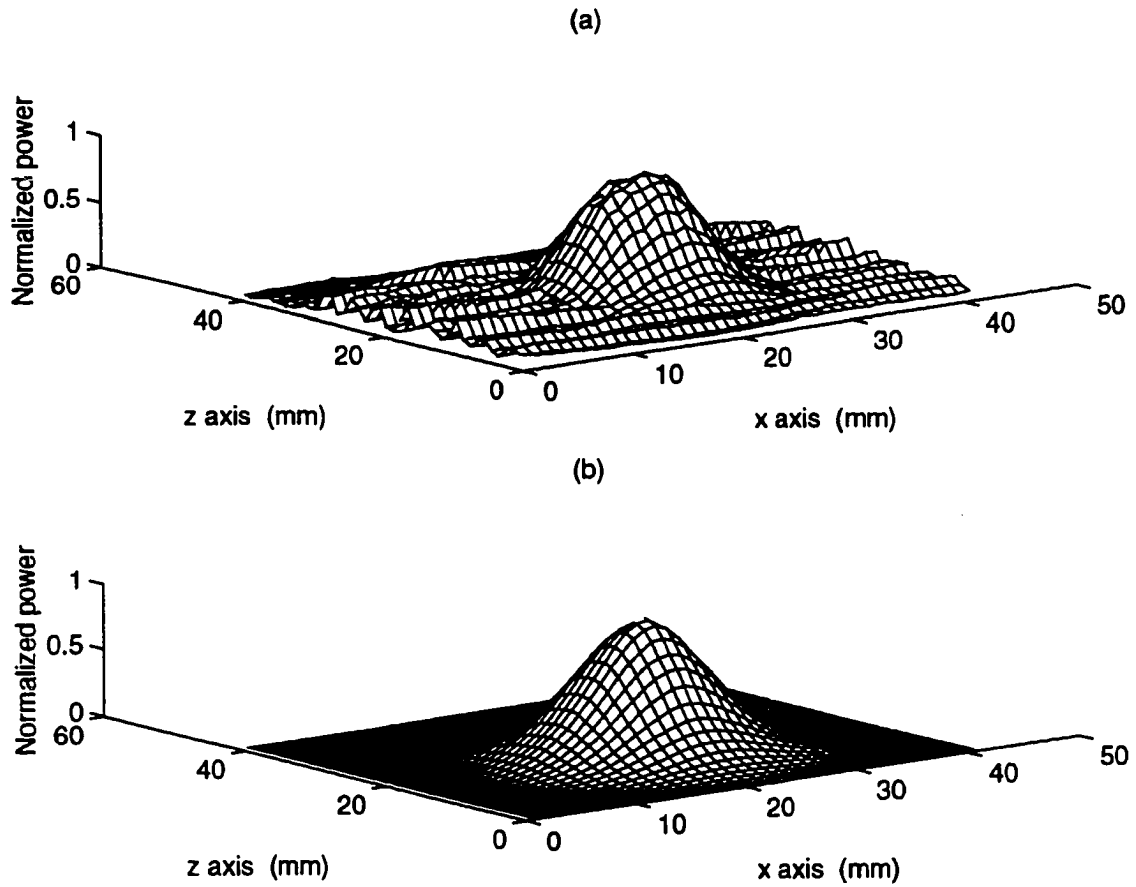


Figure 3.9 Millimeter wave images of EDM notch covered with 2 cm of nonconducting honeycomb composite (a) C-scan (b) SAR

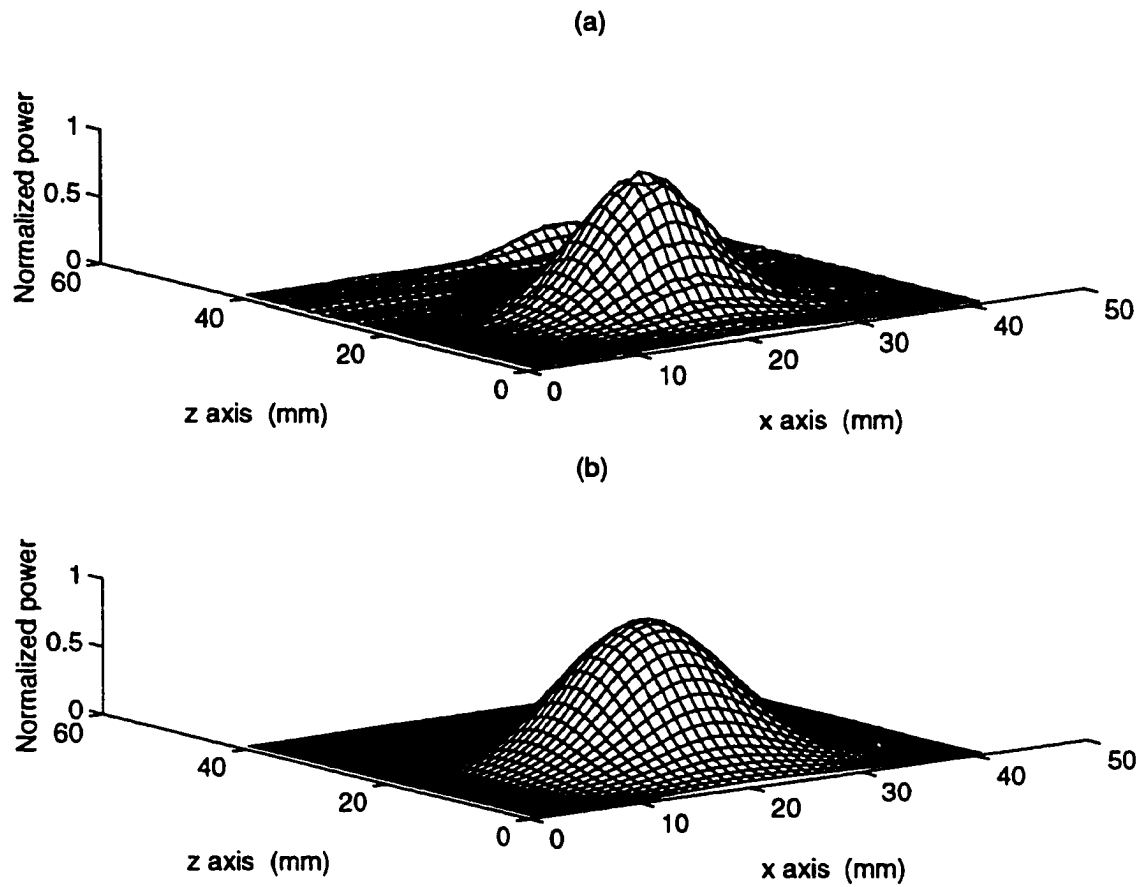


Figure 3.10 Millimeter wave images of EDM notch covered with lossy plastic covering 2 mm thick (loss 10 dB/mm) and 7 mm of lossless plexiglass (a) C-scan (b) SAR

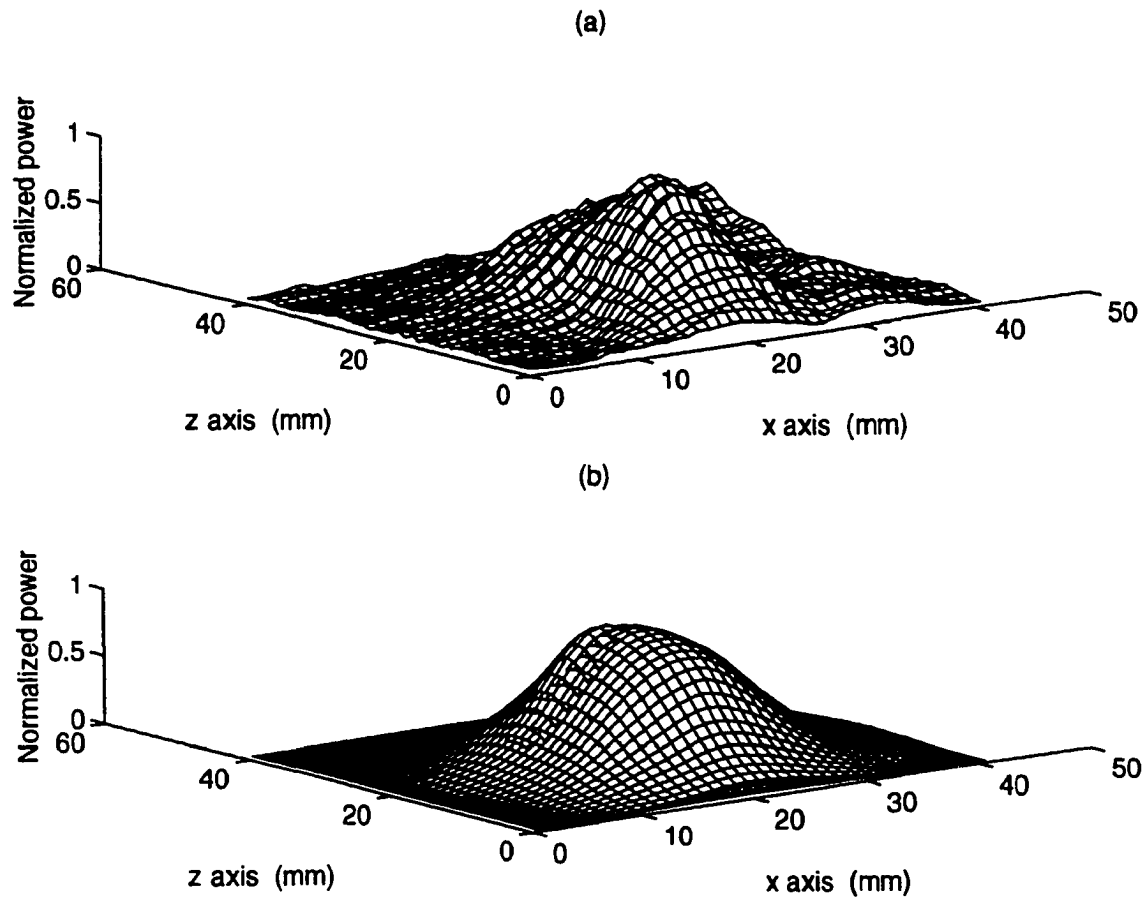


Figure 3.11 Millimeter wave images of EDM notch covered with 7.5 cm of inhomogeneous ceramic (a) C-scan (b) SAR.

3.5 Inspection of tight fatigue cracks

The results presented in the last two sections indicate that millimeter wave NDE can be used in the stand-off mode to detect small EDM notches. It is, however, important to determine if actual fatigue cracks are detectable with the stand-off millimeter wave inspection. To investigate this, a fatigue crack in an aluminum sample is inspected with both eddy current NDE and the stand-off millimeter wave NDE. The fatigue crack was produced at NASA Langley Research Center. It was grown in a 152 mm x 152 mm x 6.35 mm tensile aluminum sample as shown in Figure 3.12. The fatigue crack initiates from a starter notch approximately 1 mm wide where it extends approximately 41 mm in length and penetrates completely through the sample. The sample is inspected with eddy current NDE. The starter notch was not inspected, but rather the end of the fatigue crack. The resultant image is shown in Figure 3.13 and the fatigue crack and its tip are clearly detectable. Next the sample is inspected with millimeter wave NDE. The millimeter wave inspection is performed by scanning the fatigue crack with the horn placed approximately 15 cm from the test sample and the sample oriented at a 45 degree angle. The horn was scanned over both the starter notch and the fatigue crack. To locate the transition region between the starter notch and the fatigue crack, a conducting wire was placed perpendicular to the notch and the beginning of the fatigue crack. The resultant C-scan gray scale image is shown in Figure 3.14a and the notch and the wire are clearly detectable, however, the fatigue crack is not indicated in the image. Figure 3.14b shows a resultant C-scan without the wire indicator, and the notch is once again clearly detectable, but the fatigue crack does not produce a response. Thus, the millimeter wave inspection was unable to detect the fatigue crack, while the eddy current inspection could detect the crack easily. There have been inspections of small cracks with microwave and millimeter wave NDE, however, the transducer was placed quite close to the sample as is done in eddy current inspections, thus suffering from the same limitation as eddy current NDE. Clearly, more

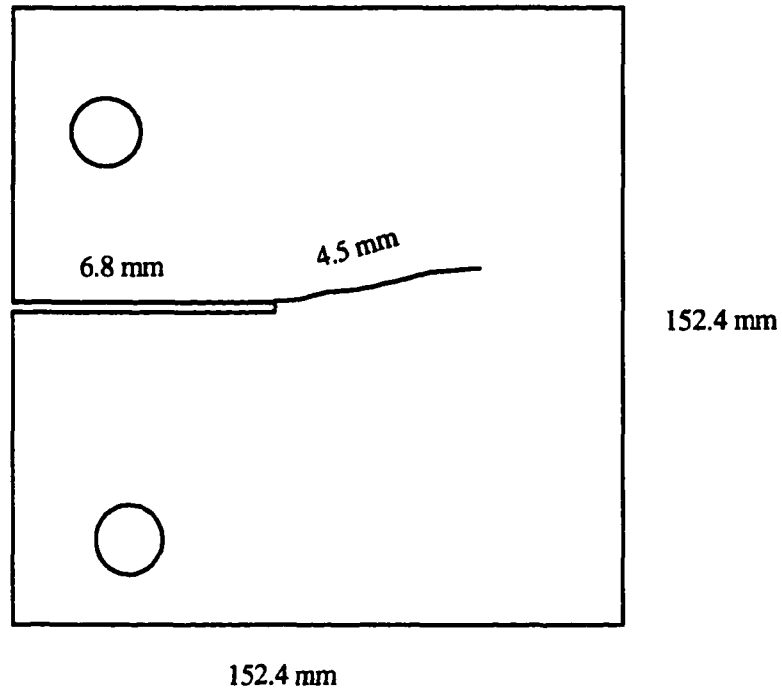


Figure 3.12 Diagram of fatigue crack.

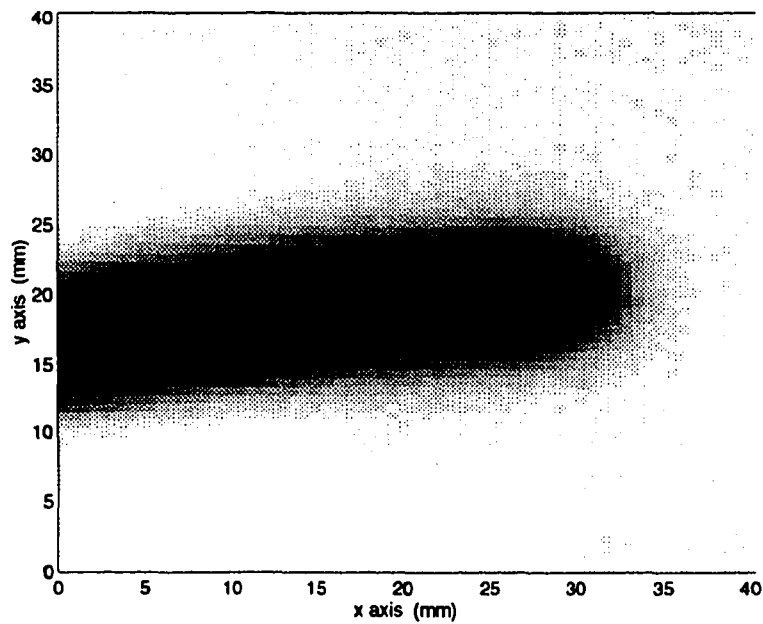
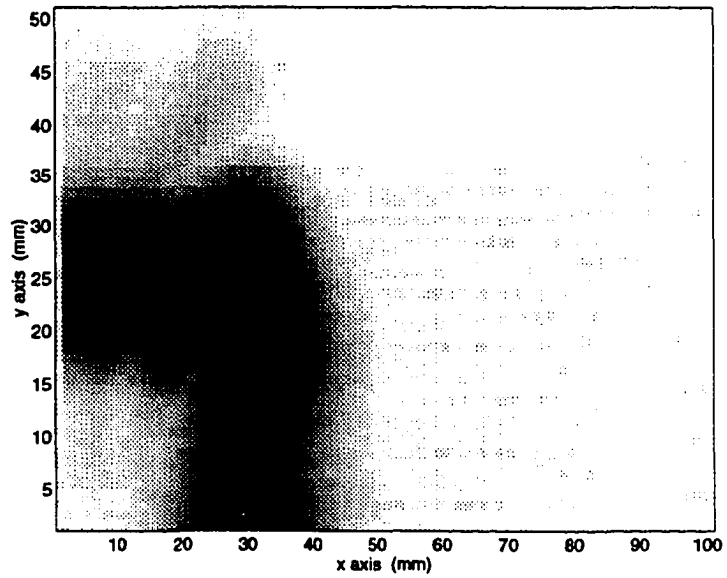


Figure 3.13 Eddy current image of fatigue crack including crack tip. Total scan dimensions (41 mm x 41 mm).

(a)



(b)

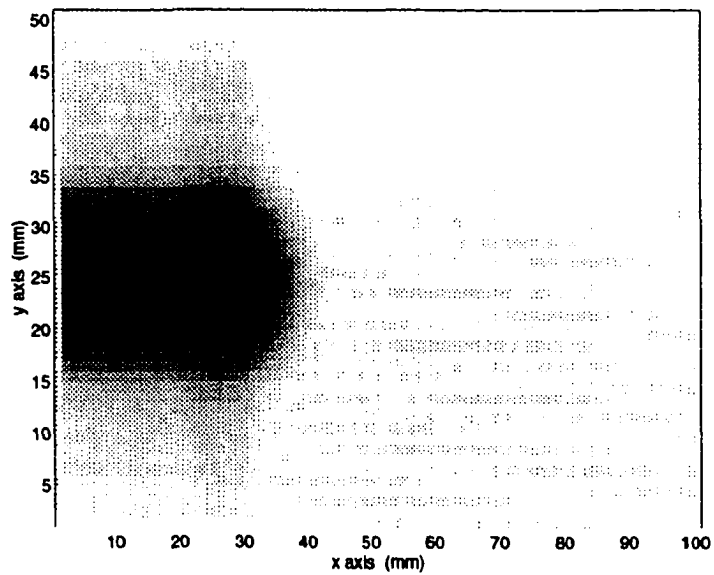


Figure 3.14 C-scan images of millimeter wave inspections of starter notch and fatigue crack (a) with reference wire perpendicular to starter notch and beginning of fatigue crack (b) without reference wire

research must be done in the inspection of fatigue cracks using millimeter wave NDE, however, the preliminary results indicate that very tight fatigue cracks may pose difficulties.

3.6 Conclusions and future work

The purpose of this chapter is to use the inspection of surface breaking flaws in a conducting sample as a means for demonstrating the differences between fully dynamic electromagnetic phenomena and MQS phenomena. The wave nature of fully dynamic fields in air is exploited by using a transducer placed at a large distance from the test sample. Practically, this has the advantage of inspections where access to the sample is limited. This wave nature was further exploited by detecting flaws with the aluminum sample covered by various inhomogeneous dielectric media. In all cases the millimeter waves propagate away from the sample, are scattered by the flaws, and this energy is recorded at the source to detect the presence of the flaw. Subsequent imaging was performed using raw C-scan data and SAR. SAR is a direct "wave based" imaging technique which utilizes the time-of-flight of the waves scattered by the EDM notches.

Since eddy current NDE is governed by MQS induction, the test coil must be placed in very close proximity to the sample. In fact, if a small (2 mm) thick dielectric material is placed on top of the sample, the eddy current coil has no response from the sample and is effectively in air. This clearly demonstrates that the eddy current coil does not launch a wave which is partially reflected and partially transmitted at the surface as some researchers suggest [97-100]. Because eddy current phenomena are not governed by wave propagation, direct "wave-based" imaging algorithms such as SAR, diffraction tomography, and holography can not be applied to the impedance measurements. To utilize a direct quantitative inversion routine for eddy current NDE the impedance relationship (2.45) must be inverted for the particular inspection geometry.

It has been shown that millimeter wave NDE can be effectively used to detect surface breaking EDM notches in aluminum. The millimeter wave technique is sensitive to changes in depth, length and width however, the sensitivity is not as great as that of an eddy current probe. These results have shown that millimeter wave NDE can be used effectively where eddy current techniques are not applicable. The inspection of surface defects in conducting materials where direct access of the test sample is not available appears to be a potential application of millimeter wave NDE. The millimeter wave technique is effective at detecting the EDM notches and SAR can be used to decrease distortion from the inhomogeneities in the covering materials. Although a preliminary study indicates that millimeter wave NDE seems to be unable to detect tight fatigue cracks in the stand-off mode, more work is required to investigate this matter further. A second focus should be to develop a calibration procedure which could not only detect flaws, but utilize horn polarization and return signal strength in conjunction with reference samples to determine the size and shape of actual fatigue cracks.

CHAPTER 4. A DIFFUSION-TO-WAVE TRANSFORMATION FOR INVERTING MQS NDE DATA

4.1 Introduction

Chapter 2 demonstrates that the inversion of phenomena governed by parabolic partial differential equations is much more difficult than that of hyperbolic systems. This is because parabolic systems do not offer useful wavelike features such as time-of-flight and backpropagation in time. Thus, the inversion of parabolic systems is generally done with indirect inversion procedures. However, a potential approach for using wave-based reconstruction techniques on diffusive phenomena is based on a mathematical transformation which exists between hyperbolic and parabolic equations [76-78]. This relationship can be used to observe diffusion data in a wavelike format where it can be subsequently inverted with wavelike procedures [79-82]. Its use is not physically based, rather, diffusive data is manipulated in such a way that it solves a non-physical wave equation. This rearranged data can then be subjected to wave-based inversion schemes. The usefulness of this technique hinges on two points: that the wave-based reconstruction has a physically meaningful interpretation; and, that the procedure for accomplishing the transformation to the hyperbolic domain is robust enough to process faithfully experimental data and its attendant noise. This chapter addresses both of these issues by considering a particularly simple test scenario chosen for the sake of clarity. The ideas developed could possibly be extended to complex geometries, however, this would bring about potential difficulties not addressed in this study.

4.2 The inverse problem

The setting for the inverse problem to be considered is shown in Figure 4.1. It consists of determining the thickness, L , of a slab placed over a perfectly conducting half-space. In order to motivate the wave transformation of the eddy current problem, the thickness of a lossless slab is first obtained as one would using microwave NDE. The inversion procedure in this case consists of observing the time-of-flight to a disturbance and back to the probe. Eddy current data is then generated for a lossy slab and compared to the microwave result. In this case wave propagation does not occur and as such the time-of-flight of a disturbance is not a realizable method of determining the thickness of the slab. However, a transformation is used which allows for the diffusive field to be observed as a wave field.

The governing hyperbolic equation of interest is equation (2.5) written again with a driving term included as

$$\nabla^2 \mathbf{E} - \mu\sigma \frac{\partial}{\partial t} \mathbf{E} - \mu\epsilon \frac{\partial^2}{\partial t^2} \mathbf{E} = \mu \frac{\partial \mathbf{J}_i}{\partial t} \quad (4.1)$$

while the governing parabolic equation is (2.30) written here as

$$\nabla^2 \mathbf{E} - \mu\sigma \frac{\partial}{\partial t} \mathbf{E} = \mu \frac{\partial \mathbf{J}_i}{\partial t}, \quad (4.2)$$

however, for this test scenario it is assumed that the fields vary only in the x direction. In each problem the driving field is a step current in the y direction at the boundary $x=0$, and this current is not a function of y and z . The source term in (4.1) and (4.2) is the time rate of change of the current and is taken to be an impulse function. For the wave equation this

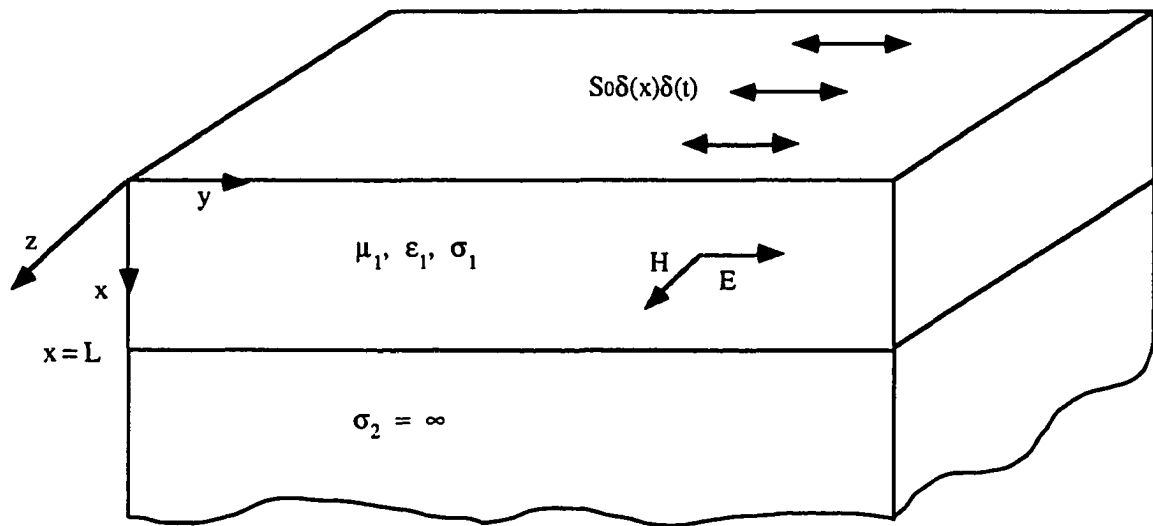


Figure 4.1. 1-D test geometry for both wave and diffusion problems.

impulsive source term is equivalent to an initial rate of change, and for the diffusion equation the impulse is equivalent to an initial value. The continuity requirements on the electric field imply

$$E(L,t) = 0 \quad (4.3)$$

$$\frac{\partial E(0,t)}{\partial x} = 0 \quad (4.4)$$

respectively, since no electric field exists in the perfectly conducting substrate and E is spatially constant in the air.

The problems of interest, shown in Figure 4.1, are thus:

Problem A: EM Waves ($\sigma_1 = 0$)

$$\frac{\partial^2 E}{\partial x^2} - \mu\epsilon \frac{\partial^2 E}{\partial t^2} = -S_0 \delta(x)\delta(t) \quad (4.5)$$

with initial conditions

$$E(x,0) = 0 \quad \frac{\partial E(x,0)}{\partial t} = 0 \quad (4.6)$$

and boundary conditions

$$\frac{\partial E(0,t)}{\partial x} = 0 \quad E(L,t) = 0. \quad (4.7)$$

Problem B: MQS Diffusion ($\sigma_1 \gg 1$)

$$\frac{\partial^2 E}{\partial x^2} - \mu\sigma \frac{\partial E}{\partial t} = -S_0 \delta(x)\delta(t) \quad (4.8)$$

with initial condition

$$E(x,0) = 0 \quad (4.9)$$

and boundary conditions

$$\frac{\partial E(0,t)}{\partial x} = 0 \quad E(L,t) = 0. \quad (4.10)$$

In each case the inverse problem is to determine where the boundary L is from measurements at $x = 0$. As Chapter 2 points out, for Problem A the boundary information must travel along the characteristic lines as shown in Figure 2.4. The information travels with finite propagation speed $c = 1/\sqrt{\mu\epsilon}$. Since the boundary is treated as a perfect conductor, there is complete reflection at the interface, and the initial disturbance travels along the characteristic lines back to the surface. An observer at $x=0$ can determine the distance to the boundary by the time the disturbance takes to travel to the boundary and return. The solution to (4.5)-(4.7) is given by

$$E(x, t) = \sum_{n \text{ odd}} \frac{S_0^4}{\sqrt{\mu\epsilon} n \pi} \sin\left(\frac{n \pi}{2 L \sqrt{\mu\epsilon}} t\right) \cos\left(\frac{n \pi}{2 L} x\right) \quad (4.11)$$

and is shown in Figure 4.2. The plot shows that the wave field at the surface has a constant value until the disturbance from the boundary interacts with the surface field. Since the disturbance must travel on the characteristic lines with finite speed it is not felt at the surface for

a finite time $t = 2L/c$. The inverse problem of determining the thickness of the slab is accomplished by reading the time that the first disturbance is felt and calculating L directly. The inverse problem can be solved directly without the need for calibration methods and *a priori* knowledge.

Now consider the inspection of a slab of finite conductivity ($\sigma_1 \gg 1$) shown in Figure 4.1 and governed by Problem B. For Problem B the characteristic equations are given on the lines $t = \text{"constant"}$ as shown in Figure 2.6. Information throughout the domain is propagated immediately on these lines resulting in a smooth solution for $t > 0$. The solution of (4.8)-(4.10) is

$$E(x,t) = \sum_{n \text{ odd}} \frac{S_0^2}{L\mu\sigma} \exp\left(-\left(\frac{n\pi}{2L\sqrt{\mu\sigma}}\right)^2 t\right) \cos\left(\frac{n\pi}{2L}x\right). \quad (4.12)$$

A plot of this solution at $x = 0$ is given in Figure 4.3 and shows that, unlike the wave case, the diffusive solution (4.12) does not give any direct information about the thickness of the slab. Though in the solution, the information is embedded in a way which makes the inverse problem difficult. A standard calibration procedure could be used in which signals from specimens of unknown thickness are compared to signals from those of known thickness. An issue is the feasibility of obtaining this information using a direct wave-based reconstruction without the need for a calibration procedure.

4.3 The inverse Q transform

There is a formal manipulation which re-expresses the hyperbolic Problem A in the form of the parabolic Problem B [76-78]. This transformation is invertible and has been considered

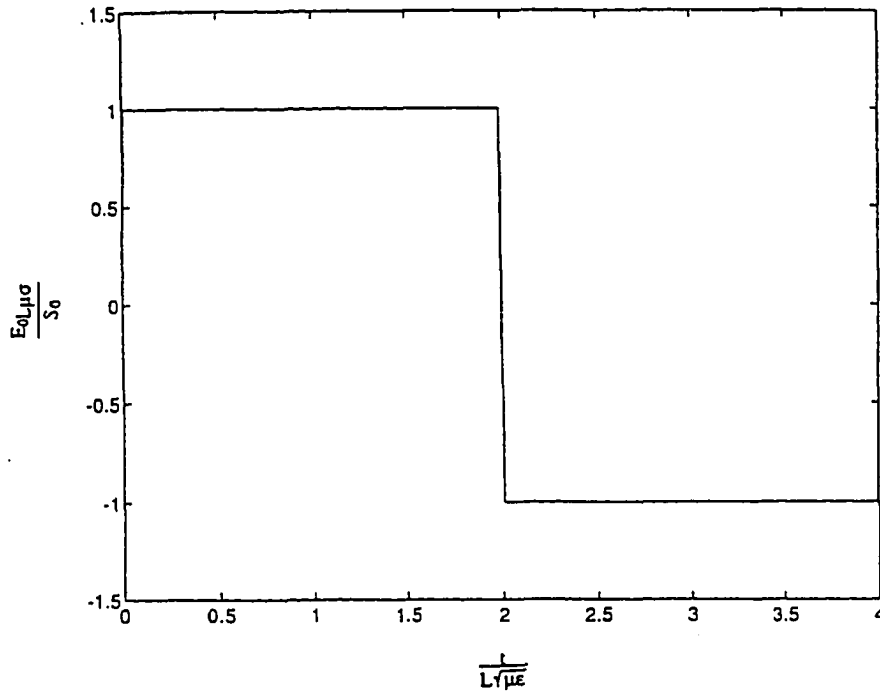


Figure 4.2 Wave field of equation (4.11)

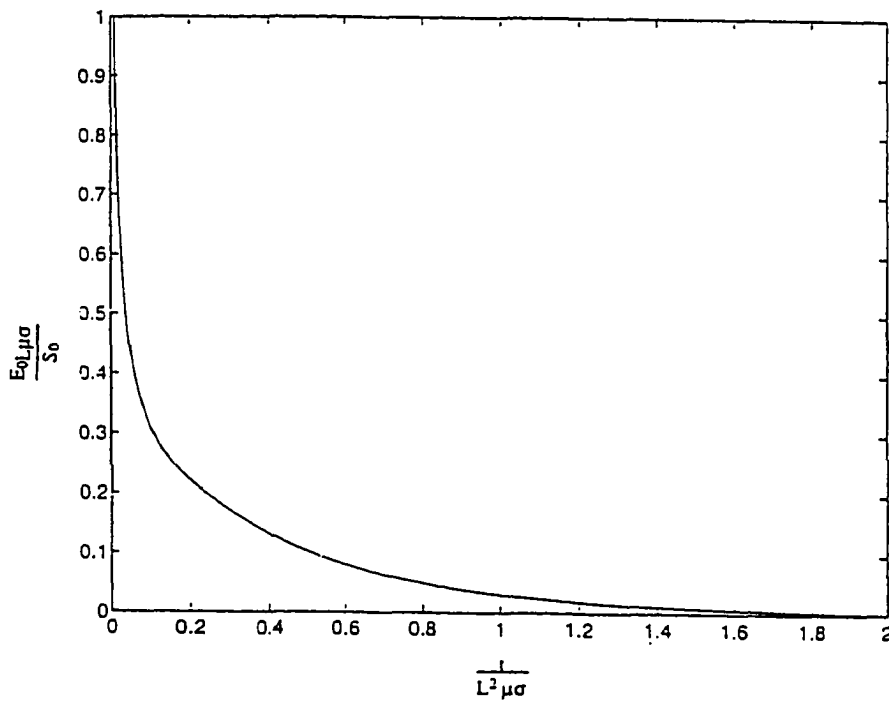


Figure 4.3 Diffusion field of equation (4.12)

as a means of interpreting seismic data [79-81]. To differentiate the physical diffusion field, E , from its hyperbolic transform, U , and to allow for non-ideal sources, Problem A and Problem B are recast as

Problem A':

$$\frac{\partial^2 U}{\partial x^2} - \mu \epsilon' \frac{\partial^2 U}{\partial q^2} = F(x, q) \quad (4.13)$$

with initial conditions

$$U(x, 0) = U_0(x) \quad \frac{\partial U(x, 0)}{\partial q} = U_{q0}(x) \quad (4.14)$$

and boundary condition on Γ

$$U(\Gamma, q) = U_\Gamma(q) \quad (4.15)$$

where the physical conductivity σ plays the role of permittivity ϵ' , and

Problem B':

$$\frac{\partial^2 E}{\partial x^2} - \mu \sigma \frac{\partial E}{\partial t} = S(x, t) \quad (4.16)$$

with initial condition

$$E(x, 0) = E_0(x) \quad (4.17)$$

and boundary condition on Γ

$$E(\Gamma, t) = E_{\Gamma}(t). \quad (4.18)$$

The diffusive Problem B' can then be related to Problem A' by taking the Laplace transform of each equation and matching like terms, resulting in

$$\int_0^{\infty} E(t) \exp(-p^2 t) dt = \int_0^{\infty} U(q) \exp(-p q) dq \quad (4.19)$$

or equivalently

$$\int_0^{\infty} E(t) \exp(-s t) dt = \int_0^{\infty} U(q) \exp(-\sqrt{s} q) dq. \quad (4.20)$$

The above equations are the fundamental relationships between the wave and diffusion domains. A transformation from an artificial wave domain to a physical diffusion domain known as the Q transform (QT) can be derived by taking the inverse Laplace transform of (4.20) giving

$$E(x, t) = \frac{1}{2\sqrt{\pi t^3}} \int_0^{\infty} q \exp(-q^2/4t) U(x, q) dq \quad (4.21)$$

$$S(x,t) = \frac{1}{2\sqrt{\pi t^3}} \int_0^{\infty} q \exp(-q^2/4t) F(x,q) dq \quad (4.22)$$

$$E_{\Gamma}(t) = \frac{1}{2\sqrt{\pi t^3}} \int_0^{\infty} q \exp(-q^2/4t) U_{\Gamma}(q) dq \quad (4.23)$$

$$E_o(x) = U_{qo}(x). \quad (4.24)$$

Although (4.21)-(4.24) is a relationship between wave fields and diffusive fields, for the purpose of processing diffusive eddy current data it is more useful to have an algorithm which transforms diffusive data to its wave counterpart. This requires the inverse Laplace transform from p to q of (4.19) which gives

$$U(x,q) = \frac{1}{2\pi j} \int_{\alpha - j\infty}^{\alpha + j\infty} \int_0^{\infty} E(x,t) \exp(-p^2 t) dt \exp(p q) dp \quad (4.25)$$

$$F(x,q) = \frac{1}{2\pi j} \int_{\alpha - j\infty}^{\alpha + j\infty} \int_0^{\infty} S(x,t) \exp(-p^2 t) dt \exp(p q) dp \quad (4.26)$$

$$U_{\Gamma}(q) = \frac{1}{2\pi j} \int_{\alpha - j\infty}^{\alpha + j\infty} \int_0^{\infty} E_{\Gamma}(t) \exp(-p^2 t) dt \exp(p q) dp \quad (4.27)$$

$$U_o(x) = 0 \quad (4.28)$$

$$U_{qo}(x) = E_o(x). \quad (4.29)$$

Equations (4.25)-(4.29) transform a diffusive field to a wave field and are referred to as the inverse Q transform (IQT). These relationships are summarized in Table 4.1 while Table 4.2 lists some useful transform pairs. Significantly, the rate of exponential decay in the diffusive domain corresponds to a sinusoidal frequency in the wave domain. Therefore, the initial moments of diffusion characterized by a set of decaying exponentials contains the highest frequency information of the pseudo wave.

The IQT is now applied as an inversion scheme to re-express the results of Figure 4.3 in a more meaningful format. The diffusion field is transformed and observed as a pseudo wave field for which the thickness of the slab can be determined through time-of-flight measurements as in the wave case presented in Problem A. Substituting the diffusive field $E(x,t)$ from (4.12) into the IQT gives a pseudo-wave field

$$U(x, q) = \sum_{n \text{ odd}} \frac{S_0^4}{\sqrt{\mu\sigma n\pi}} \sin\left(\frac{n\pi}{2L\sqrt{\mu\sigma}} q\right) \cos\left(\frac{n\pi}{2L} x\right). \quad (4.30)$$

This, of course, is also the solution to the EM wave Problem A, demonstrating that diffusive data can be converted to wave data. Thus, wave-based inversion schemes which rely on time-of-flight measurements could be used to determine the thickness of the slab even though the situation is truly diffusive.

4.4 Algorithm robustness

An analytic solution was used in the inversion scheme of Section 4.3, but in order to be of practical significance, the algorithm must handle non-ideal data as well. The procedure is ill-

Table 4.1. Summary of transform parameters

Terms	Physical Diffusion	Mathematical Wave
Field	$E(x,t)$ V/m	$U(x,q)$
Length	x meters	x meters
Time	t seconds	q (seconds) ^{1/2}
Source	S	F
Initial Data	$E_0(x)$	$U_{\infty}(x)$
Temporal Frequency	s radians/second	p radians/(seconds) ^{1/2}

Table 4.2. Transform pairs.

Diffusion	Wave
$\delta(t)$	$\delta(q)$
$\exp(-at)$	$\frac{\sin(\sqrt{a} q)}{\sqrt{a}}$
a	aq
$\frac{a^n}{n!}$	$\frac{aq^{2n+1}}{(2n+1)!}$
$\sin(\omega t)$	$\frac{1}{\sqrt{2\omega}} \left[\sin\left(\sqrt{\frac{\omega}{2}} q\right) \cosh\left(\sqrt{\frac{\omega}{2}} q\right) - \cos\left(\sqrt{\frac{\omega}{2}} q\right) \sinh\left(\sqrt{\frac{\omega}{2}} q\right) \right]$
$\cos(\omega t)$	$\frac{1}{\sqrt{2\omega}} \left[\cos\left(\sqrt{\frac{\omega}{2}} q\right) \sinh\left(\sqrt{\frac{\omega}{2}} q\right) + \sin\left(\sqrt{\frac{\omega}{2}} q\right) \cosh\left(\sqrt{\frac{\omega}{2}} q\right) \right]$

posed, however, in that the transformed field exhibits an extreme sensitivity to the diffusive data. This is not surprising since the IQT is a relationship that inverts the QT, a Fredholm integral of the first kind, which is well understood to be unstable [114]. This lack of robustness can be exhibited in the way a small sinusoidal perturbation coupled with a small constant shift to the diffusive data is transformed:

$$E(t) = E_{\text{exact}}(t) + E_{\text{pert}}(t) \quad (4.31)$$

where

$$E_{\text{pert}}(t) = \varepsilon \sin(\omega t) + \gamma. \quad (4.32)$$

From Table 4.2 the perturbation is observed in the wave domain as

$$U_{\text{pert}}(q) = \frac{\varepsilon}{\sqrt{2\omega}} \left[\sin\left(\sqrt{\frac{\omega}{2}}q\right) \cosh\left(\sqrt{\frac{\omega}{2}}q\right) + \cos\left(\sqrt{\frac{\omega}{2}}q\right) \sinh\left(\sqrt{\frac{\omega}{2}}q\right) \right] + \gamma q. \quad (4.33)$$

The small sinusoidal perturbation of the diffusion field grows exponentially in the hyperbolic domain and the constant shift grows linearly which implies that the IQT is unstable to such perturbations.

In order to implement the IQT with experimental data it must be truncated and discretized. The truncated inner integral typically yields terms that exhibit exponential growth when integrated along an imaginary axis in the p -domain. The inner truncation therefore gives rise to an instability that worsens as the limits of the outer integral are extended. This complicates the direct application of the IQT to experimental data. On the other hand, the IQT could be used along with any set of transformable functions used to describe the data set, although this would

reduce the inversion to a calibration procedure which can be done more simply in the diffusive domain.

To bypass this lack of numerical robustness in the IQT, the QT can be discretized and then inverted algebraically. Fredholm integral inversions of this type were considered unsolvable at one time [115], however, as discussed by Tikhonov [114], various methods of regularizing the problem are now available. A common method of regularization is to cast the integral equation in matrix form and use various techniques to stabilize the condition number of the matrix, i.e., eliminate small singular values. This allows the matrix to be inverted thus giving the IQT in a discretized form. The approach is used in [80] and is also developed here.

First the QT is cast as a matrix equation given as

$$\bar{\mathbf{A}} \mathbf{U} = \mathbf{E} \quad (4.34)$$

where the vector \mathbf{U} is the unknown wave field and \mathbf{E} is the diffusive data. The matrix $\bar{\mathbf{A}}$ can be expected to be ill-conditioned since the kernel of the integral decays with increasing q . This can be verified by taking the singular value decomposition of $\bar{\mathbf{A}}$ as

$$\bar{\mathbf{X}} \bar{\mathbf{\Lambda}} \bar{\mathbf{V}}^T \mathbf{U} = \mathbf{E} \quad (4.35)$$

with the inverse operation

$$\mathbf{U} = \bar{\mathbf{V}} \bar{\mathbf{\Lambda}}^{-1} \bar{\mathbf{X}}^T \mathbf{E}. \quad (4.36)$$

Consider the original diffusion Problem B of determining the thickness of a metal slab over a perfectly conducting half space. Instead of performing the IQT analytically as before, numerical data obtained by discretizing Figure 4.3 is used in the algebraic inversion of (4.34).

A diffusion time domain sampling interval of 10^{-2} units is used, 400 diffusion values are sampled, and 400 wave values calculated. It is found that increasing this number beyond 400 does not greatly improve the transformed wave field.

With no regularization the inversion is unstable and the wave data can not be meaningfully interpreted as expected because of the high condition number of $\bar{\Lambda}$, so some form of regularization must be used in carrying out this inversion. Small amounts of regularization provide significant improvement in robustness with the disadvantage of losing high frequency wave information. Two different methods of accomplishing this were investigated.

The first method of regularization is simply to eliminate all singular values in $\bar{\Lambda}$ below a given threshold. Two different threshold values are considered, and although both gave stable wave fields, there are significant differences in the transformed fields. Figure 4.4a shows a wave field obtained from inverting the noise free diffusion field. With a threshold value of 10^{-5} the wave field is regularized enough to have good agreement with the wave obtained analytically using (4.11), shown here and in all subsequent plots as a solid line. There are oscillations present and the field lacks the high frequency terms required for a sharp cutoff at 2 units. If the threshold is increased to 10^{-3} there are fewer oscillations present, but the field degrades at the wave front. The wave field is only shown up to 4 units, after this the wave field quickly degrades to zero. This is expected since the small singular values which are eliminated with the regularization procedure correspond to wave fields associated with large values of q .

The numerical oscillations vary with the value of threshold used, and an average of the wave fields obtained for a range of threshold values tends to smooth out these unwanted perturbations. Figure 4.4b is the wave field obtained from averaging one hundred transformed fields calculated for stable threshold values between 10^{-10} and 10^{-2} . The wave field does not have the oscillations of the previous figure and follows the exact wave field closely at the

wave front. From this wave field an accurate estimate of the thickness of the slab can be observed.

Next, Tikhonov regularization is used to make the inversion process more robust. A regularization parameter α was added to the singular values:

$$\mathbf{U} = \bar{\mathbf{V}} (\bar{\Lambda}^2 + \alpha)^{-1} \bar{\Lambda} \bar{\mathbf{X}}^T \mathbf{E}. \quad (4.37)$$

The parameter α can be optimized in many different ways [116-120] and its choice seems to be application dependent. For this study specific values of α were chosen to give insight into the effect of this parameter on stabilizing the inversion process and optimization was not considered. Figure 4.4c shows the results from Tikhonov regularization with two different values of α . The results are similar to those of Figure 4.4a; for a small α the fields have more oscillations, but the high frequency terms are not damped out which allows the exact wave front to be followed closely. For large α the fields are smoother, but do not follow the wave front as closely, demonstrating the damping of high frequencies in the wave domain through regularization. Figure 4.4d shows results from Tikhonov regularization where one hundred wave fields regularized with α between 10^{-20} and 10^{-10} have been averaged. Once again, the averaging greatly improves the result, the field has almost no oscillations and follows the exact field very closely. From Figure 4.4 it can be seen that both regularization schemes give comparable results and in both cases averaging the stable fields greatly improves the transformed wave field. By using the wave field of Figure 4.4d and the fact that the first wave boundary disturbance at the surface is felt at $q = 2L\sqrt{\mu\sigma}$, the inverse problem of finding the thickness L could be solved using time-of-flight wave-based techniques, demonstrating that a diffusion field can be transformed to a wave field where straightforward wave-based inversion such as time-of-flight can be applied.

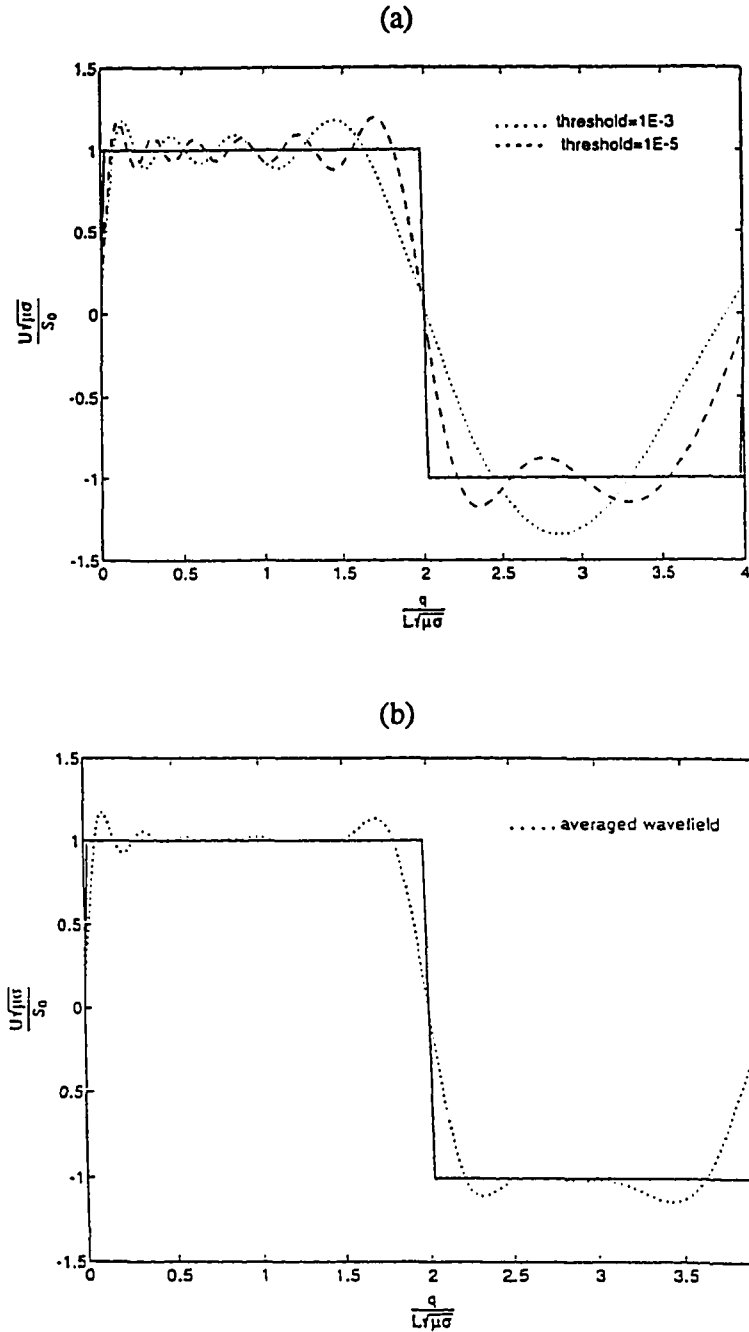
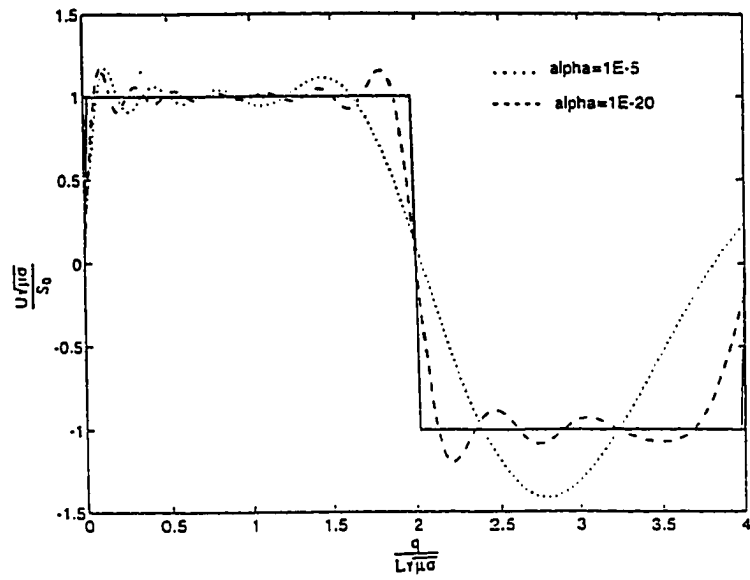


Figure 4.4 (a) Transformed wave field with regularization obtained by eliminating singular values below a given threshold (b) Transformed wave field obtained by averaging 100 stable fields regularized by eliminating singular values below a given threshold.

(c)



(d)

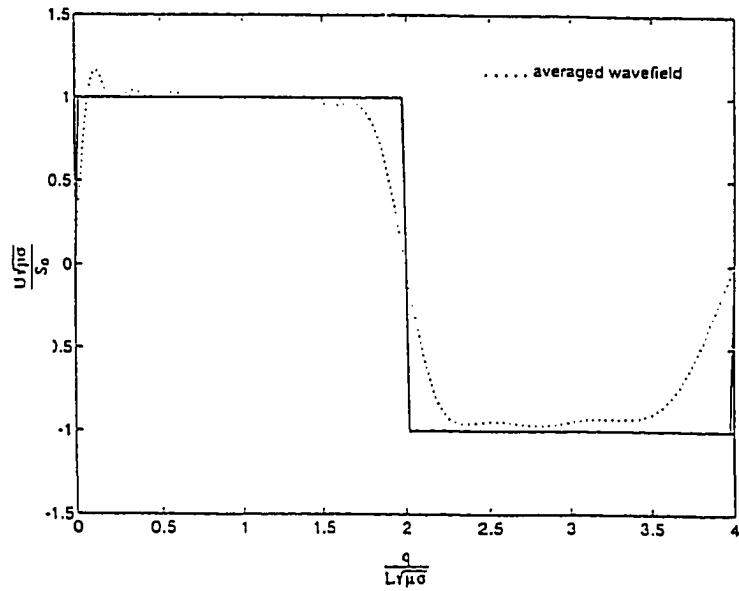


Figure 4.4 continued; (c) Transformed wave field using Tikhonov regularization (d) Transformed wave field obtained by averaging 100 stable fields inverted with Tikhonov regularization.

An interesting aspect of the inversion process is observed by using a smaller minimum sampling time in the diffusive domain which has the effect of including more higher order rates of decay in the diffusive solution. As shown in Table 5.2, exponential rates of decay in the diffusion domain transform to sinusoidal frequencies in the wave domain. Thus, the inclusion of higher rates of decay in the diffusion domain will introduce high frequency modes in the wave domain which require more regularization in the inversion algorithm. When this is done for a given set of data, α must be increased in order to damp out these higher order frequency terms. This is shown by repeating the inversion of the diffusive field using Tikhonov regularization shown in Figure 4.4c. Now the minimum sampling time in the diffusion domain is reduced from 10^{-2} units to 10^{-5} units, with the previous sampling interval and number of points the same. The new wave field is shown in Figure 4.5 and is unstable with the same α of 10^{-20} . This instability is directly attributable to the higher frequency terms which require greater regularization. There is a tradeoff between stability and information content which must be balanced in the inversion.

The regularized IQT is only a useful algorithm if it can be applied to experimental measurements and so it must be sufficiently robust to process noisy data faithfully. Therefore, noise was added to the diffusion field of Figure 4.3 with a signal to noise ratio (SNR) of 40 dB, as defined by

$$\text{SNR} = 10 \log \frac{\sigma_s^2}{\sigma_n^2} \quad (4.38)$$

where σ_s^2 is the variance of the signal and σ_n^2 is the variance of the noise. The diffusion data is shown in Figure 4.6a, and Figure 4.6b shows wave fields obtained by eliminating the singular values in the matrix $\bar{\Lambda}$ below a specified threshold. It is clear that the noise in the diffusion field has a large effect on the inversion scheme. The oscillations are much larger than those

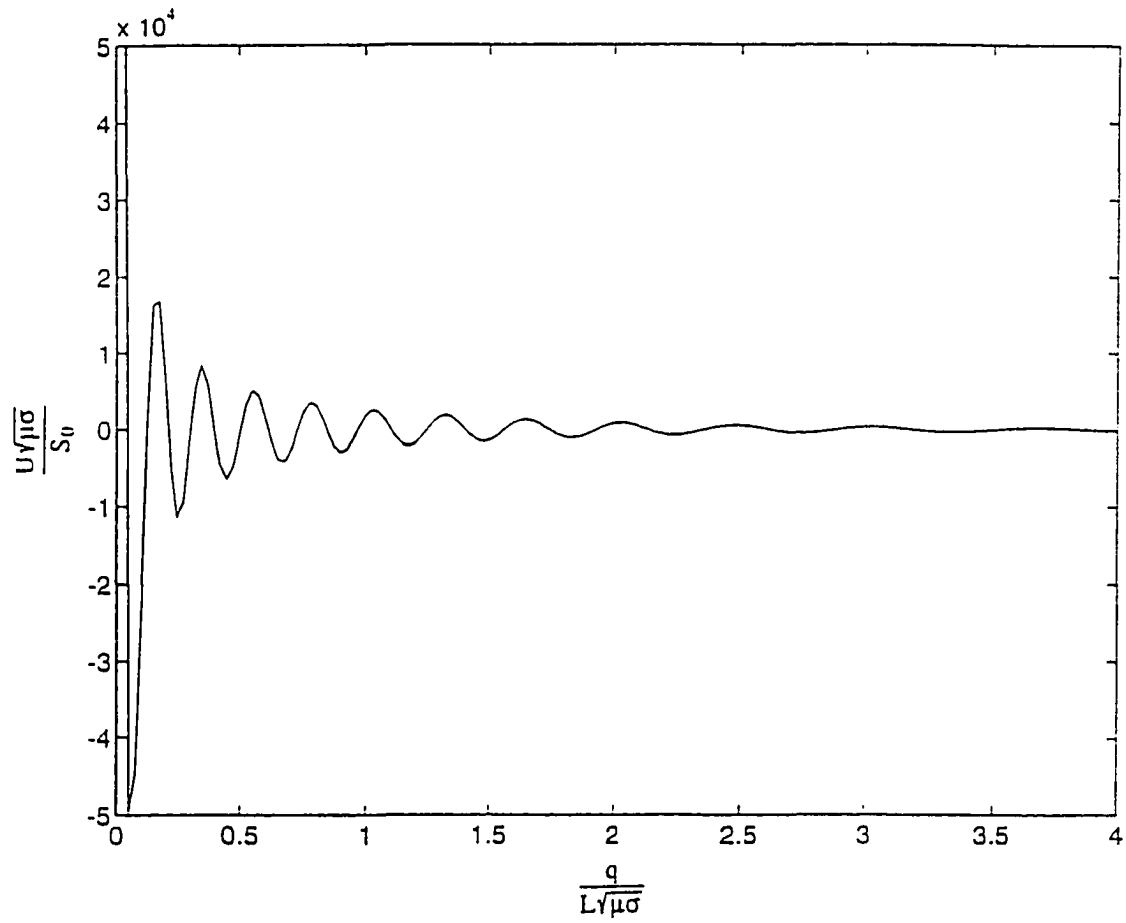
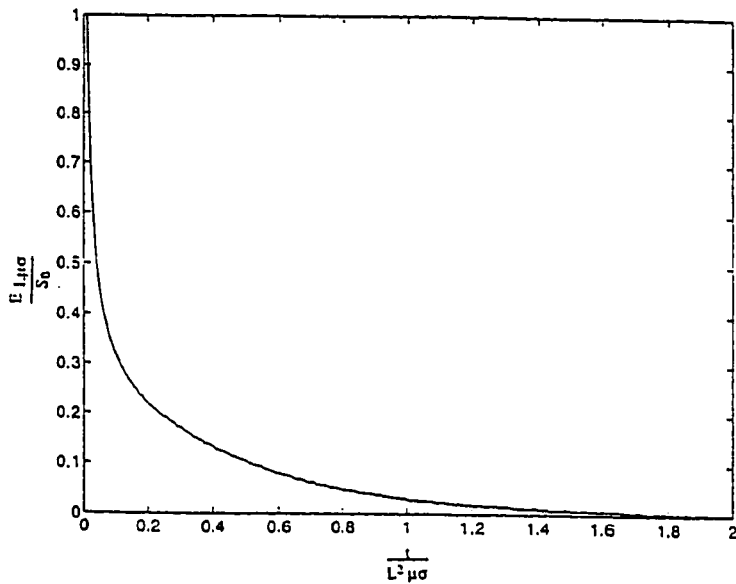


Figure 4.5 Wave field obtained with minimum sampling time in diffusion domain reduced to include higher rates of decay which result in unstable wave modes.

from the inversion of the noise free diffusion field, and the transformed data does not follow the analytic solution closely at the wave front. The threshold singular values therefore had to be chosen larger than those of the noise free inversion to stabilize the transformed field. Increasing the threshold from 10^{-3} to 10^{-1} only slightly decreased the oscillations. Figure 4.6c shows the wave field calculated by averaging one hundred wave fields obtained from inversions with different singular value thresholds. The oscillations are now damped out considerably, however, there are not enough high frequency terms to allow the transformed data to follow the analytic wave front very closely. Figure 4.6d shows the wave fields obtained from Tikhonov regularization. Once again, the noise has corrupted the inversion considerably and α had to be chosen much larger to stabilize the inversion of the noisy diffusion field than was needed for inversion of the clean diffusive data. Figure 4.6e shows wave fields obtained by averaging one hundred sets of inverted data associated with stable values of α between 10^{-8} and 10^{-3} . Here the oscillations have been significantly reduced, but the noise does not allow the transformed field to follow the analytic solution closely at the wave front.

The IQT has now been performed via the discretized QT, thus avoiding the instabilities due to the integration limits of (4.25) and allowing for the inversion of numerical and experimental data. It should be noted, however, that when the SNR was reduced below 40 dB, the inversion quickly degraded and regularization was not nearly as effective at inverting the fields. Also, these inversions were done assuming that a perfect impulse function was used as a source, which of course is not realistic. Next, the use of sources other than exact impulse functions is discussed.

(a)



(b)

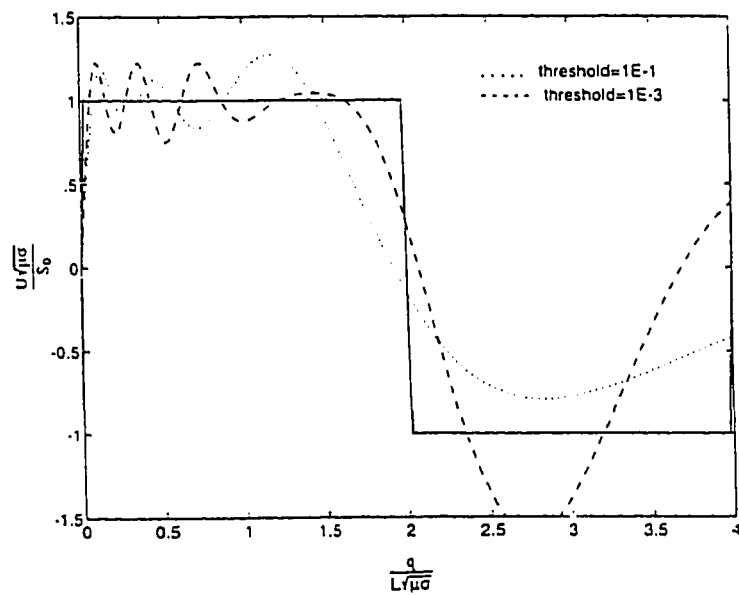
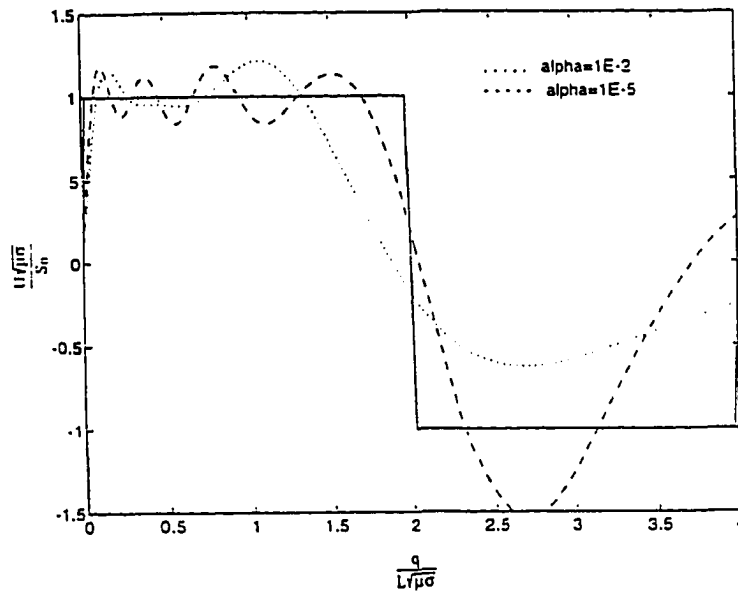


Figure 4.6 (a) Diffusion field with SNR = 40 dB (b) Transformed wave field with regularization obtained by eliminating singular values below a given threshold.

(c)



(d)

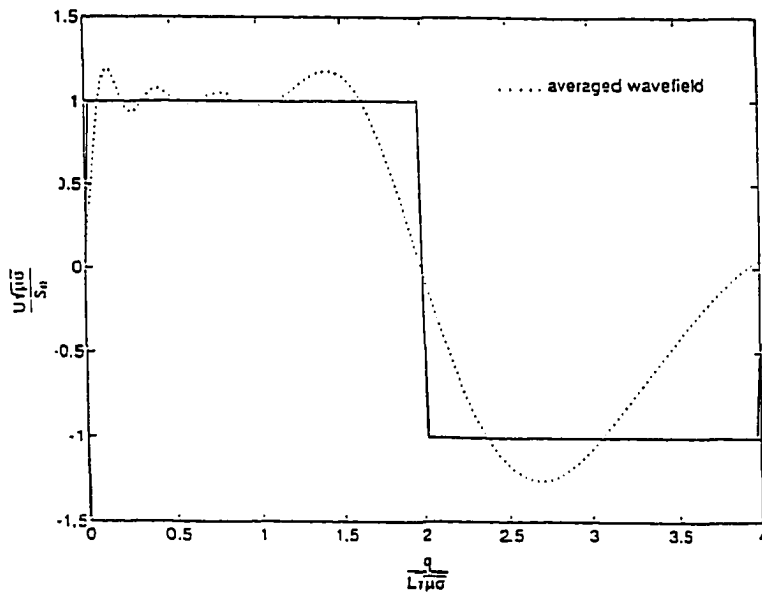


Figure 4.6 continued; (c) Transformed wave field obtained by averaging 100 stable fields regularized by eliminating singular values below a given threshold (d) Transformed wave field using Tikhonov regularization.

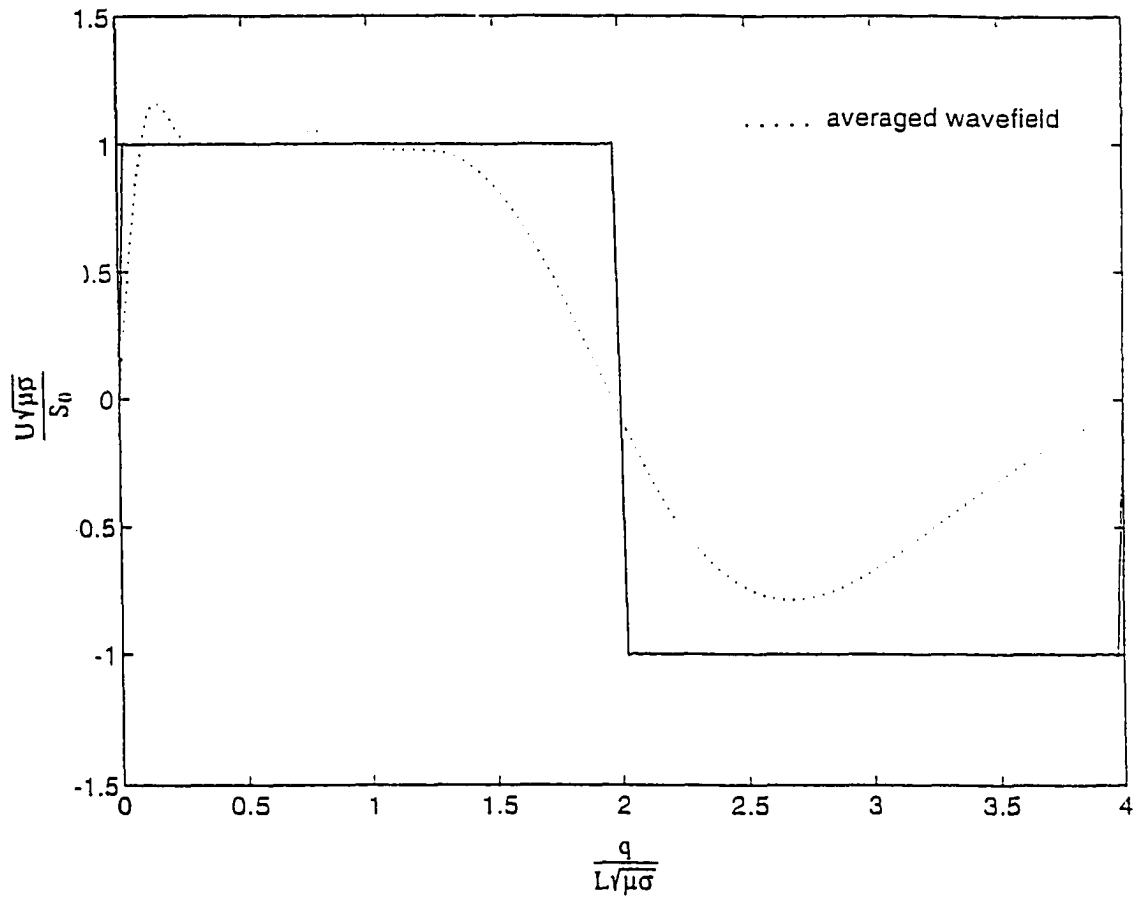


Figure 4.6 continued; (e) Transformed wave field obtained by averaging 100 stable fields inverted with Tikhonov regularization.

4.5 Transformation of non-impulsive sources

It has been shown that the IQT can be used to observe diffusive data in a wave domain, but the physical meaning of the transformed data is not always apparent. This is because the diffusive source does not in general transform to a wave source of the same form, and in many cases, transforms to an unstable source. As shown in (4.26) the IQT of the diffusive field with source S is a wave field with transformed source F . If the source is a Dirac delta function, the transformed source is also observed as a Dirac delta function. However, the IQT of a function which converges to a Dirac delta function in the limit does not itself converge to a Dirac delta function. This is shown by letting the diffusive source be an approximation to a Dirac delta function of the form

$$S(t) = S_0 \frac{e^{-t/\gamma}}{\gamma} \quad \gamma \ll 1, \quad (4.39)$$

for which the transformed wave source is

$$F(q) = S_0 \frac{1}{\sqrt{\gamma}} \sin\left(\frac{q}{\sqrt{\gamma}}\right). \quad (4.40)$$

The wave domain now has a different source than its diffusive counterpart and its physical meaning is unclear. Since the input is not an impulse, the measured response can not be interpreted as time-of-flight information. If (4.39) is used as a source to the diffusive problem B , the transformed wave field is given by

$$U(x, q) = \sum_{n \text{ odd}} \frac{4S_0}{\sqrt{\mu\sigma} n\pi} \left[\frac{\sin\left(\frac{n\pi}{2L\sqrt{\mu\sigma}} q\right) - \frac{n\pi}{2L\sqrt{\mu\sigma}} \sqrt{\gamma} \sin\left(\frac{q}{\sqrt{\gamma}}\right)}{\left(1 - \left(\frac{n\pi}{2L\sqrt{\mu\sigma}}\right)^2 \gamma\right)} \right] \cos\left(\frac{n\pi}{2L} x\right) \quad (4.50)$$

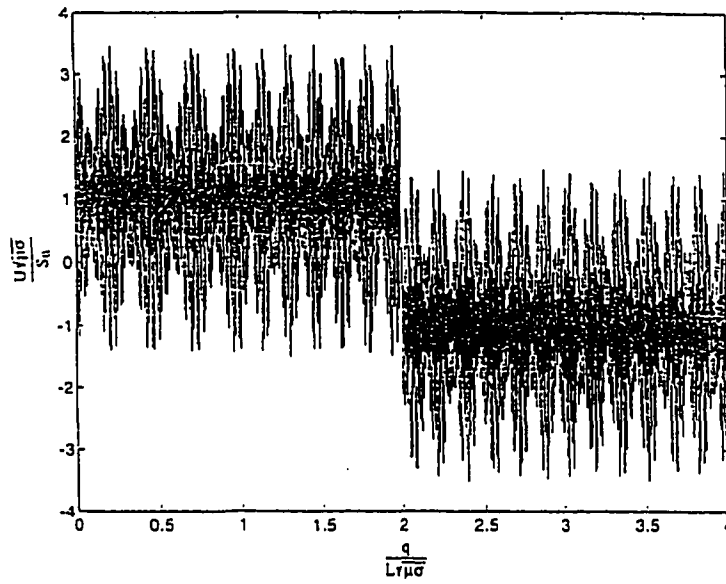
and is shown in Figure 4.7a with $\gamma = 10^{-6}$ seconds. The overwhelming noise is due to high frequency terms in the wave domain contributed by high rates of decay in the diffusive domain. Since a non-ideal impulse function was used as a source, the high rates of change in the diffusive field which are necessary for exact inversion are distorted. One method of addressing this instability might be to deconvolve the non-ideal impulse source into an exact impulse function and then perform the inversion, however, another method is presented here where the instabilities are reduced with the use of a low pass filter applied to the wave data. To demonstrate this (4.50) is passed through a fifth order Butterworth lowpass filter with cutoff frequency of 50 dimensionless units. The result is given in Figure 4.7b which shows that the filtered version of (4.50) is a stable wave field that closely resembles the field with a Dirac delta function as a source. This shows that although a non-ideal impulse function leads to an unstable source, these instabilities can be controlled by elimination of high frequency modes. Thus, it is possible to invert diffusive data with non-ideal impulse sources.

If the source of diffusion is time harmonic of the form $e^{j\omega t}$, the transformed source is given by

$$F(q) = \frac{1}{\sqrt{2\omega l}} \left[(1 + j) \sin\left(\sqrt{\frac{\omega}{2}} q\right) \cosh\left(\sqrt{\frac{\omega}{2}} q\right) + (1 - j) \cos\left(\sqrt{\frac{\omega}{2}} q\right) \sinh\left(\sqrt{\frac{\omega}{2}} q\right) \right] \quad (4.51)$$

which is an unstable source that leads to a wave field without physical meaning, as such, wave-based imaging based on this transform is not possible for the most common form of single frequency time-harmonic eddy current testing. This chapter focuses on the inversion of pulsed eddy current data because the IQT is not applicable to time-harmonic solutions of parabolic equations.

(a)



(b)

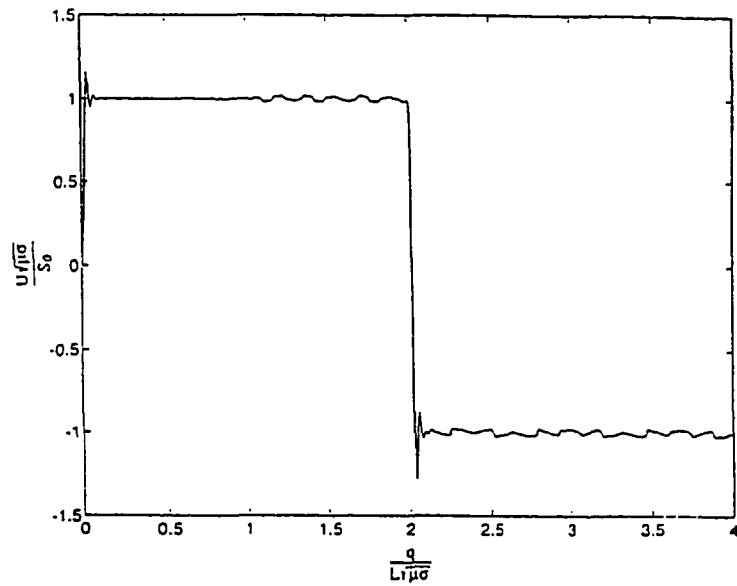


Figure 4.7 (a) Wave field obtained from inverting diffusion field with non-ideal impulse source (b) Low pass filtered version of (a)

4.6 Conclusions

The application of an algorithm for converting eddy current data to a pseudo wave has been considered in a simple test geometry. It is possible to observe such diffusive data in a wave domain and then use inversion schemes which rely on properties of wave propagation to solve the inverse problem. The IQT is a direct analytic inversion scheme which performs this transformation, however, it can be accomplished only with a closed form solution. Thus, the IQT is effective only in association with a calibration procedure involving basis functions that can be used to describe the diffusive data. The IQT does, however, provide a valuable tool with which to gain insight into the transformation process. The transformation can be implemented numerically by inverting the discretized QT. There are significant difficulties with the robustness of this inversion which can in part be overcome with regularization procedures. Two types of regularization are shown to be effective: elimination of small singular values below a given threshold; and Tikhonov regularization. These techniques provide robustness at the expense of high frequency information in the wave domain. A supplementary method of regularization which appears to be effective is the averaging of stable wave field values, however, the averaging can only be done with wave fields that have been regularized using one of the two schemes identified or any other effective scheme. Non-ideal impulse sources in the diffusion domain transform to wave domain sources which give rise to unstable wave fields. However, with the use of a low pass filter in the wave domain it is possible to stabilize the wave field by eliminating some of the high frequency wave modes. The methods described are not applicable to single frequency eddy current NDE, although application to swept frequency or pulsed eddy current NDE holds promise. Further research is required before the method can be applied to actual experimental eddy current data.

CHAPTER 5. A DIRECT INVERSION TECHNIQUE FOR MQS DATA

5.1 Introduction

Chapter 4 describes a transformation which allows diffusion fields to be observed as pseudo-wave fields and could provide a means for the direct inversion of time-domain MQS data. There are, however, several limitations which reduce the usefulness of the transformation. In particular the technique is not applicable to steady-state eddy current NDE. This chapter introduces a technique for the direct inversion/imaging of steady state eddy current data which does not rely on a transformation to waves. As mentioned in Chapter 2, there have been many attempts to provide a means for the direct inversion of eddy current data [95-97]. Generally, these approaches have incorrectly treated MQS eddy current fields as if they were actually propagating wave fields. The subsequent imaging algorithms then utilize "wave-based" inversion methods such as holography and tomography. Unlike these methods, the technique introduced in this chapter makes no attempt to back propagate MQS eddy current fields. Instead, the technique exploits phase shifts in the impedance of an eddy current coil. As with the transformation method of Chapter 4, there are many limitations to the method which currently limit its practical implementation.

As Chapter 2 points out, the complex impedance change ΔZ^s of a coil over a conducting halfspace with host conductivity σ_0 and containing an anomalous region with conductivity $\sigma(\mathbf{x})$ is given as [92]

$$\Delta Z^s = \frac{1}{I^2} \int_{v_D} (\sigma(\mathbf{x}) - \sigma_0) \mathbf{E}_0^s(\mathbf{x}) \cdot \mathbf{E}^s(\mathbf{x}) dv, \quad (5.1)$$

where $\mathbf{E}^s(\mathbf{x})$ is the electric field in the presence of an anomaly, $\mathbf{E}_0^s(\mathbf{x})$ is the electric field in the absence of the anomaly, and \mathbf{I}^s is the source current in the eddy current coil. In general, the impedance change ΔZ^s varies nonlinearly with variations in the conductivity of the unknown anomalous region $\sigma(\mathbf{x})$. This in turn makes the characterization of the anomalous region quite difficult in general. There have been techniques developed which utilize the nonlinear inversion of (5.1) [92-93], although they are quite limited due to the complex geometry of most eddy current tests. However, if the anomalous region is such that the electric field in the presence of the anomaly $\mathbf{E}^s(\mathbf{x})$ is well approximated by the electric field in the absence of the anomaly $\mathbf{E}_0^s(\mathbf{x})$, the inversion of ΔZ^s becomes much more straightforward. This fact has been utilized in [91,94] for the inversion of a layered conducting halfspace under a weak conductivity change. The goal of this chapter is to utilize a linearized inversion of (5.1) in the context of MQS diffusion phenomena. To do this, the requirements for the linearized inversion of (5.1) are pointed out and a technique is developed which can in theory be used to determine the position of a subsurface flaw. Unlike other attempts to invert MQS data, this technique does not incorrectly assume that the underlying MQS phenomenon is governed by wave propagation. As such, no attempt is made to back propagate MQS eddy current impedance measurements. 1-D analysis is used to demonstrate clearly this inversion technique without the complexities found in higher dimensional settings. Next, a finite element model is used to extend the results of the 1-D study to a 2-D setting. Finally, experimental results are utilized which demonstrate the limitations associated with extending this technique to realistic geometries.

5.2 1-D analysis

This section demonstrates how a direct inversion scheme can be utilized to invert MQS data and how this direct inversion method differs from those used for wave systems. To do this, a 1-D study is utilized for fully dynamic electromagnetic fields and MQS fields. The geometry for the 1-D analysis is shown in Figure 5.1. It consists of a slab of finite thickness L placed over a semi-infinite halfspace. The driving field is a sinusoidal current source in the y direction which sets up a constant magnetic field H_0^s at the boundary $x=0$ and is not a function of y and z . For fully dynamic systems the source can be thought of as a microwave horn which sets up a spatially uniform magnetic field on the surface in the region of interest. For MQS systems it can be thought of as a coil that is sufficiently large to set up a spatially uniform magnetic field on the surface in the region of interest. The governing equation for this time-harmonic system is

$$\frac{\partial^2 \mathbf{E}^s}{\partial x^2} + k^2 \mathbf{E}^s = 0 \quad (5.2)$$

where

$$k = \beta - j\alpha = \sqrt{\omega^2 \mu \epsilon - j\omega \mu \sigma} \quad (5.3)$$

As the operating frequency and material parameters are varied, k is associated with either hyperbolic, parabolic, or elliptic governing equations depending on whether the governing fields are fully dynamic, MQS, or static. The boundary conditions of the electromagnetic field are

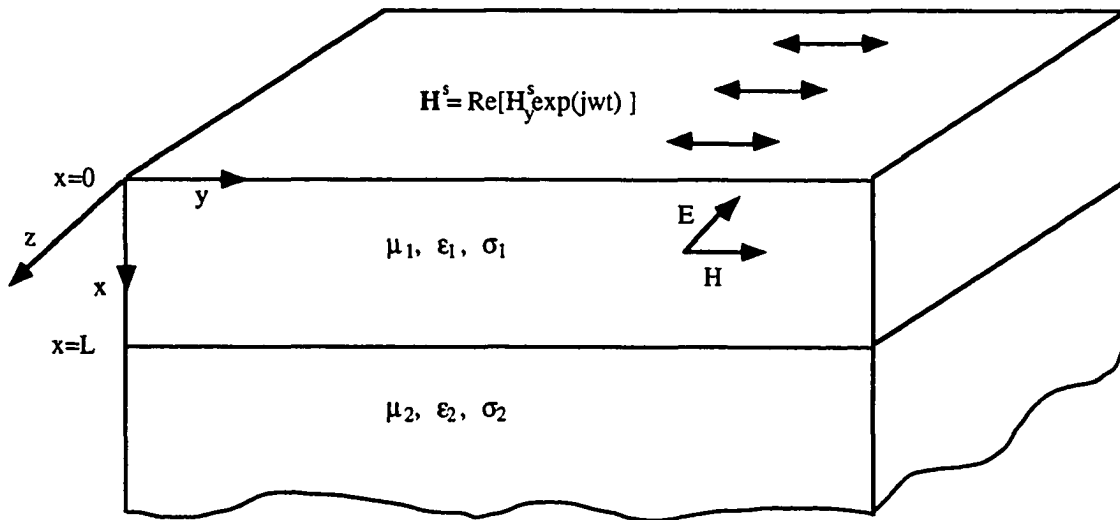


Figure 5.1 Geometry for the 1-D inverse problem.

$$\left. \frac{\partial E_1^s}{\partial x} \right|_{x=0} = j\omega\mu_0 H_0 \quad (5.4)$$

$$E_1^s \Big|_{x=L} = E_2^s \Big|_{x=L} \quad \frac{\partial E_1^s}{\partial x} \Big|_{x=L} = \frac{\partial E_2^s}{\partial x} \Big|_{x=L} \quad (5.5)$$

$$E_2^s \Big|_{x=\infty} = 0. \quad (5.6)$$

The solution of the system in region 1 is

$$E_1^s(x) = \frac{\omega\mu_0 H_0^s}{k_1} \left[\frac{\Gamma \exp(jk_1 L) \exp(-jk_1 x) + \exp(-jk_1 L) \exp(jk_1 x)}{\Gamma \exp(jk_1 L) - \exp(-jk_1 L)} \right] \quad (5.7)$$

where

$$\Gamma = \frac{1 + \frac{k_2}{k_1}}{1 - \frac{k_2}{k_1}} \quad (5.8)$$

Mathematically, (5.7) describes a combination of fields which change phase in the positive x and negative x directions. The solution is consistent for fully dynamic and MQS systems. The positive x field results from the boundary condition at $x = 0$ and the negative x field results from the interface at the boundary $x = L$. For fully dynamic systems, the solution represents forward and backward traveling waves whose existence is contingent on the presence of displacement current. These forward and backward wave components are separable and measurable. Under the MQS approximation wave propagation does not occur so the solution

represents the instantaneous interaction of the source field at $x = 0$ with the eddy currents which are perturbed by the interface $x = L$.

In this setting, the inverse problem for both fully dynamic and MQS systems is to determine the thickness of the slab (region 1) from measurements of the fields at $x = 0$. There is more than one mathematical relationship which yields this information, however, the field components necessary for its use must be physically present and measurable. A simple inversion technique which can be used for wave systems is obtained by utilizing the phase shift of the complex ratio of reflected and incident electric wave fields measured at $x = 0$. This ratio is

$$\frac{E^{s-}|_{x=0}}{E^{s+}|_{x=0}} = \frac{\exp(-j2k_1L)}{\Gamma} \quad (5.9)$$

whose complex phase shift is given by

$$\theta = -2\beta_1L. \quad (5.10)$$

This phase shift is linear provided regions 1 and 2 are occupied by linear homogeneous materials. A trivial inversion of (5.10) can be utilized to determine the thickness of the slab. A direct application of this relationship is seen in the measurement of thin film thickness with millimeter wave NDE [121] and this relationship is also used with synthetic aperture methods in higher dimensions to determine the position of scattering objects [24]. The implementation of this technique requires the measurement of incident and scattered fields which, of course, do not exist under the MQS approximation. Consequently, a different inversion method must be utilized for fields which exist under the MQS approximation.

In general, for MQS systems, e.g., eddy current NDE, an anomaly is detected by measuring the complex impedance of the source coil given as

$$Z^s = \frac{V^s}{I^s}. \quad (5.11)$$

The voltage and current of the source coil are not defined for this 1-D problem, so instead the measurement is of the intrinsic impedance of the fields at the boundary $x = 0$ which is given by

$$\eta^s|_{x=0} = \frac{E^s}{H^s}|_{x=0} = \frac{\omega\mu_0}{\sigma} \left[\frac{\Gamma \exp(j2k_1L) + 1}{\Gamma \exp(j2k_1L) - 1} \right]. \quad (5.12)$$

To force the phase to wrap around the origin a differential impedance measurement is made as

$$\Delta\eta^s = \eta^s - \eta^s_{L=\infty}. \quad (5.13)$$

which is analogous to the nulling of an eddy current probe. To simulate an eddy current test, region 1 is given the properties of stainless steel with $\epsilon = \epsilon_0$, $\mu = \mu_0$, and $\sigma = 1.4 \times 10^6$; the source frequency is $f = 2$ MHz. The ratio of displacement current to conduction current in region 1 is

$$\frac{\omega\epsilon}{\sigma} = 12.4 \times 10^{-12} \quad (5.14)$$

so displacement current is negligible and the MQS approximation is valid.

The following results show the phase shift of $\Delta\eta^s$ at $x = 0$ with the stainless steel slab placed over three different halfspace media. The exact phase shift is shown in the dotted line and a linear reference plot with slope $-2L/\delta$ is shown in the solid line, where

$$\delta = \sqrt{\pi f \mu \sigma} = \frac{1}{\alpha} = \frac{1}{\beta} \quad (5.15)$$

is referred to as the “skin depth” of the eddy currents. With the material properties of stainless steel and a source frequency $f = 2$ MHz, the skin depth in region 1 is $\delta = 0.30$ mm. Figure 5.2a shows the phase shift of $\Delta\eta^s$ with region 2 consisting of a perfectly conducting halfspace. Note that a distinct nonlinearity exists for values of L less than one skin depth. Below this depth the phase shift follows the linear plot quite well. In Figure 5.2a this nonlinearity is a maximum at approximately one half skin depth. If the thickness of the slab at $L = 0.15$ mm is determined using the linear relationship $\theta = -2L/\delta$, the predicted value for the thickness is $L = 0.11$ mm, an error of 25%. This demonstrates the significance of the errors which arise due to the approximations made in the inversion and makes it clear that the use of a simple inversion scheme based on a linearization is not always justified.

Figure 5.2b shows the phase shift measured with region 2 having the properties of free space ($\epsilon = \epsilon_0$, $\mu = \mu_0$, and $\sigma = 0$). The result is similar to Figure 5.2a except the nonlinearity takes a somewhat different form. Once again, the phase shift becomes linear after approximately one skin depth. Thus, the phase shift becomes linear when the effect of the boundary is reduced due to the attenuation of the eddy currents with depth. To demonstrate this further, the conductivity of region 2 is varied only 10% from that of region 1 with the result shown in Figure 5.2c. Figure 5.2c shows that the phase shift is now linear for all depths L . In all results, this linear relationship is seen when the depth of the interface is near a skin depth, or when the contrast of the anomaly from the host medium is small. In both instances, the total field in the sample is well approximated by the source field, i.e., the field in the absence of an interface at $x = L$. In this case, linearity follows from (5.1) because the total field of (5.7) is well approximated by

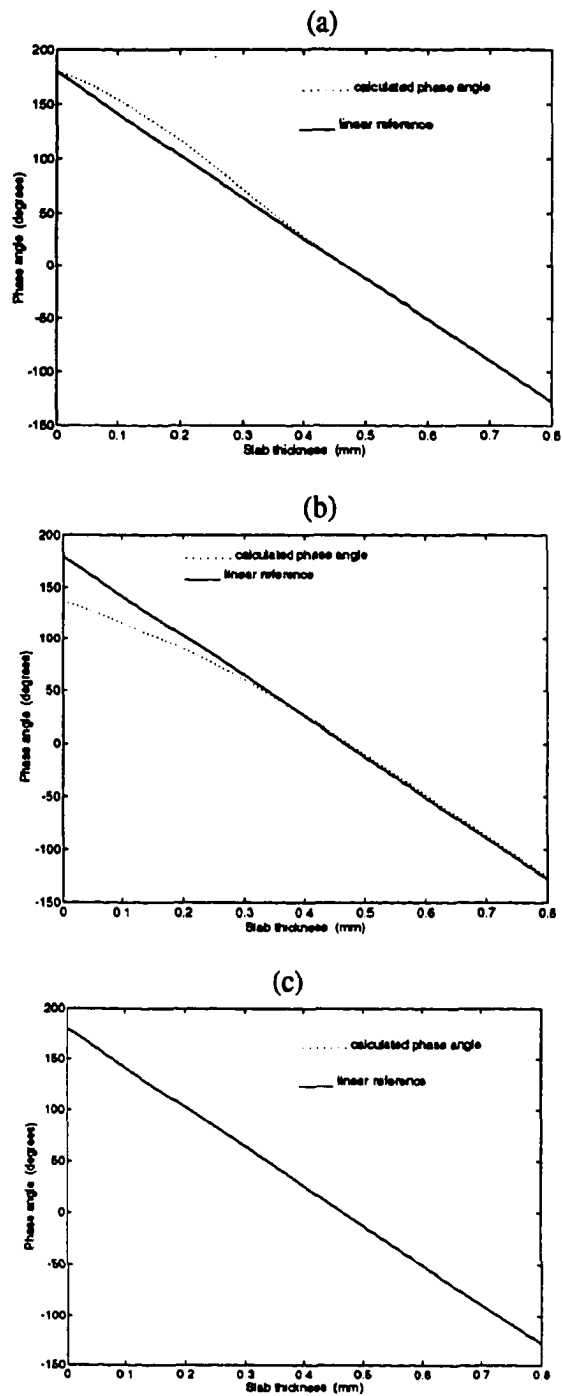


Figure 5.2 Phase shifts of intrinsic impedance ($f=2$ MHz, Slab 1: $\sigma = 1.4 \times 10^6$, $\mu = \mu_0$, $\epsilon = \epsilon_0$) (a) Slab 2: $\sigma = \infty$, $\mu = \mu_0$, $\epsilon = \epsilon_0$ (b) Slab 2: $\sigma = 0$, $\mu = \mu_0$, $\epsilon = \epsilon_0$ (c) Slab 2 $\sigma = 1.54 \times 10^6$, $\mu = \mu_0$, $\epsilon = \epsilon_0$.

$$E_0^s(x) = \frac{\omega\mu H_0^s}{\sigma} \exp(-jk_1x), \quad (5.16)$$

which is the solution to (5.2)-(5.6) with a decay condition at $x = \infty$ instead of a boundary condition at $x = L$. Substituting (5.16) for both the total electric field $E^s(x)$ and the source electric field $E_0^s(x)$ into (5.1) leads to an impedance phase shift relationship of

$$\theta = -2L/\delta \quad (5.17)$$

which is precisely the value observed in the 1-D analysis. This linear relationship is analogous to the linear relationship (5.10) obtained for fully dynamic wave fields and can be used analogously to determine directly the thickness of the slab. This is an important result because it demonstrates that there are linearized relationships which exist and can be used to determine the distance from a source to a current perturbing flaw for MQS systems. In the next section, a finite element model is utilized to extend this linearized inversion to a two-dimensional setting.

5.3 2-D finite element study

5.3.1 Introduction

The results of Section 5.2 demonstrate that, under a weak flaw approximation, the phase of eddy current impedance measurements yields a linear relationship between the source coil and the depth of a defect. The 1-D analysis neglects factors such as finite size coil effects which could distort the linear impedance phase shift used in the inversion. It also neglects the fact that resolution is quite limited because, as this section demonstrates, the phase repetition period of the eddy currents is very large compared to the size of the flaws. A 2-D finite

element model [122] is now used to investigate the findings of Section 5.2 in a more realistic setting with the aforementioned effects included. The finite element test geometry is shown in Figure 5.3. It consists of a current rail with operating frequency 2MHz which is infinite in the z direction and is placed over a stainless steel slab containing a small void. The impedance of the current rail is calculated at 81 positions above the sample along a baseline that is 1.6 mm long. As in the 1-D study, the phase shift is forced to wrap around the origin by taking a differential impedance measurement as

$$\Delta Z^s = Z_{\text{defect}}^s - Z_{\text{no defect}}^s \quad (5.18)$$

To ensure that the linear phase relationships necessary for the inversion algorithm are available, the impedance formula (5.1) must be investigated for the geometry of Figure 5.3. Since (5.1) involves an integration over the anomalous region it is necessary to know how the fields are affected by the anomaly over that volume. The finite element model is used to calculate the total electric field $E^s(\mathbf{x})$ at the position of a small void (0.02 mm x 0.02 mm) one skin depth deep (0.30 mm) and the electric field $E_0^s(\mathbf{x})$ which exists at that position in the absence of the flaw. At the position of the void, the difference between $E^s(\mathbf{x})$ and $E_0^s(\mathbf{x})$ is less than 1 percent of the electric field in the absence of the flaw $E_0^s(\mathbf{x})$, so (5.1) can be well approximated by

$$\Delta Z^s = \frac{1}{I^2} \int_{V_D} (\sigma(\mathbf{x}) - \sigma_0) E_0^s(\mathbf{x}) \cdot E_0^s(\mathbf{x}) dv. \quad (5.19)$$

For a uniform source, the eddy currents induced in the test sample can be written as

$$E_0^s(\mathbf{x}) = E_0^s|_{x=0} \exp\left(-\frac{x}{\delta}(1+j)\right). \quad (5.20)$$

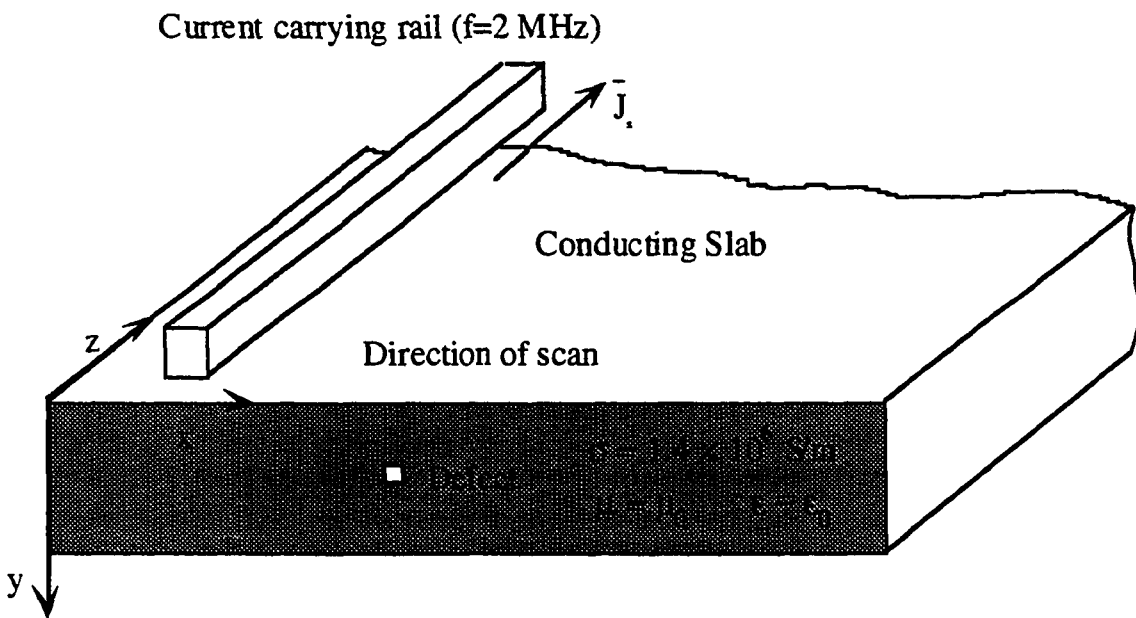


Figure 5.3 Eddy current finite element geometry.

Inserting (5.20) into (5.19) leads to an impedance phase shift θ vs. distance d (source coil to flaw) of

$$\theta = -\frac{2d}{\delta} + \phi_0, \quad (5.21)$$

where ϕ_0 represents a constant offset due to lift off of the coil. A similar linear relationship is arrived at in [98], however, in [98] this relationship is used as justification for implementing a holographic inversion scheme based on the backpropagation of the eddy current fields. As mentioned previously, this is a misinterpretation of the underlying physics governing MQS phenomena. "Wave-based" inversion schemes such as holography do not have a physical basis for eddy current fields which do not support wave propagation. The inversion technique developed here differs in that no attempt is made to back propagate the eddy current diffusion fields. Instead, the linear relationship of (5.21) is utilized to determine the position of a subsurface flaw directly. This technique requires *a priori* knowledge that the flaw provides a weak current perturbation leading to a linearized inversion of ΔZ^s .

To utilize this technique, a series of impedance measurements are taken along a baseline above the stainless steel sample. To generate an image, the stainless steel sample region is divided into an image array consisting of a number of pixels. The algorithm then assigns an appropriate intensity to each pixel value m,n according to

$$I(m,n) = \left| \sum_{k=1}^K F(k)G(m,n,k) \right| \quad (5.22)$$

where

$$F(k) = |Z^s(k)| \exp(j\theta_{Z^s(k)}) \quad (5.23)$$

is the complex impedance of the source coil at the k_{th} baseline position, and

$$G(m,n,k) = \exp\left\{j\frac{2}{\delta}[(x(m,n) - x(k))^2 + y(m,n)^2]^{1/2}\right\} \quad (5.24)$$

corresponds to the impedance phase (plus or minus a constant offset) which would occur if the void were located at the m_{th} , n_{th} pixel for the k_{th} source position. Equation (5.22) acts as a matched filter which passes only the impedance values which correspond to the depth of the flaw. Any constant offset in the measured phase shift is averaged out during the process. This procedure provides a simple and direct mathematical technique which can be used to obtain quantitative information about subsurface flaws. This type of algorithm is often applied to wave fields in the form of synthetic aperture radar (SAR) [24], however, the measured phase shift need not arise from the propagation of wave fields. The only requirement is that the measured quantity contain linear phase shifts as the distance d from the source to a defect is varied.

5.3.2 Results

Figure 5.4 shows an image with the void located in the center of the sample at the position (0.80 mm, -0.30 mm) so that the depth corresponds to one skin depth. The figure shows the intensity at each pixel with the maximum values shaded dark. The predicted maximum using the algorithm of Section 5.3.1 is at (0.73, -0.99); well off the actual position of the flaw. This large error occurs because the inversion algorithm utilizes the fact that the impedance of the current rail has phase shifts proportional to $-2d/\delta$ in all directions from the current rail. For this to occur, the induced eddy currents in the sample must have equiphase

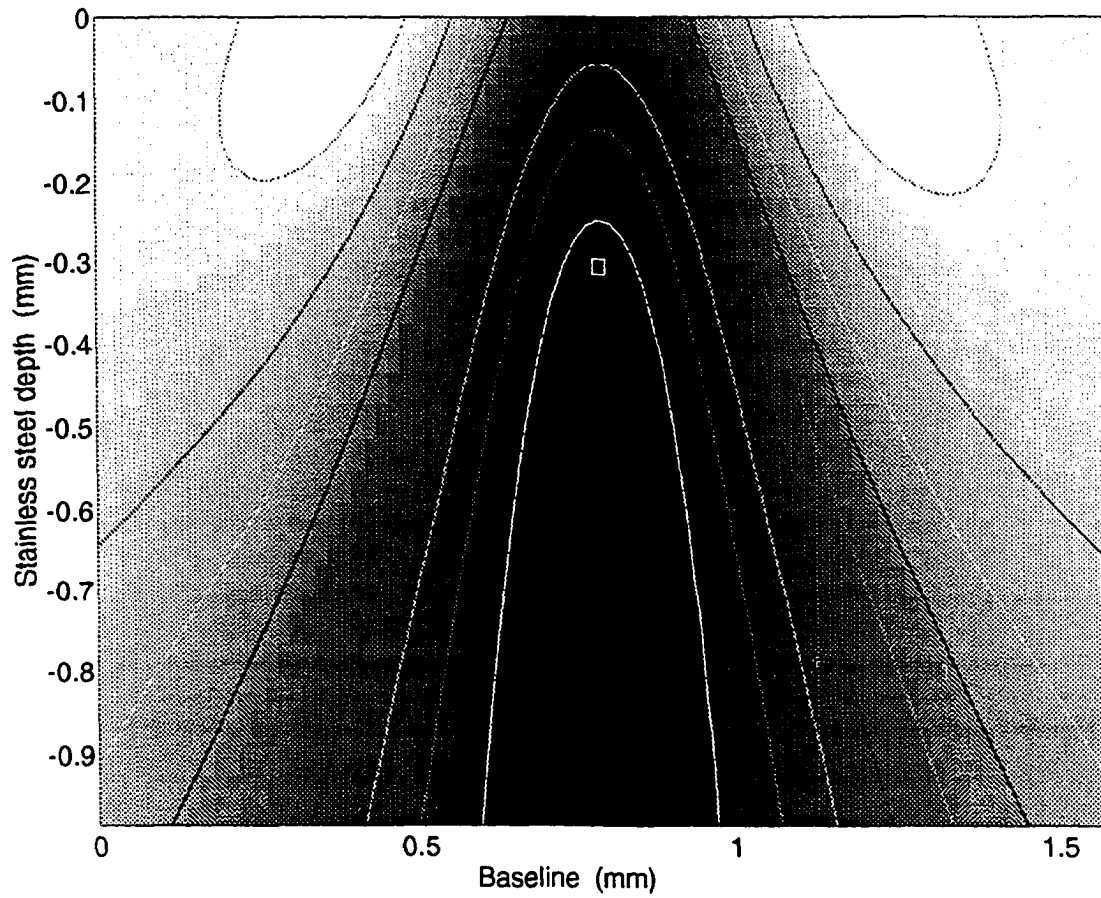


Figure 5.4 Image with current rail over stainless steel slab: void position (0.80,-0.30), predicted defect position (0.73,-0.99)

contours on semi-circular lines around the current rail. The actual equiphase contours are shown in Figure 5.5a and are seen to be distorted due to the air-metal interface altering the field lines. For demonstration purposes, the distortion in the phase contours is eliminated by removing the air-stainless steel interface and replacing the air region above the sample entirely with stainless steel. The current rail is now embedded in the test sample and the equiphase contours are circular as shown in Figure 5.5b. The inversion algorithm is now applied to impedance data taken at 81 positions along the same baseline used previously. The resulting image is shown in Figure 5.6 with the predicted defect position at (0.78 mm, -0.34 mm). This is much closer to the actual defect position, but there is still an error that can be attributed to the averaging of the electric field which is done during the impedance calculations. The impedance is defined as

$$Z^s = \frac{V^s}{I^s} \quad (5.24)$$

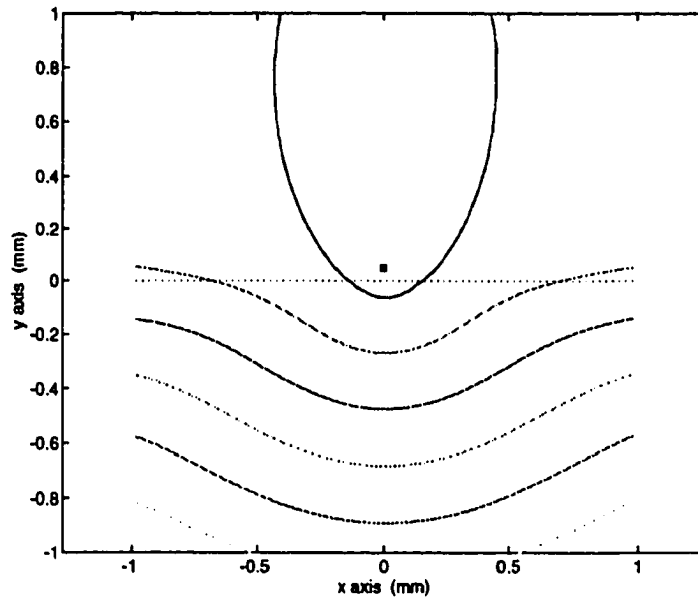
where

$$V^s = \int \mathbf{E}^s \cdot d\mathbf{l}. \quad (5.25)$$

Physically, this corresponds to the integrated effects of the many turns of a coil. This averaging of the electric field tends to smear the resultant image because each element in the rail views the flaw as being at a slightly different location. To eliminate this problem, the current rail is reduced from 72 elements (6 x 12) to 2 elements (1 x 2). The resultant image is shown in Figure 5.7 and accurately predicts the position of the defect at (0.80, -0.30).

The flaw is now moved to one third of its previous depth (0.80, -0.10) to cause a greater current perturbation. The resultant image is shown in Figure 5.8 with the predicted defect

(a)



(b)

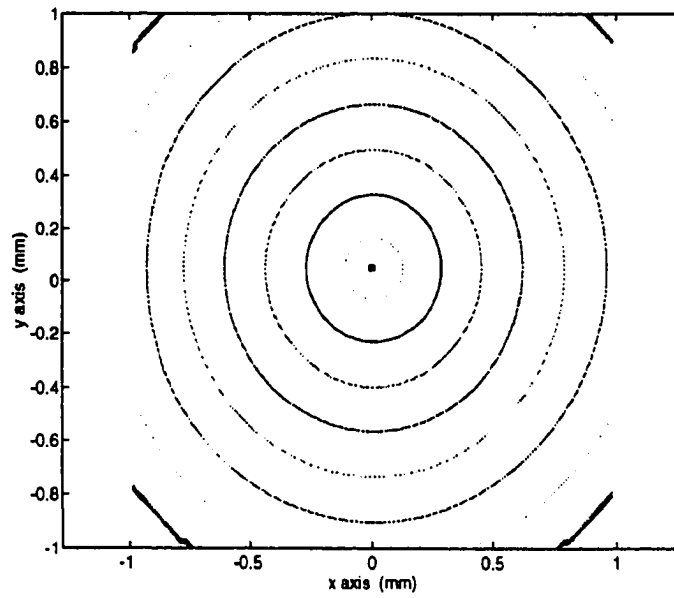


Figure 5.5 Eddy current equiphase contours (a) Current rail over a stainless steel halfspace (b) Current rail embedded in a stainless steel fullspace.

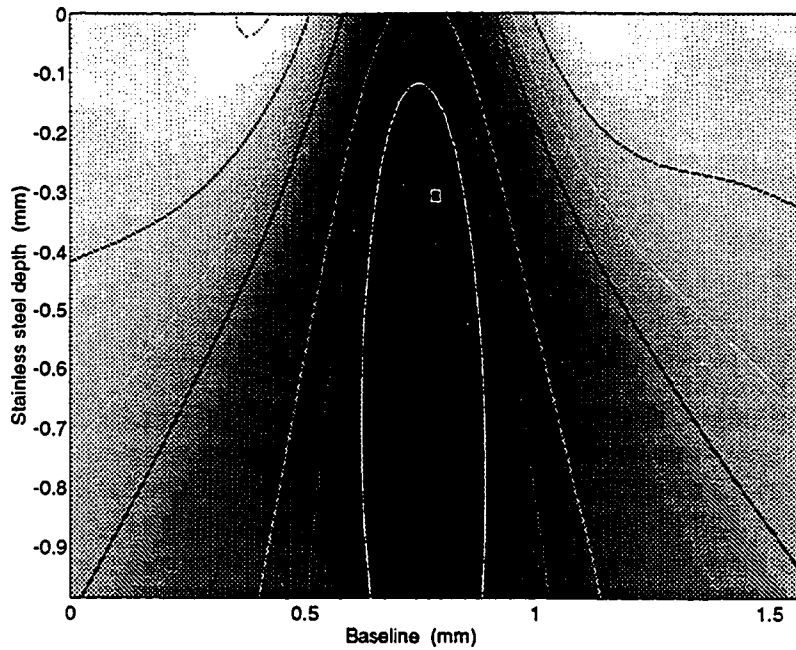


Figure 5.6 Image with current rail embedded in stainless steel: defect position $(0.80, -0.30)$, predicted defect position $(0.78, -0.34)$.

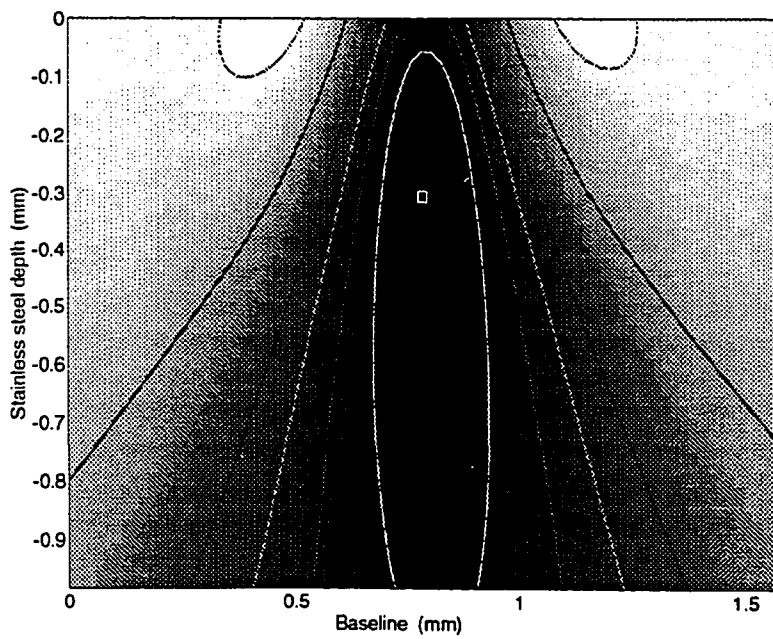


Figure 5.7 Image with current rail consisting of 2 elements: defect position $(0.80, -0.30)$, predicted defect position $(0.80, -0.30)$.

position now at (0.78, -0.08). The introduced error can be attributed to the increased effect of the flaw which distorts the linear approximation assumed in the impedance formula of (5.1). To demonstrate this effect, the impedance of the current rail is calculated with the void positioned at varying depths directly beneath the rail. The resulting impedance phase shift (dotted line) is shown along with a linear reference plot (solid line) in Figure 5.9. The result is very similar to the 1-D results of Figure 5.2 with the nonlinearity clearly visible for small depths. Thus, the proper inversion scheme for data associated with even small flaws may be nonlinear.

5.3.3 Resolution

All of the images shown have had very poor spatial resolution which makes interpreting the actual position of the flaw quite difficult, particularly with experimental data. The lack of resolution is directly related to the large phase repetition length of the eddy currents in the sample. The phase of the sinusoidal eddy currents repeats every $2\pi\delta$, while the defects which are inspected are generally less than one skin depth deep. Therefore, the relative change in phase which is observed when the defect is viewed at different positions is not large enough to create a high resolution image of the void. This is an inherent problem in eddy current imaging and is analogous to an attempt to resolve millimeter size defects with centimeter long waves. For wave based tests, the source frequency can be increased to improve the resolution, however, for the eddy current tests increasing the source frequency is generally not an option as it leads to a reduction in skin depth. To compensate for this difficulty, some researchers in this area use a signal processing technique known as "phase multiplication" [97-99]. The measured impedance phase is multiplied by a constant p and (5.23) is then rewritten as

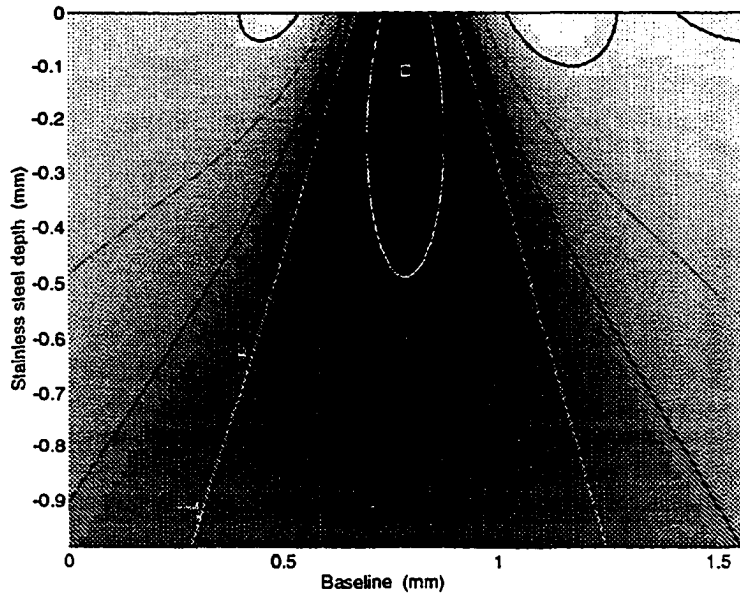


Figure 5.8 Image with defect closer to surface: defect position (0.80, -0.10) , predicted defect position (0.78, -0.08)

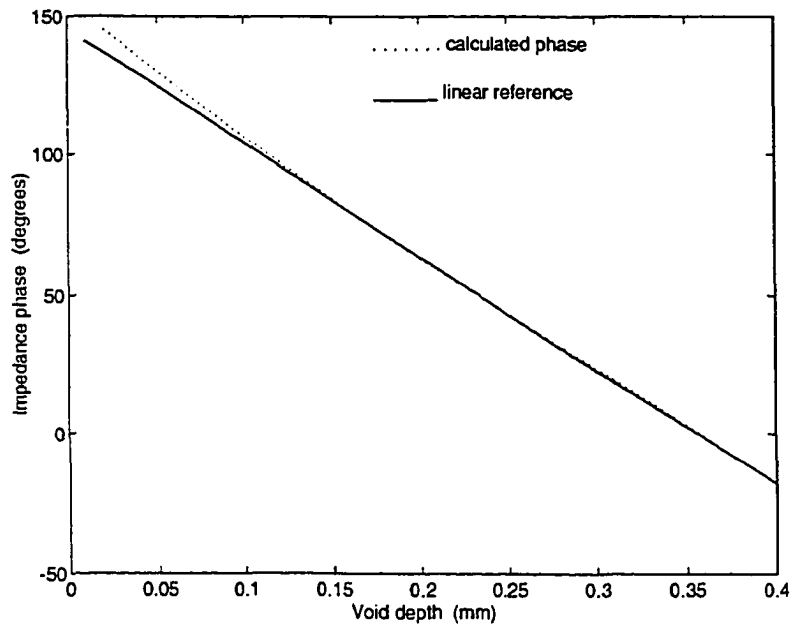


Figure 5.9 Impedance phase shift vs. void depth.

$$F(k) = |Z^s(k)| \exp(-j p \theta_{Z^s(k)}) \quad (5.26)$$

while (5.24) is written as

$$G(m,n,k) = \exp\left\{j p \frac{2}{\delta} [(x(m,n) - x(k))^2 + y(m,n)^2]^{1/2}\right\}. \quad (5.27)$$

This has the effect of reducing the phase repetition length and results in improved resolution, however, it also reduces dynamic range if there are multiple flaws which produce different signal strengths. Without the use of this technique the phase repetition period is too large for any reasonable degree of resolution to be obtained. Phase multiplication has no physical basis and does not appear to be an adequate solution to the lack of resolution, however, for explanatory purposes it is utilized in the following results.

5.3.4 Modification for phase distortion effects

For demonstration purposes the distortion of eddy current equiphase contours was eliminated by removing the metal-air interface, but this is obviously not a realistic solution to the problem. To overcome this obstacle operationally, an approach is presented which modifies the inversion algorithm in order compensate for the actual equiphase contours which the source coil and the test sample produce. The approach utilizes the fact that although the induced eddy currents are distorted at the air-metal interface, there is still a linear phase shift associated with the eddy currents. The interface simply distorts the direction of this linear phase shift (from circular). The original inversion algorithm utilizes the fact that a defect at any position on a circular equiphase contour will result in an identical phase shift in the detection coil. The distortion of the interface of course alters this assumption. The algorithm is now

modified so that defects on a distorted equiphase contour are assumed to result in identical impedance phase shifts. From (5.19)-(5.21) it is known that the phase shift of ΔZ^s for a void at position (x_0, z_0) is proportional to twice the phase shift of the induced eddy currents at the position (x_0, z_0) in an unflawed sample. To exploit this fact, the eddy current coil and the test geometry of an unflawed sample are modeled numerically. From this model, the eddy current phase information is obtained at uniform pixel locations in the test geometry. The inversion algorithm is now modified with (5.27) given as

$$G(m,n,k) = \exp(j2p\psi(m,n)). \quad (5.28)$$

$\psi_{m,n}$ corresponds to the phase of the eddy currents at the m_{th} , n_{th} pixel and p corresponds to the phase multiplication used to improve image resolution. With this modification, the inversion algorithm no longer requires spherical equiphase contours to utilize the impedance phase shift vs. defect depth relationship. The coil is simply modeled over an unflawed sample and the phase of the eddy currents calculated at pixel locations in the sample. The finite element model is used to compensate for the distortion of the induced eddy current phase shifts in the conducting sample. The effects of liftoff can be eliminated provided the modeled coil has the same liftoff as the experimental coil. Obviously, it is still important that the phase shift ΔZ^s of the coil be related to the phase shift of the induced eddy currents. To demonstrate this, the current rail is placed over the conducting halfspace with a liftoff of 0.04 mm and ΔZ^s is calculated with a void at varying depths directly below the current rail. In Figure 5.10 the solid line shows twice the phase shift of the eddy currents beneath the current rail in the absence of a flaw, the dotted line shows the phase shift of ΔZ^s as the depth of the void is varied in the sample. The figure shows that the phase shift of ΔZ^s is very similar to that of the eddy current phase with a nonlinearity for small depths. (Note: an offset was added to the eddy current phase shift for clarity, however, it would have no effect on the imaging algorithm.) Thus, the

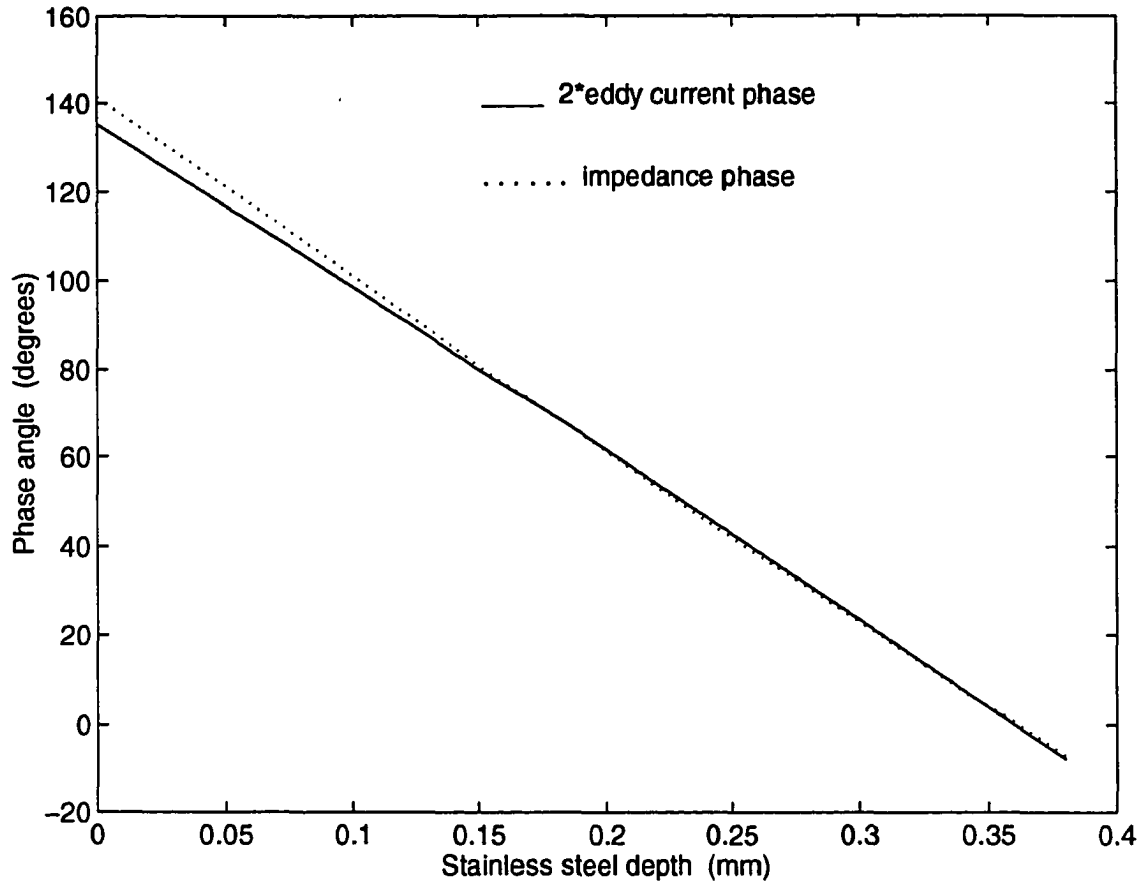


Figure 5.10 Comparison of phase shift of ΔZ^s vs. defect depth (solid line) and the eddy current phase (times two) vs. sample depth (dotted line).

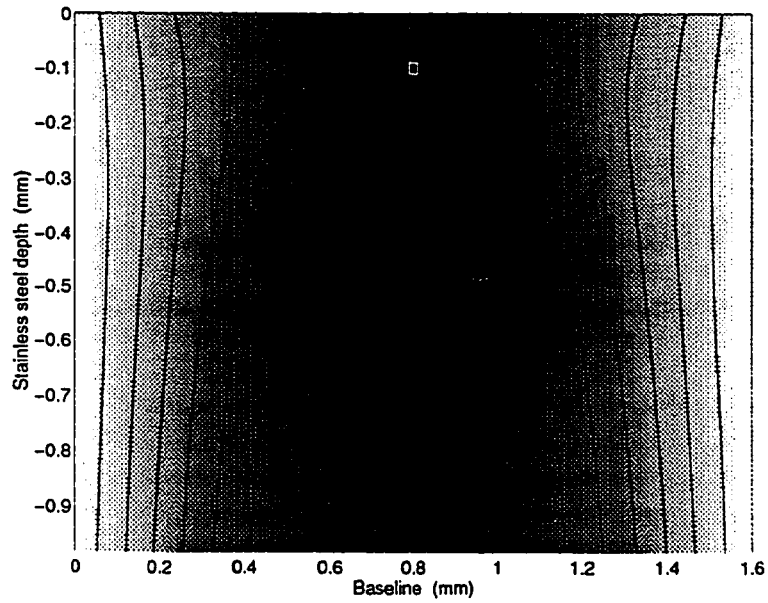
modified algorithm simply utilizes the phase shift of the eddy currents at each position in an unflawed sample and the impedance change of the coil measured along a baseline to predict the position of a void. To test the modified algorithm, impedance data were obtained using the original geometry of Figure 5.3 (coil over a stainless steel slab). The void was placed at two different positions (0.80,-0.10) and (0.80,-0.30) with the resulting images shown in Figure 5.11. Figure 5.11a shows the image with the void at (0.80,-0.10) and Figure 5.11b shows the image with the void at (0.80,-0.30). The predicted maxima occur at (0.78,-0.08) and (0.80,-0.30) for the respective voids. The error in the predicted maximum of the shallow void can be attributed to the nonlinearity of the impedance phase at small defect depths. Although the inversion algorithm reliably predicts the void position, the resolution of the images is clearly insufficient to determine the position of the flaw. To increase the resolution, a phase multiplication with $p = 12$ is used with the results shown in Figure 5.11c and 5.11d. The figure shows that the resolution is improved significantly and the depth of the flaw can be predicted reliably from the images. However, phase multiplication reduces dynamic range and can result in errors when noise is present in the measured data. This reduced dynamic range also limits the algorithms ability to detect multiple flaws.

5.3.5 Noise effects

Random noise was added to the finite element data to determine how this method could be utilized for noisy experimental data. The impedance data calculated with the void at (0.80,-0.30) was corrupted with a signal to noise ratio (SNR) of 20 dB, with

$$\text{SNR} = 10 \log \frac{\sigma_s^2}{\sigma_n^2}, \quad (5.29)$$

(a)



(b)

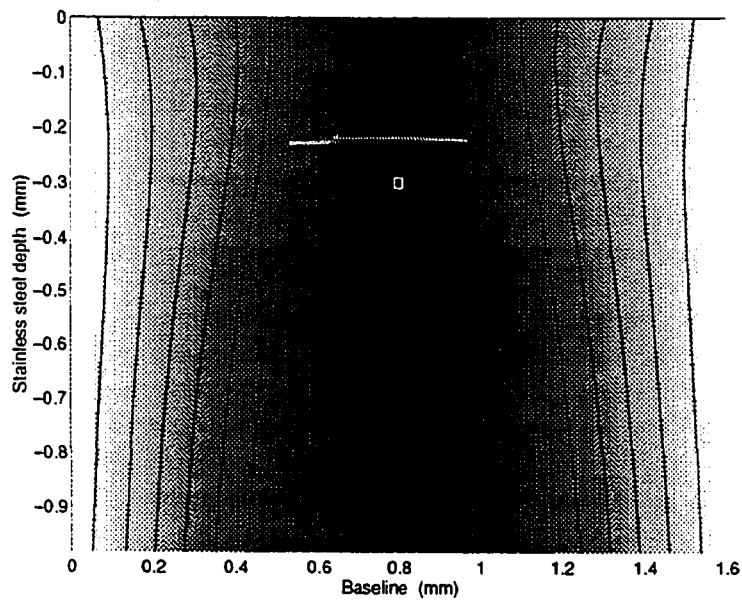


Figure 5.11 Images with coil in air over stainless steel sample: (a) defect position (0.80,-0.10), no phase multiplication (b) defect position (0.80,-0.30), no phase multiplication

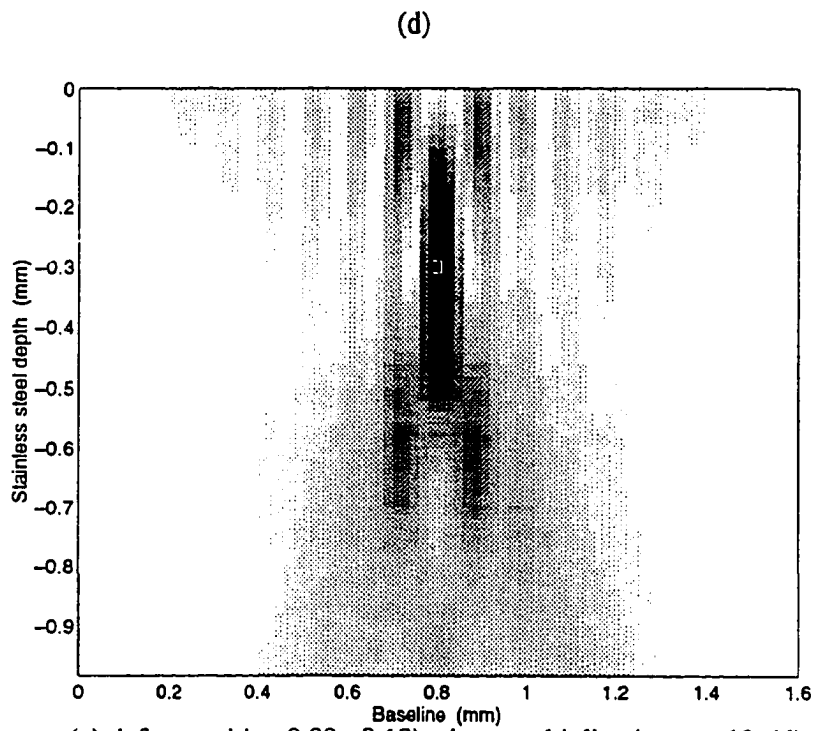
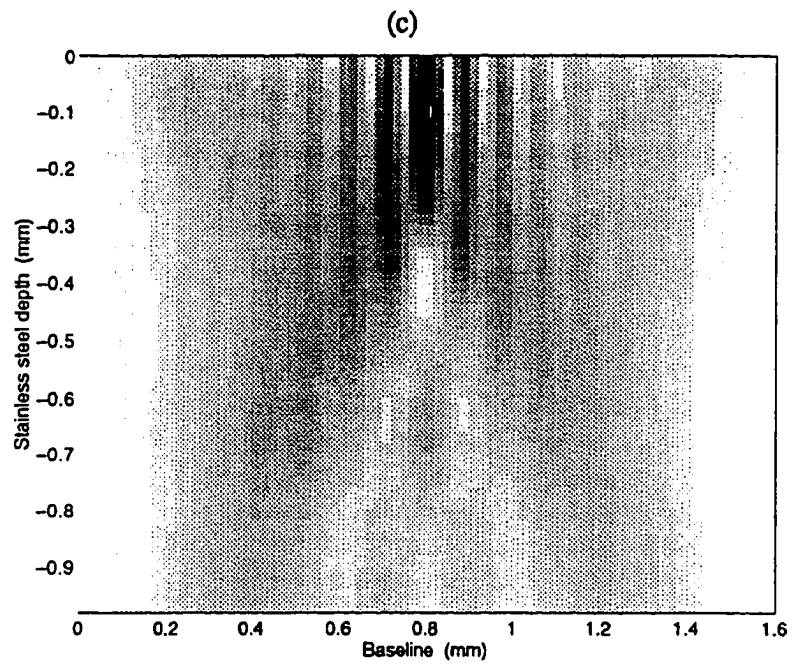


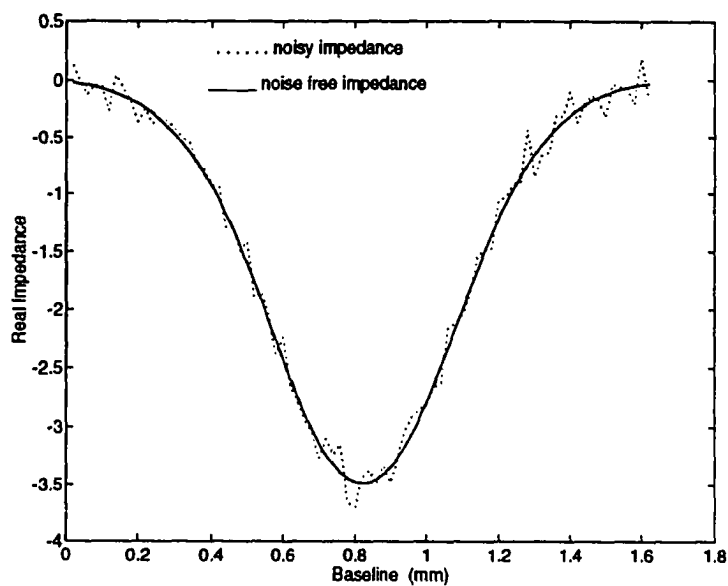
Figure 5.11. cont. (c) defect position 0.80,-0.10, phase multiplication $p = 12$ (d) defect position (0.80,-0.30), phase multiplication $p = 12$

where σ_s^2 is the variance of the signal and σ_n^2 is the variance of the noise. Figure 5.12a and Figure 5.12b show the original impedance data along with the corrupted data. The resultant image using the corrupted data is shown in Figure 5.13a with $p = 12$ and the predicted defect position at (0.80,-0.30). Figure 5.13b is an image generated with the corrupted data and $p = 40$. The predicted defect position is at (0.80,-0.38), however, the resultant image contains many artifacts which indicate that phase multiplication is quite sensitive to noise in the data. Thus, the phase multiplication constant p must be chosen with a careful consideration of the signal to noise ratio of the measured data.

5.3.6 Coil effects

As demonstrated previously, the electric field of the wires in the source coil is averaged when the impedance is measured. This effect produces errors which lead to distortion of the image. To investigate this effect in the modified algorithm, the current rail was made to consist of 576 elements (24 x 24) and impedance data were taken on a baseline over the stainless steel sample with the defect at (0.80,-0.30). The predicted defect position is found to be at (0.80, -0.30). The process was repeated with the defect at (0.80,-0.10) and the predicted defect position is at (0.80,-0.10). The effects due to averaging appear to be reduced in the modified imaging algorithm, however, they potentially could be much more noticeable in a 3-D coil where the fields are not only averaged in the r and z components, but also in the ϕ direction around the circumference of the coil. Section 5.4 discusses this effect for axisymmetric coils and potential future work which could address this issue. Figure 5.14 shows the phase shift of ΔZ^s as the depth of the void is varied beneath the larger coil. The phase shift of ΔZ^s is shown in the dotted line, while the phase shift of the induced eddy current in the absence of a void directly beneath the current rail is shown in the solid line. Unlike the previous results of Figure

(a)



(b)

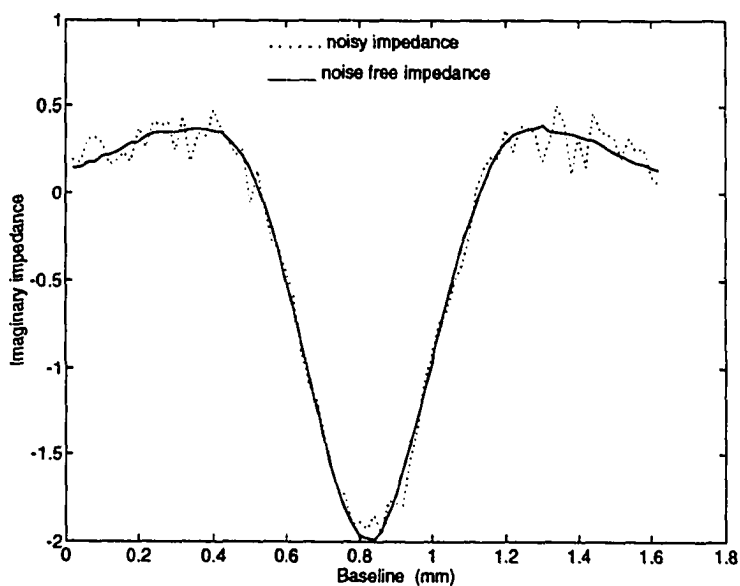
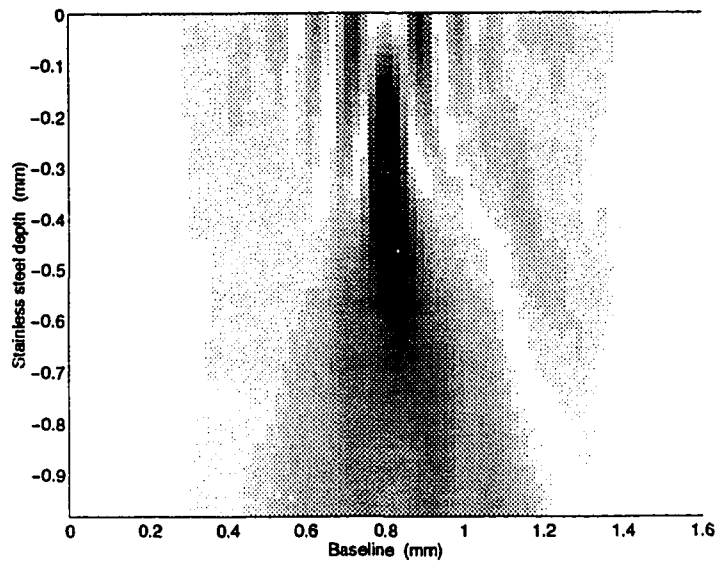


Figure 5.12 Impedance data with SNR = 20 dB. (a) Real part (b) Imaginary part.

(a)



(b)

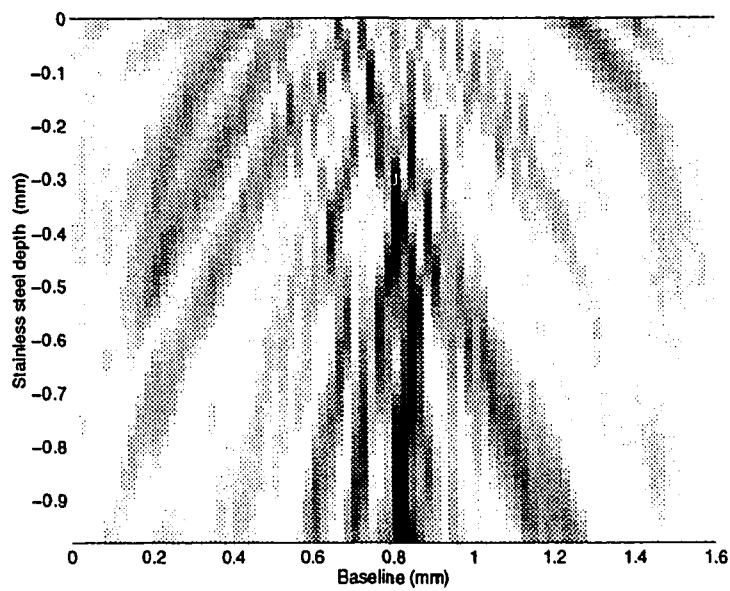


Figure 5.13 Images using modified algorithm with coil in air over stainless steel sample with SNR = 20 dB: defect position (0.80, -0.30) (a) phase multiplication $p=12$: predicted defect position (0.80, -0.30) (b) modified algorithm with phase multiplication $p=40$: predicted defect position (0.80, -0.38).

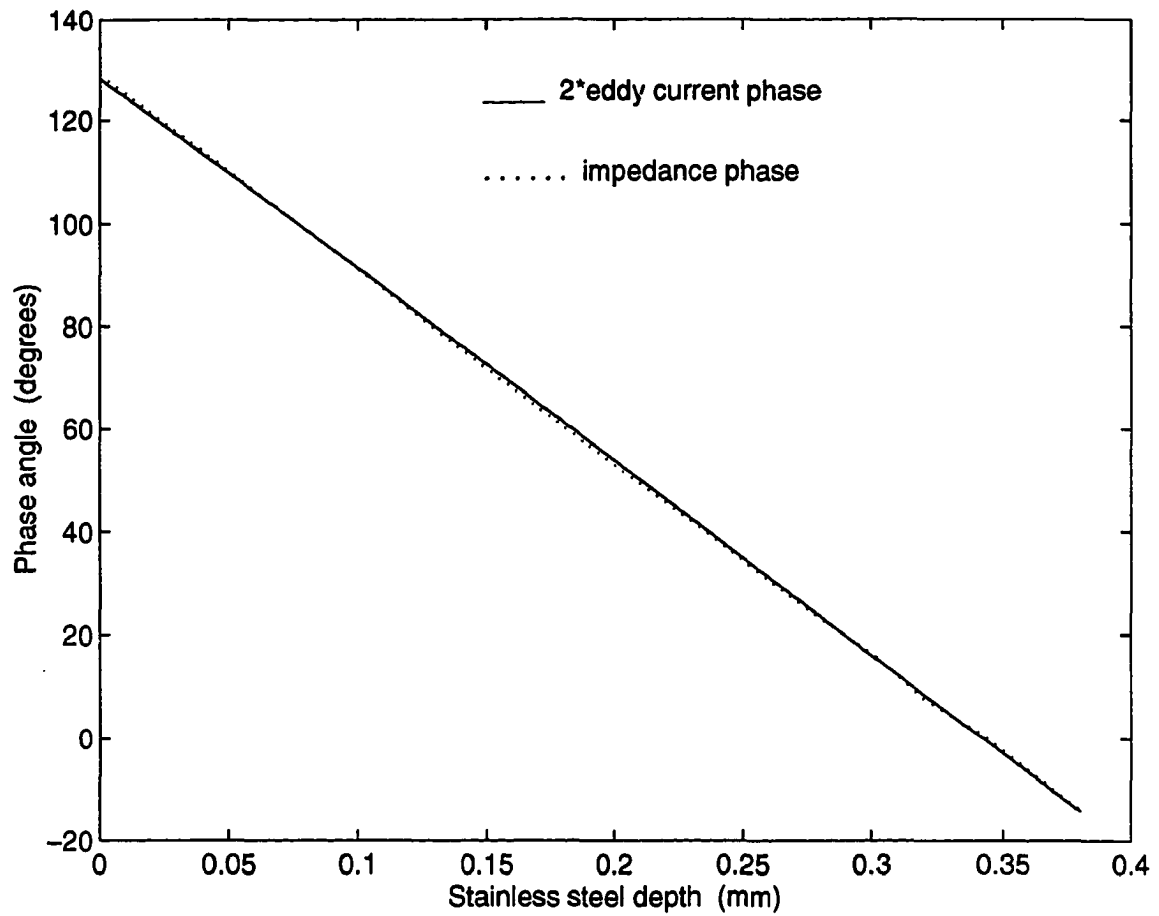


Figure 5.14. Phase shift of impedance vs. defect depth and eddy current phase vs. defect depth.

5.11, the phase shift of ΔZ^s is proportional to the phase of the eddy currents in the unflawed sample for all depths, thus demonstrating that the presence of a void results in a reduced current perturbation to the fields of a larger coil.

This section utilizes a finite element model to extend the 1-D results of Section 5.2 to a 2-D geometry. An inversion algorithm is developed to compensate for the distortion of the induced eddy currents due to the air-metal interface. The algorithm accurately predicts the position of a small void and is robust to reasonable amounts of noise. The resultant images lack adequate resolution to interpret reasonably the position of the flaw. Phase multiplication does increase resolution, however, it is ad hoc in nature and does not appear to be a reasonable solution to this lack of resolution. The next section utilizes experimental results to demonstrate the limitations of this method to practical test situations.

5.4 Experimental implementation

A significant degree of complexity was avoided in Section 5.3 by utilizing a current rail instead of an actual coil. This section attempts to overcome this by implementing this inversion technique on 3-D experimental eddy current data. Since the coil is axisymmetric, the 2-D finite element model can be used to determine the eddy current phase values in the absence of a flaw. These phase values are, of course, the key ingredient necessary for the inversion scheme to be implemented. The experimental study utilizes a series of flat bottom holes 1.60 mm in diameter which are drilled into a 6.35 mm thick aluminum sample ($\sigma = 3 \times 10^7$ S/m). The holes are drilled from the bottom of the sample to various depths d from the inspection surface. The goal is to utilize the inversion algorithm developed in this chapter to determine the depth of the flat bottom holes. A Zetec ferrite core eddy current probe with a diameter of 3.175 mm and an operating frequency of 5 KHz is used for the inspections. The resulting skin depth in the

aluminum is 1.3 mm at 5 KHz. The eddy current coil is scanned over the inspection surface with a resolution of 0.16 mm in the x and y directions with 64 complex impedance values collected in each direction (scan dimension 10.24 mm x 10.24 mm). In conventional eddy current tests, the presence of a flaw can be indicated from plots of the real and imaginary impedance, as well as plots of the magnitude and phase of the impedance. Calibration systems are then used to obtain quantitative information about the flaw (size, shape, depth). The goal of this experimental study is to determine directly the depth of the flaw without utilizing calibration systems.

To implement the inversion algorithm, the eddy current coil must be modeled to predict the eddy current phase values in the unflawed aluminum sample. The resulting electric field equiphase contours calculated with the 2-D axisymmetric finite element model are shown in Figure 5.15. Since the axisymmetric phase data is actually 3-D in nature, a modification to the 2-D inversion of Section 5.3 is necessary in order to implement the algorithm for 3-D imaging. To determine the depth of the holes, a 3-D image array is produced over the test geometry. An image is reconstructed at different depths with intervals of 0.08 mm in the z direction. At each depth the contribution of each x and y pixel is summed and the depth which results in the maximum intensity (indication of an anomaly) is considered the depth of the flaw.

Eddy current impedance data are collected for four different holes. To indicate the presence of a flaw, the magnitude of the coil impedance is displayed prior to implementing the imaging algorithm. Figure 5.16a shows the magnitude of the coil impedance over the scan region for a hole 0.32 mm beneath the inspection surface. From the figure, the presence of a defect is clearly visible at approximately ($x = 5.2$ mm, $y = 4.0$ mm), however, no information about the depth is readily available. To attempt to determine the depth of the defect, the inversion algorithm is implemented with no phase multiplication ($p=1$). The resulting imaging is shown in Figure 5.16b, and as expected, the resolution of the image is quite poor. There is a slight maximum at the position of the flaw, however, the depth is inaccurately predicted to be

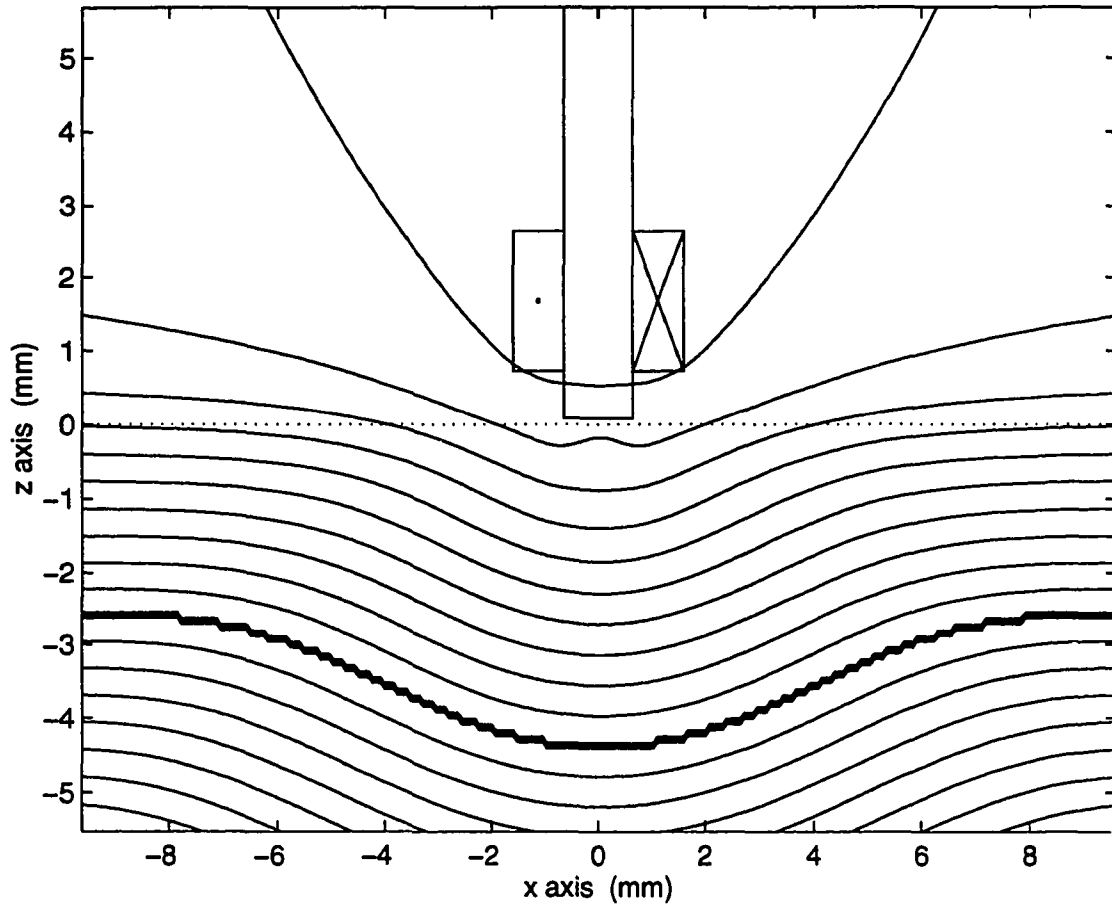
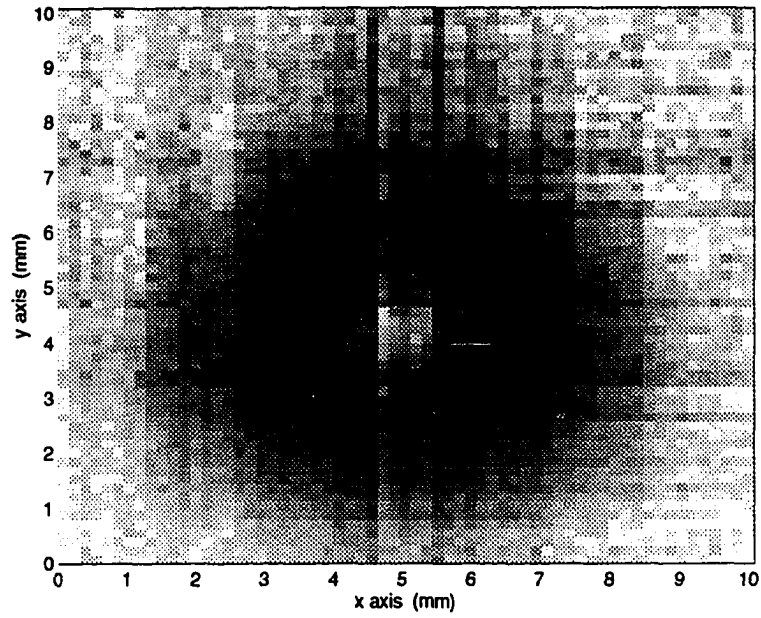


Figure 5.15 Equiphase contours of experimental coil.

(a)



(b)

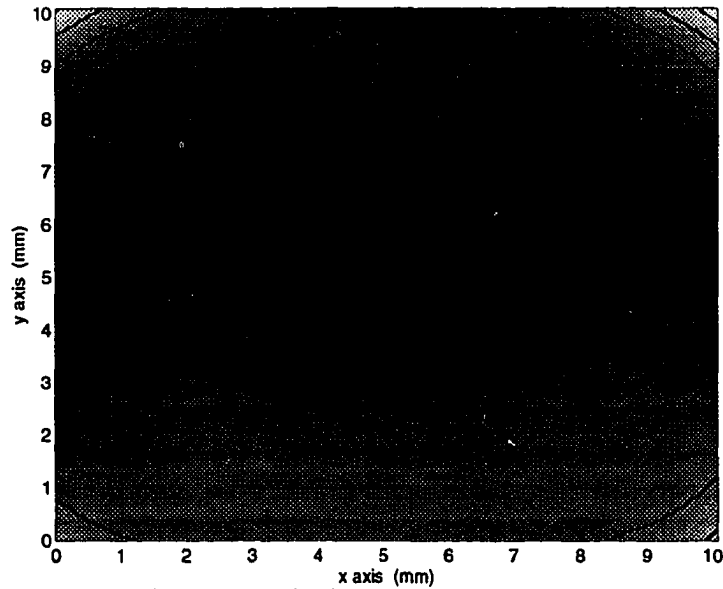
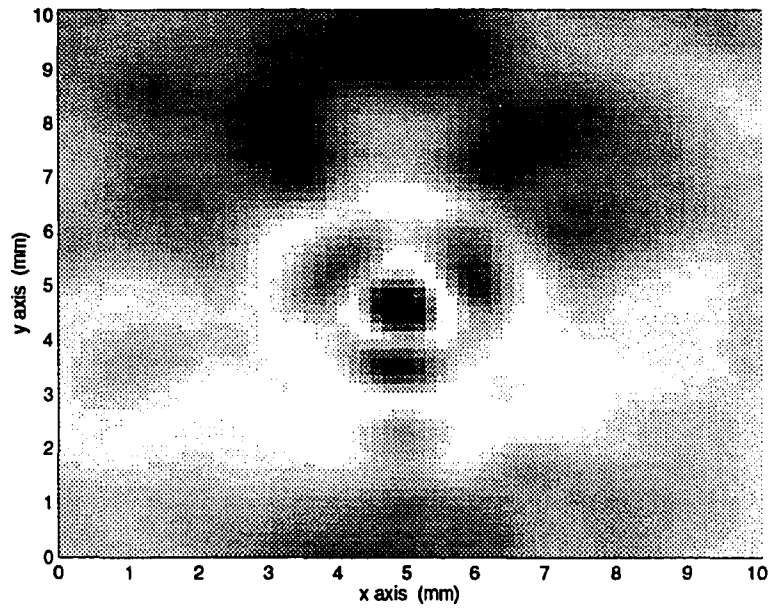


Figure 5.16 Images of hole #2. (a) Magnitude of coil impedance (raster scan) (b) Image with $p = 1$

(c)



(d)

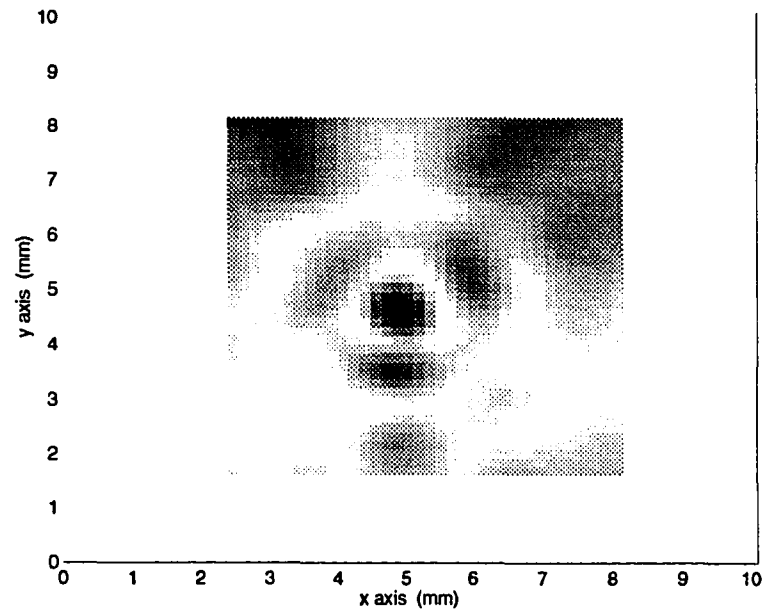


Figure 5.16. cont. (c) Image with $p = 12$ (d) Image with $p = 12$ and windowed impedance data.

at 0.08 mm. Figure 5.16c shows a result with phase multiplication $p = 12$. Here the defect position is much clearer in the x-y plane, however, the predicted defect depth is 0.92 mm. This error in depth prediction appears to be caused in part by artifacts which can be reduced by windowing the original impedance data. To do this, the original impedance magnitude of Figure 5.16a is used to determine the window area. The experimental impedance values inside a window indicating the presence of the defect are utilized while the impedance values outside window are set equal to zero. Thus, only data which indicates the presence of a flaw is utilized in the imaging algorithm. This could also be accomplished through a threshold of the measured impedance data. The result of the inversion algorithm utilizing this windowed data is shown in Figure 5.16d. The image is quite similar to that of Figure 5.16c, however, the depth is now predicted at 0.40 mm, much closer to the actual value. The results of the inversion algorithm for all four holes are presented in Table 5.1. The results indicate that without phase multiplication the inversion algorithm is basically useless at predicting the depth of the holes. With phase multiplication of $p = 12$, the algorithm is extremely inaccurate at determining the depth. When the original data is windowed the results improve substantially. Although the depth of the hole is not predicted exactly, there is a trend in which the calculated depth is correlated to the depth of the hole. The errors in depth can be contributed to many factors including the averaging which takes place in the impedance of the coil due to the extra dimension. Also, there are potential errors in the modeling of the equiphase contours due to potential inaccuracies in the estimated material properties, coil parameters, and coil lift off. There are also errors due to the lack of resolution which can be attributed to the large phase repetition period.

Table 5.1 Predicted depth from inspection surface to top of flat bottom hole.

	Predicted depth		
Depth	m = 1	m = 12	m = 12 (windowing)
0.08 mm	0.08 mm	0.08 mm	0.08 mm
0.32 mm	0.08 mm	0.80 mm	0.40 mm
0.48 mm	0.08 mm	0.96 mm	0.64 mm
0.64 mm	0.08 mm	1.44 mm	0.96 mm

5.5 Conclusions

This chapter develops an eddy current inversion algorithm based on linear phase shifts associated with MQS eddy current impedance measurements. The 1-D analysis demonstrates how linear approximations (weak current perturbations) lead to linear correlations between the phase shift of the impedance and the distance from the source to the perturbing anomaly. An extension to a 2-D geometry demonstrates that this linear impedance phase shift can be used to determine the position of a small subsurface flaw. To overcome the distortion of the coil fields, a technique is introduced to adapt the imaging algorithm to compensate for the distortion in eddy current equiphase contours due to the air-sample interface. The technique is seen to lack adequate resolution to determine the position of subsurface flaws with a high degree of accuracy. Phase multiplication is used to improve the resolution, however, its use significantly reduces the dynamic range of the algorithm and it appears to be an inadequate solution to this problem. The algorithm is implemented on experimental data to attempt to determine the position of subsurface flaws. As expected, without phase multiplication, the technique is

unable to determine the position of the flaws. With phase multiplication ($p=12$) the resolution is improved, however, artifacts are introduced into the image which cause error in the depth predictions. When the impedance data is windowed the robustness of the algorithm improves to the point of having correlations to the actual defect depth, although it does not accurately predict the position of the flaw. Thus, the technique appears to be quite limited for actual inspections. The limitations of this technique can be summarized below:

1. Phase multiplication must be used to improve resolution.
2. Aperture width is limited due to attenuation of fields.
3. Linear approximations must be valid.
4. Coil effects tend to smear the resulting image (modified algorithm reduces this effect).
5. Accuracy of image is dependent on windowing of data.

Although the method espoused does provide a direct quantitative solution to the inverse problem and requires minimal *a priori* knowledge, the above limitations reduce its potential usefulness. The results of the 2-D finite element study indicate that the method is sound in theory and can be applied in idealized situations, however, the experimental results indicate that much future work is necessary if the technique is to provide any useful results. Due to the limitations of resolution, it appears that the best potential for the inversion method introduced in this chapter is, currently, to be used as a counterpart to an existing calibration scheme.

CHAPTER 6. CONCLUSIONS AND FUTURE WORK

The primary goal of this research has been to investigate direct inversion/imaging methods normally associated with fully dynamic electromagnetic wave phenomena to determine under what conditions they can be applied to MQS diffusion phenomena. The secondary goal was to develop techniques which could be used for the direct inversion of MQS data. This chapter summarizes the contributions of this research and indicates avenues for future research.

6.1 Summary of contributions

Chapter 2 develops the governing equations of fully dynamic electromagnetic and MQS NDE. The underlying mathematics and physics of the two systems are shown to have significant differences which affect their associated inverse problem. Fully dynamic electromagnetic fields are governed by hyperbolic partial differential equations which give rise to wave features such as finite time-of-flight and backpropagation. These features are quite useful in the solution of the inverse problem. On the other hand, MQS fields are governed by parabolic partial differential equations which do not allow time-of-flight and backpropagation. For these reasons, the solution of the inverse problem is much more difficult under the MQS approximation. These differences are quite clear in time-domain tests and there appears to be little confusion on this topic. For time-harmonic tests, however, the governing equations of both fully dynamic fields and MQS fields degenerate to elliptic equations which take on a similar form. This has led to the misconception that MQS diffusion fields are, in fact, fully dynamic electromagnetic wave fields. Because of this misconception, some researchers have incorrectly applied "wave-based" backpropagation imaging algorithms such as holography and

tomography to MQS data. Chapter 2 clearly demonstrates that although the elliptic form of the governing partial differential equations takes on the same form, the two systems are still inherently different and must be treated as such. These differences are demonstrated in Chapter 3 through experiments which utilize millimeter wave NDE and eddy current NDE to compare and contrast fully dynamic and MQS phenomena. A "wave-based" SAR technique is used to image millimeter wave data, while conventional raster scans are used for imaging eddy current data. The wave nature of millimeter wave NDE is utilized by inspecting surface flaws on conducting samples in the stand-off mode, thereby providing a significant advantage over eddy current techniques. The technique was quite effective at inspecting EDM notches through dielectric coverings, but more work is required to inspect actual fatigue cracks.

Chapter 4 discusses a transformation approach to imaging eddy current data. The transformation can be used to convert diffusion fields to pseudo-wave fields. These transformed fields are governed by a hyperbolic partial differential equation and thus utilize features such as finite time-of-flight of disturbances and backpropagation of fields. Thus, conventional "wave-based" inversion algorithms can be utilized on the transformed fields. The transformation, however, has many limitations which severely reduce its usefulness. For instance, it lacks robustness to noise and has a restricted class of allowable diffusion sources that can be transformed to stable pseudo-wave sources.

Chapter 5 introduces a technique which can be used for the direct inversion of MQS eddy current data. It differs from other "wave-based" approaches of inverting eddy current data in that no attempt is made to backpropagate the eddy current data. Instead the technique utilizes linear relationships between the complex impedance of an eddy current coil and the distance from the coil to a subsurface flaw. Its use is therefore based on the underlying physics of eddy current NDE. A 1-D analytic study, 2-D finite element study, and 3-D experimental study are utilized to demonstrate the technique. The technique is shown to hold some potential for the inversion of eddy current data, however, there are obstacles which presently reduce its

usefulness. It does not appear to be a technique which can be used independently for eddy current imaging, instead, it may hold potential as a counterpart to existing calibration methods.

6.2 Future work

1. The results of Chapter 3 indicate that millimeter wave NDE can be used to detect surface breaking EDM notches in conducting materials. There are many techniques which might be used to improve the imaging capabilities of this modality. Wider beamwidth horns could be used to improve the image resolution. The increased specular reflection due to the wider horns could be reduced through signal processing schemes. Since the returned scattered energy is dependent on polarization of the fields, this orientation dependence could be utilized to determine the orientation of a flaw. For the technique to be effective, it is necessary to develop calibration methods which utilize the original SAR image, the polarization of the horn, and previous reference standards to determine the size of the surface flaws reliably. The most important avenue for future research is in the detection of surface breaking fatigue cracks. The results of Chapter 3 indicate that fatigue cracks are not detectable with the experimental set up used in this study. Clearly, it is essential that real fatigue cracks be detectable, so immediate research is required in this area.

2. Chapter 4 introduces a method for transforming diffusion fields to pseudo-wave fields for subsequent "wave-based" inversion. There are many robustness limitations to the method and it is not applicable to steady state eddy current NDE. Future work in this area should therefore be concentrated on pulsed eddy current NDE. Although the transformation degrades for non-ideal impulsive sources, low pass filtering appears to add some degree of stability to the transformation of non-ideal sources. The method is also very sensitive to noisy data and more work must be done to develop robust regularization schemes. A major drawback to the

technique lies in the fact that even if the diffusion field is transformed to a pseudo-wave field, the generalized 3-D inverse problem for wave propagation is still quite difficult.

3. Chapter 5 develops a direct inversion technique which can be used for eddy current NDE. The technique is shown to be useful for determining the position of subsurface flaws under ideal conditions, however, physical limitations severely restrict the effectiveness of the technique in practical test situations. Future work in this area should be directed toward implementing the method in a realistic 3-D test situation. This could be most thoroughly studied with a 3-D eddy current computer simulation. The model could be used to determine if the technique can be utilized under ideal test conditions. More detailed experimental studies must be performed along with the numerical study to determine the effectiveness of the technique in non-ideal test situations. Due to the inherent limitation in resolution, the technique does not appear to be adequate as an independent imaging modality. Instead, it would most likely be better suited as a counterpart to an existing calibration technique.

6.3 Concluding remarks

This study has clearly demonstrated that direct inversion method which rely on "wave-based" features should not be applied to MQS data without reasonable justification. This justification must reside in some type of mathematical relationship which transforms the MQS diffusion fields to propagating wave fields. To treat the original MQS interactions as though they result from propagating and scattered electromagnetic waves is incorrect. As demonstrated in Chapter 5, direct inversion techniques which are not "wave-based" can be developed from the underlying MQS phenomenon, however, these inversions do not treat the MQS fields as though they are wave fields. Rather, they take advantage of phase information in a way similar to that underlying the "wave-based" inversion schemes. The transformation

technique discussed in Chapter 4 allow "wave-based" inversion schemes to be applied, however, the field must first be transformed to a pseudo-wave field. Only then can direct inversion schemes be employed on the diffusive data. These techniques, however, suffer from a lack of robustness which limits their usefulness in realistic NDE test situations. In summary, the direct inversion of MQS fields is theoretically possible, however, it must be done with justification based on the governing physical and mathematical MQS phenomenon.

REFERENCES

- [1] R.C. McMaster, Nondestructive Testing Handbook, Vol. 1, The American Society For Nondestructive Testing, Columbus, OH, 1959.
- [2] R.C. McMaster, Nondestructive Testing Handbook, Vol. 2, The American Society For Nondestructive Testing, Columbus, OH, 1959.
- [3] A. Vary, Materials Analysis by Ultrasonics, Noyes Data Corporation, Park Ridge, NJ, 1987.
- [4] H. L. Libby, Introduction to Electromagnetic Nondestructive Testing Methods, Wiley Interscience, New York, 1971.
- [5] W. Lord, S. Nath, Y.K. Shin and Z. You, "Electromagnetic Methods of Defect Detection," IEEE Transactions on Magnetics, Vol. 26, No. 5, pp 2070-2075, September, 1990.
- [6] W. D. Lawson and J. H. Sabey, "Infrared Techniques," Research Techniques in Nondestructive Testing, Edited by R. S. Sharpe, Academic Press, New York, 1970, pp. 443-489.
- [7] V. P. Vavilov and R. Taylor, "Theoretical and Practical Aspects of the Thermal Nondestructive Testing of Bonded Structures," Research Techniques in Nondestructive Testing, Vol. V, Edited by R. S. Sharpe, Academic Press, New York, 1982, pp. 239-280.
- [8] S. S. Udpa and W. Lord, "A Fourier Descriptor Classification Scheme for Differential Probe Signals," Materials Evaluation, Vol. 42, No. 9, 1984, pp. 1136-1141.
- [9] L. Udpa and S. S. Udpa, "Neural Networks for the Classification of Nondestructive Evaluation Signals," IEE Proceedings-F, Vol. 138, No. 1, February 1991, pp. 41-45.
- [10] J. M. Mann, L. W. Schmerr, and J. C. Moulder, "Neural Network Inversion of Uniform-Field Eddy Current Data," Materials Evaluation, Vol. 49, No. 1, January 1991, pp. 34-39.
- [11] L. Udpa and S. S. Udpa, "Eddy Current Defect Characterization Using Neural Networks," Materials Evaluation, Vol. 48, No. 3, March 1990, pp. 342-347.
- [12] I. Elshafiey, L. Udpa, and S. S. Udpa, "A Neural Network Approach for Solving Inverse Problems in NDE," Review of Progress in QNDE, Vol 11A., eds. D. O. Thompson and D. E. Chimenti, Plenum Press, New York, 1992, pp. 709-716.
- [13] M. K. Hu, "Visual Pattern Recognition by Moment Invariants," IRE Transactions on Information Theory, Vol. IT-8, 1962, pp. 179-187.

- [14] R. L. McCreanor, Image Interpolation Via Moments, M.S. Thesis, Colorado State University, Summer 1988.
- [15] R. Shankar, R. Williams, and M. Avioli, "An Expert System for Power Plant NDE," Review of Progress in ONDE, Vol. 9A, eds. D. O. Thompson and D. E. Chimenti, Plenum Press, New York, 1990, pp. 665-672.
- [16] W. Lord, "Numerical Modeling of Electromagnetic NDT Phenomena," New Procedures in Nondestructive Testing, Springer-Verlag, Berlin-Heidelberg, 1983, Chapter 6.
- [17] W. Lord, "A Survey of Electromagnetic Methods of Nondestructive Testing," Mechanics of Nondestructive Testing, Edited by W. W. Stinchcomb, Plenum Press, New York and London, 1982, pp. 77-99.
- [18] M. Cheyney, "A Review of Multidimensional Inverse Potential Scattering," Inverse Problems In Partial Differential Equations, Edited by D. Colton, R. Ewing, and W. Rundell, SIAM, Philadelphia, PA, 1990, pp. 35-48.
- [19] A. J. Devaney, "Fundamental Limitations In Inverse Source And Scattering Problems In NDE," Review Of Progress In ONDE, Vol. 5A, eds. D. O. Thompson and D. E. Chimenti, Plenum Press, New York, 1986, pp. 303-316.
- [20] C. A. Balanis, Advanced Engineering Electromagnetics, John Wiley and Sons, New York, 1989.
- [21] J. D. Jackson, Classical Electrodynamics, John Wiley and Sons, New York, 1975.
- [22] F. John, Partial Differential Equations, Springer-Verlag, New York, 1991.
- [23] R. B. Guenther and J. W. Lee, Partial Differential Equations of Mathematical Physics and Integral Equations, Prentice-Hall, Englewood Cliffs, NJ, 1988.
- [24] Mensa, High Resolution Radar Cross Section Imaging, Artech House, Norwood, MA., 1991.
- [25] B. D. Steinberg and H. M. Subbaram, Microwave Imaging Techniques, Wiley Series In Remote Sensing, John Wiley and Sons, New York, 1991.
- [26] G. T. Ruck, D.E. Barrick, W.D. Stuart, and C.K. Krichbaum, Radar Cross Section Handbook, Plenum Press, New York, 1970.
- [27] C. L. Bennett, "Time Domain Inverse Scattering," IEEE Transactions On Antennas and Propagation, Vol. AP-29, No. 2, March 1981, pp. 213-219.
- [28] C. K. Chan and N. H. Farat, "Frequency Swept Tomographic Imaging of Three-Dimensional Perfectly Conducting Object," IEEE Transactions On Antennas and Propagation, Vol. AP-29, No. 2, March 1981, pp. 312-319.

- [29] R.H.Bates and R.P. Millane, "Time Domain Approaches To Inverse Scattering," IEEE Transactions On Antennas and Propagation, Vol. AP-29, No. 2, March 1981, pp. 359-363.
- [30] H. E. Moses, "A Solution of the Time-Dependent Inverse Source Problem for Three-Dimensional Electromagnetic Wave Propagation," Inverse Methods in Electromagnetic Imaging, Part 1, eds., W. M. Boerner, H. Brand, L. A. Cram, D. T. Gjessing, A. K. Jordan, W. Keydel, G. Schwierz, and M. Vogel, D. Reidel Publishing Company, Dordrecht, Holland, 1985, pp. 77-86.
- [31] K. Langenberg, G. Bollig, M. Fischer, and D. Bruck, "Transient Methods in Electromagnetic Imaging," Inverse Methods in Electromagnetic Imaging, Part 1, eds., W. M. Boerner, H. Brand, L. A. Cram, D. T. Gjessing, A. K. Jordan, W. Keydel, G. Schwierz, and M. Vogel, D. Reidel Publishing Company, Dordrecht, Holland, 1985, pp. 87-110.
- [32] H. Blick and A. G. Tjihuis, "One Dimensional Time-Domain Inverse Scattering Applicable to Electromagnetic Imaging," Inverse Methods in Electromagnetic Imaging, Part 1, eds., W. M. Boerner, H. Brand, L. A. Cram, D. T. Gjessing, A. K. Jordan, W. Keydel, G. Schwierz, and M. Vogel, D. Reidel Publishing Company, Dordrecht, Holland, 1985, pp. 141-156.
- [33] W. Tabbara, "Application of Time-Domain Inverse Scattering to Electromagnetic Waves," Inverse Methods in Electromagnetic Imaging, Part 1, eds., W. M. Boerner, H. Brand, L. A. Cram, D. T. Gjessing, A. K. Jordan, W. Keydel, G. Schwierz, and M. Vogel, D. Reidel Publishing Company, Dordrecht, Holland, 1985, pp. 431-440.
- [34] R. Carriere and R. L. Moses, "High Resolution Radar Target Modeling Using a Modified Prony Estimator," IEEE Transactions On Antennas and Propagation, Vol. 40, No. 1, January 1992, pp. 13-18.
- [35] M. Soumekh, Fourier Array Imaging, Prentice Hall, Englewood Cliffs, NJ 1994.
- [36] J.H. Richmond, "Scattering by a Dielectric Cylinder of Arbitrary Cross-Section Shape," IEEE Transactions on Antennas and Propagation, Vol. AP-13, No. 3, pp. 334-341, May 1965.
- [37] D. N. Ghosh Roy, Methods of Inverse Problems in Physics, CRC Press, Boca Raton, Florida, 1991.
- [38] N. Joachimowicz, C. Pichot, and J. P. Hugonin, "Inverse Scattering: An Iterative Numerical Method for Electromagnetic Imaging," IEEE Transactions on Antennas and Propagation, Vol. 39, No. 12, December 1991, pp. 1742-1752.
- [39] Y. M. Wang and W. C. Chew, "An Iterative Solution of Two-Dimensional Electromagnetic Inverse Scattering Problem," International Journal of Imaging Systems and Technology, Vol. 1, pp. 100-108, 1989.
- [40] A. Roger, "Newton-Kantorovich Algorithm Applied To An Electromagnetic Inverse Problem," IEEE Transactions on Antennas and Propagation, Vol. AP-29, No. 2, March 1981, pp. 232-238.

- [41] A. N. Datta and B. Bandyopadhyay, "Nonlinear Extension to a Moment Method Iterative Reconstruction Algorithm for Microwave Tomography," Proceedings of the IEEE, Vol. 74, 1986, pp. 604-606.
- [42] S. Caorsi, G. L. Gragnani, and M. Pastorino, "Two-Dimensional Microwave Imaging by a Numerical Inverse Scattering Solution," IEEE Transactions on Microwave Theory and Techniques, Vol. 38, No. 8, August 1990, pp. 981-989.
- [43] P. C. Sabatier, "Critical Analysis of the Mathematical Methods Used in Electromagnetic Inverse Theories: A Quest for New Routes in the Space of Parameters," Inverse Methods in Electromagnetic Imaging, Part 1, eds., W. M. Boerner, H. Brand, L. A. Cram, D. T. Gjessing, A. K. Jordan, W. Keydel, G. Schwierz, and M. Vogel, D. Reidel Publishing Company, Dordrecht, Holland, 1985, pp. 43-64.
- [44] V. V. Jory, "Approximation Schema for Generalized Inverses: Spectral Results and Regularization of Ill-Posed Problems," Inverse Methods in Electromagnetic Imaging, Part 1, eds., W. M. Boerner, H. Brand, L. A. Cram, D. T. Gjessing, A. K. Jordan, W. Keydel, G. Schwierz, and M. Vogel, D. Reidel Publishing Company, Dordrecht, Holland, 1985, pp. 365-374.
- [45] R. G. Kouyoumijian, "Asymptotic High-Frequency Methods," Proceedings of the IEEE, Vol. 53, August, 1965, pp. 864-876.
- [46] S. D. Rajan and G.V. Frisk, "A Comparison Between the Born and Rytov Approximations for the Inverse Backscattering Problem," Geophysics, Vol. 54, July 1989, pp. 864-871.
- [47] M. Kaveh and M. Soumekh, "Algorithms and Error Analysis for Diffraction Tomography Using the Born and Rytov Approximations," Inverse Methods in Electromagnetic Imaging, Part 2, eds., W. M. Boerner, H. Brand, L. A. Cram, D. T. Gjessing, A. K. Jordan, W. Keydel, G. Schwierz, and M. Vogel, D. Reidel Publishing Company, Dordrecht, Holland, 1985, pp. 1137-1146.
- [48] F. C. Lin and M. A. Fidy, "The Born-Rytov Controversy," Journal Of The Optical Society Of America, Vol. 9, July, 1992, pp. 1102-10.
- [49] J.M. Blackledge, Quantitative Coherent Imaging, Academic Press, London, 19.
- [50] M. Slaney, A. C. Kak, and L. E. Larsen, "Limitations of Imaging With First Order Diffraction Tomography," IEEE Transactions on Microwave Theory and Techniques, Vol. MTT-32, 1984, pp. 860-873.
- [51] A. J. Devaney, "A Filtered Backprojection Algorithm for Diffraction Tomography," Ultrasonic Imaging, Vol. 4, 1982, pp. 336-350.
- [52] C. Pichot, L. Jofre, G. Peronnet, and J. C. Bolomey, "Active Microwave Imaging of Inhomogeneous Bodies," IEEE Transactions on Antennas and Propagation, Vol. 33, 1985, pp. 416-425.

- [53] K. J. Langenberg, "Introduction to the Special Issue on Inverse Problems," Wave Motion, Vol. 11, North-Holland, 1989, pp. 99-112.
- [54] G. T. Herman, Image Reconstructions From Projections, Academic Press, New York, 1980.
- [55] G. T. Herman and H. K. Liu, "Three-Dimensional Display of Human Organs from Computed Tomograms," Computer Graphics and Image Processing, Vol. 9, 1979, pp. 1-21.
- [56] G. Schwierz, "Review of Tomographic Imaging Methods Applied to Medical Imaging," Inverse Methods in Electromagnetic Imaging, Part 2, eds., W. M. Boerner, H. Brand, L. A. Cram, D. T. Gjessing, A. K. Jordan, W. Keydel, G. Schwierz, and M. Vogel, D. Reidel Publishing Company, Dordrecht, Holland, 1985, pp. 1043-1064.
- [57] W. Tabbara, B. Duchene, C. Pichot, D. Lesselier, L. Chommeloux, and N. J. Joachimowicz, "Diffraction Tomography: Contribution to the Analysis of Some Applications in Microwaves and Ultrasonics," Inverse Problems, Vol. 4, 1988, pp. 305-331.
- [58] J. C. Bolomey and C. Pichot, "Microwave Tomography: From Theory to Practical Imaging Systems," International Journal of Imaging Systems and Technology, Vol. 2, 1990, pp. 144-156.
- [59] A. P. Anderson and M. F. Adams, "Holographic and Tomographic Imaging with Microwave and Ultrasound," Inverse Methods in Electromagnetic Imaging, Part 1, eds., W. M. Boerner, H. Brand, L. A. Cram, D. T. Gjessing, A. K. Jordan, W. Keydel, G. Schwierz, and M. Vogel, D. Reidel Publishing Company, Dordrecht, Holland, 1985, pp. 1077-1106.
- [60] Z. Zhang and J. P. Basart, "Microwave Image Reconstruction of Rod Objects," Review of Progress in ONDE, eds, D. O. Thompson and D. E. Chimenti, Plenum Press, New York, 1993, pp. 355-362.
- [61] A. J. Bahr, Microwave Nondestructive Testing Methods, Vol. 1, Gordon and Breach NDT Monographs and Tracts, Gordon and Breach, New York, 1982.
- [62] N. Ida, Microwave NDT, Kluwer Academic Publishers, Dordrecht, The Netherlands, 1992.
- [63] R. K. Erf, Holographic Nondestructive Testing, Academic Press, Orlando, Florida, 1974.
- [64] Y. I. Ostrovsky, V. P. Shchepinov, and V. V. Yakovlev, Holographic Interferometry in Experimental Mechanics, Springer Series in Optical Sciences, Springer-Verlag, Berlin, 1991.
- [65] A. Lohmann, "The Holographic Principle," Inverse Methods in Electromagnetic Imaging, Part 2, eds., W. M. Boerner, H. Brand, L. A. Cram, D. T. Gjessing, A. K. Jordan, W. Keydel, G. Schwierz, and M. Vogel, D. Reidel Publishing Company, Dordrecht, Holland, 1985, pp. 1033-1042.

- [66] A. E. Ennos, "Optical Holography and Coherent Light Techniques," Research Techniques in Nondestructive Testing, Edited by R. S. Sharpe, Academic Press, New York, 1970, pp. 155-181.
- [67] T. C. Chatters and S. Krishnaswamy, "Nondestructive Evaluation Using Shearing Interferometry," Review of Progress in QNDE, Vol. 11A, eds. D. O. Thompson and D. E. Chimenti, Plenum Press, New York, 1992, pp. 479-486.
- [68] J. W. Goodman, Introduction To Fourier Optics, McGraw-Hill Physical And Quantum Electronics Series, McGraw Hill Book Company, New York, 1968.
- [69] R. Halmshaw, Industrial Radiology Techniques, Wykeham Publications, London, 1971.
- [70] C. V. Kropas and M. E. Hughes, "Computed Tomography Imaging For Nondestructive Evaluation," Review of Progress in QNDE, Vol. 11A, eds. D. O. Thompson and D. E. Chimenti, Plenum Press, New York, 1992, pp. 409-415.
- [71] H. Hauss and J. Melcher, Electromagnetic Fields and Energy, Prentice Hall, Englewood Cliffs, New Jersey, 1989.
- [72] D. L. Waidelich, "Pulsed Eddy Currents," Research Techniques in Nondestructive Testing, Edited by R. S. Sharpe, Academic Press, New York, 1970, pp. 383-416.
- [73] J. L. Fisher and R. E. Beissner, "Pulsed Eddy-Current Crack-Characterization Experiments," Review Of Progress In QNDE, Vol. 5A, eds. D. O. Thompson and D. E. Chimenti, Plenum Press, New York, 1986, pp. 199-206.
- [74] D. L. Waidelich, "Pulsed Eddy-Current Testing of Steel Sheets," Eddy-Current Characterization of Materials and Structures, American Society for Testing and Materials, Philadelphia, PA, 1981, pp. 367-373.
- [75] W. Lord, "A Discussion of the Inverse Problem in Electromagnetic NDE," Review of Progress in Quantitative NDE, Vol. 5A, pp 375, 1986.
- [76] M. M. Lavrent'ev, V.G. Romanov, and S.P. Shishatskii, Ill-Posed Problems of Mathematical Physical and Analysis, American Mathematical Society, Providence, Rhode Island, 1980.
- [77] V. G. Romanov, Inverse Problems of Mathematical Physics, VNU Science Press BV, The Netherlands, 1987.
- [78] A. Pierce, "Wave Methods for an Inverse Problem in Diffusion", Inverse Problems, 2, pp. 205-217, 1986.
- [79] K.H. Lee, G. Liu, and H.F. Morrison, "A New Approach to Modeling the Electromagnetic Response of Conductive Media", Geophysics, Vol. 54, No. 9, pp. 1180, Sept. 1989.

- [80] K.H. Lee and G. Xie, "A New Approach to Imaging with Low-Frequency Electromagnetic Fields", Geophysics, Vol. 58, No. 6. pp. 780, June 1993.
- [81] J. Viriex, C. Floresluna and D. Gibert, "Asymptotic Theory for Diffusive Electromagnetic Imaging", Geophysics Journal, July 1993.
- [82] S. Ross, M. Lusk, and W. Lord, "A Transformation Approach to Imaging Eddy Current NDE," accepted for publication in IEEE Transactions On Magnetics, April 1995.
- [83] J.P. Coronas, M.E. Davison, and R.J. Krueger, "Direct and Inverse Scattering in the Time Domain by Invariant Embedding Techniques," The Journal of the Acoustic Society of America, Vol. 74, 1983, pp. 1535-1541.
- [84] M. Cheyney, J. Rose, and B. DeFacio, "Three-Dimensional Inverse Scattering," Inverse Source Problems, 1986, pp. 61-68.
- [85] P. DuChateau, "Inverse Problems for Parabolic Partial Differential Equations," Inverse Problems, Edited by J.R. Cannon and W. Hornung, 1986, pp. 51-60.
- [86] C. D. Pagani, "Determining a Coefficient in a Parabolic Equation," Applied Analysis, Vol. 14, 1982, pp. 99-116.
- [87] R. O. McCary and J. R. Viertl, "Automating An Eddy Current Test System For In-Service Inspection Of Turbine/Generator Rotor Bores," IEEE Transactions On Magnetics, Vol. 24, No. 6, Nov. 1988, pp. 2594-2596.
- [88] T. W. Guettinger, K. Grotz, and H. Wezel, "Eddy Current Imaging," Materials Evaluation, Vol. 51, No. 4, April 1993, pp. 444-451.
- [89] P. Weidelt, "Electromagnetic Induction in Three-Dimensional Structures," Journal of Geophysics, Vol. 41, 1975, pp. 85-109.
- [90] L. D. Sabbagh and H. A. Sabbagh, "Eddy-Current Modeling and Flaw Reconstruction," Journal of Nondestructive Evaluation, Vol. 7, Nos. 1/2, 1988, pp. 95-109.
- [91] S. M. Nair and J. H. Rose, "Reconstruction of Three-Dimensional Conductivity Variations from Eddy Current (Electromagnetic Induction) Data," Inverse Problems, Vol. 6, 1990, pp. 1007-1030.
- [92] B. A. Auld, F. G. Muennemann, and M. Riazat, "Quantitative Modelling of Flaw Responses in Eddy Current Testing," Research Techniques in Nondestructive Testing, Vol. 7, edited by R.S. Sharpe, London, 1984, pp. 37-76.
- [93] B. A. Auld, S. R. Jefferies, and J. C. Moulder, "Eddy-Current Signal Analysis and Inversion for Semielliptical Surface Cracks," Journal of Nondestructive Evaluation, Vol. 7, Nos. 1 and 2, 1988, pp. 79-94.
- [94] J. H. Rose and S. M. Nair, "Exact Recovery of the DC Electrical Conductivity of a Layered Solid," Inverse Problems, Vol. 7, 1991, pp. L31-L36.

- [95] R. G. Olson, "Power-Transmission Electromagnetics," Antennas and Propagation Magazine, Vol. 36, No. 6, December 1994, pp. 7-16.
- [96] M. N. O. Sadiku, Elements of Electromagnetics, Saunders College Publishing, Holt, Rinehart and Winton, Inc., Orlando, FL, 1989.
- [97] B.P. Hildebrand and G.L. Fitzpatrick, "Inversion of Eddy Current Data Using Holographic Principles," Review of Progress in Quantitative NDE, Vol. 4A, pp. 507-515, 1985.
- [98] J. M. Prince, B. P. Hildebrand, and G. L. Hower, "The Eddy Current Probe as a Holographic Transducer," Journal of Nondestructive Evaluation, Vol. 12. No. 4. pp. 209-217, 1993.
- [99] J.H. Hippler, H. Ermert, and L. Von Bernus, "Broadband Holography Applied to Eddy Current Imaging by Using Signals with Multiplied Phases," Journal of Nondestructive Evaluation, Vol. 12. No. 3. pp. 153-162, 1993.
- [100] R. Zorgati, B. Duchene, D. Lesselier and F. Pons, "Eddy Current Testing of Anomalies in Conductive Materials, Part I: Qualitative Imaging via Diffraction Tomography Techniques," IEEE Transactions on Magnetics, Vol. 27, No. 6, pp. 4416, 1991.
- [101] O. Pade and A. Mandelis, "Thermal-Wave Slice Tomography Using Wave-Field Reconstruction," Inverse Problems, Vol. 10, 1994, pp. 185-197.
- [102] A. Mandelis, "Theory of Photothermal Wave Diffraction Tomography Via Spatial Laplace Spectral Decomposition," J. Phys. A: Math. Gen. Vol. 24, 1991, pp. 2485-2505.
- [103] L. Udpa, Imaging of Electromagnetic NDT Phenomena, Ph.D. Dissertation, Colorado State University, Fort Collins Colorado, 1985.
- [104] L. Udpa and W. Lord, "Diffusion, Waves, Phase and Eddy Current Imaging," Review of Progress In Quantitative Nondestructive Evaluation", Vol. 4A, pp. 499, 1985.
- [105] R. H. Bates, G. C. McKinnon, And A. D. Seagar, "A Limitation on Systems for Imaging Electrical Conductivity Distributions," IEEE Transactions on Biomedical Engineering, Vol. BME-27, No. 7, July 1980, pp. 418-420.
- [106] L. Udpa and W. Lord, "A Search-Based Imaging System for Electromagnetic Nondestructive Testing," IEEE Expert, 1989, pp. 18-26.
- [107] W. Lord and L. Srinivasan, "Deconvolution of Defect Leakage Field Profiles Obtained by Using Hall Element Probes," Vol. 3B, Review of Progress in ONDE, eds, D. O. Thompson and D. E. Chimenti, Plenum Press, New York, 1982, pp. 855-862.
- [108] D. J. Hagamaier, "Application of Eddy Current Impedance Plane Testing," Materials Evaluation, Vol. 42, July, 1984, pp. 1035-1040.

- [109] A. J. Bahr, "Microwave Eddy-Current Techniques for Quantitative Nondestructive Evaluation," Eddy Current Characterization of Materials, pp. 311-331, American Society for Testing and Materials, Philadelphia, PA 1979.
- [110] C. Y. Yeh, E. Ranu, and R. Zoughi, "A Novel Microwave Method for Surface Crack Detection Using Higher Order Waveguide Modes," Materials Evaluation, Vol. 52, No. 6, June 1994, pp. 676-681.
- [111] R. J. Hruby and L. Feinstein, "A Novel Nondestructive, Noncontacting Method of Measuring the Depth of Thin Slits and Cracks in Metals," The Review of Scientific Instruments, Vol. 41, No. 5, May 1979, pp. 679-683.
- [112] M. T. Lusk and H. C. Han, "Nondestructive Evaluation Using Swept-Frequency Synthetic Aperture Radar," Review of Progress In Quantitative Nondestructive Evaluation, edited by D. O. Thompson and D. E. Chimenti, Plenum Press, New York, Vol. 13A, 1994, pp. 607-614.
- [113] Technical Manual, M/M Wave Devices 18.0 To 325.0 GHz, Aerowave Inc, Medford, MA. 02155, 1995.
- [114] A. N. Tikhonov and V. Y. Arsenin, Solutions of Ill-Posed Problems, John Wiley and Sons, Washington, D.C. 1977.
- [115] J. Hadamard, Lectures on the Cauchy Problem in Linear Partial Differential Equations, Yale University Press, New Haven, 1923.
- [116] A.S. Leonov, "On the Choice of Regularization Parameter by Means of the Quasi-Optimality and the Ratio Criteria," Soviet Math. Dokl., 19, pp. 537, 1978.
- [117] L. Dou and R. J. W. Hodgson, "Application of the Regularization Method to the Inverse Black Body Radiation Problem," IEEE Transactions on Antennas and Propagation, Vol. 40, No. 10, pp. 1249-1253, 1992.
- [118] M. Hegland, "An Optimal Order Regularization Method Which Does Not Use Additional Smoothness Assumptions," SIAM Journal on Numerical Analysis, Vol. 29, No. 5, pp. 1446-1461.
- [119] M. M. Radulescu, J. C. Sabonnadiere, G. Meunier, and D. Micu, "A New Procedure for Choosing the Regularization Parameter in Electromagnetic Field Synthesis Discrete Problems," Compumag 9th Conference on the Computation of Electromagnetic Fields, 1993, pp. 546-548.
- [120] W. Chen, "A New Extrapolation Algorithm for Band-Limited Signals Using the Regularization Method," IEEE Transactions on Signal Processing, Vol. 41, No. 3, pp. 1048-1060, March, 1993, pp. 1048-1060.
- [121] K. Radhakrishnan and M. Lusk, "Thin Film Measurements with Millimeter Wave NDE," submitted to IEEE Transactions on Microwave Theory and Techniques, February, 1995.

- [122] S. Palinasimy, Finite Element Modeling of Electromagnetic NDE, Ph.D. dissertation, Colorado State University, 1980.